A STUDY OF PUMP CAVITATION DAMAGE

CONTRACT NO. NAS8-34535

GEORGE C. MARSHALL SPACE FLIGHT CENTER
MARSHALL SPACE FLIGHT CENTER, AL 35812

BY

MICHAEL C. BROPHY
DAVID R. STINEBRING
MICHAEL L. BILLET

APPLIED RESEARCH LABORATORY
THE PENNSYLVANIA STATE UNIVERSITY
POST OFFICE BOX 30
STATE COLLEGE, PA 16801

30 NOVEMBER 1983

A Study of Pump Cavitation Damage

Contract No. NAS8-34535

George C. Marshall Space Flight Center
Marshall Space Flight Center, AL 35812

by

Michael C. Brophy
David R. Stinebring
Michael L. Billet

Applied Research Laboratory
The Pennsylvania State University
Post Office Box 30
State College, PA 16801

30 November 1983

Abstract

This report documents the cavitation assessment for the Space Shuttle Main Engine (SSME) high pressure oxidizer turbopump (HPOTP). In order to do this, a model of the flow through the pump had to be developed. Initially, a computational procedure was developed to analyze the flow through the inlet casing including the prediction of wakes downstream of the casing vanes. From these flow calculations, cavitation patterns on the inducer blades were approximated and hence the damage rate estimated. The model correlates the heavy damage on the housing and over the inducer with unsteady blade surface cavitation. The unsteady blade surface cavitation is due to the large incidence changes caused by the wakes of the upstream vanes. Very high cavitation damage rates are associated with this type of cavitation. As a result of the computational procedure, a set of design recommendations for reducing the unsteady cavitation are given. These include removing the set of vanes closest to the inducer and modifying the remaining vanes.

Table of Contents

Table of Contents

List of Tables

List of Figures

List of Figures (Cont'd)

List of Figures (Cont'd)

1. Introduction

The destructive action caused by cavitation has long been a problem of practical importance with fluid machinery. At the turn of the century, severe erosion of the propellers on the ships Lusitania and Mauretania [1] prompted the creation of a special commission by the British Admiralty to investigate the problem. It was determined that the damage was the result of repeated "hydraulic blows" accompanying the collapse of cavities.

After nearly 100 years of research in this area, the problem of predicting damage on a prototype is still unsolved. This is not due to a lack of work in this area but rather due to the fact that cavitation damage involves both solid mechanics and the fluid mechanics of two-phase flows, and thus is inherently difficult. As noted in a recent article by Hutton [2] there has been some success in empirically predicting when and where cavitation may begin, but there are difficulties in predicting how serious its damage effects might be. The literature on cavitation damage is very extensive and as noted by Hutton [2] "provides absorbing reading for those with a morbid interest in engineering failures".

The problems associated with the occurrence of severe cavitation damage in fluid handling machinery are primarily dependent on the degree and type of cavitation. The majority of all fluid machinery can operate with some limited degree of cavitation and still provide satsifactory performance although damage can still occur if operated over longer periods of time. However, large amounts of cavitation not only causes severe cavitation damage, but the accompanying rapid formation and collapse of cavities alters the local pressure field acting on each blade segment. As a result, net axial and radial thrusts become random, reaching high magnitudes at unpredictable

frequencies. The unsteady forces generated in this manner cause severe wear and damage to bearings and seals.

The practical problem addressed in this report is the reduction of cavitation damage in the Space Shuttle Main Engine (SSME) high pressure oxidizer turbopump (HPOTP) and the improvement of its life expectancy. Experience with cavitation damage suggests that this is a difficult problem because it involves (1) a prediction of the pressure field in the turbopump, (2) a prediction of the cavitation type and extent, (3) the determination of cavitation impact pressures, and (4) an analysis of the interaction between cavitation impact pressure and the material response. All four of these issues must be addressed in order to predict a cavitation damage rate and hence the turbopump life expectancy. This problem is further complicated when one realizes that the turbopump will operate off-design for extended periods of time. Thus, before developing a damage model, some assumptions must be made from a detail assessment of the existing turbopump data. This assessment includes hardware geometry, hardware evidence of cavitation damage, operating conditions and life requirements.

The characteristics of the SSME are given in Table 1 and the SSME powerhead component arrangement showing the HPOTP is illustrated in Figure 1. The HPOTP is shown in Figure 2 and its operating conditions are listed in Table 2.

Examination of the turbopump hardware shows that cavitation damage occurred at the following locations:

1. Housing (casing) upstream and alongside the inducer,
2. Inducer blades near the tip,

3. Impeller near the partial blades, and

4. Impeller blades at the exit diameter.

Damage on the impeller is relatively light; however, the damage associated with the inducer is very severe.

Figure 3 shows schematically that the damage on the inducer occurs in an area located at the blade tip. The most severe damage, however, occurs on the housing, downstream of the stator vanes and near the leading edge of the inducer. This damage appears at discrete spots as can be noted in Figure 4 for the left-hand pump housing and in Figure 5 for the right-hand pump housing. In addition, a band of cavitation damage occurs on the housing near the trailing edge of the inducer as can be noted in Figure 6.

The deep-pitting cavitation damage occurring on the housing significantly reduces the life expectancy of the turbopump. A depth of cavitation damage of 0.05 inches in only 30 minutes of operation has been documented by Rocketdyne and Figure 7 shows the characteristics of a typical pit. This time is significantly less than the goal of 7.5 hours for the life expectancy of the turbopump (see Table 1).

High damage rates can be expected in this area of the turbopump because of high inducer tip speed which is in excess of 600 ft/sec. Many investigators such as Knapp [3] and Stinebring [4] have shown that the damage rate is proportional to the sixth power of the relative velocity.

The existence of deep pitting suggests that bubble collapse is occurring predominantly at these locations. This is possible if the amount of cavitation occurring on the inducer varies circumferentially, and could result from a changing flow incidence angle.

In this report, a model is developed which correlates the heavy damage on the housing and over the inducer blades with unsteady blade surface

cavitation. Initially, a flow calculation procedure was developed that gives the inlet flow distribution at the inducer including the wakes from the upstream vanes. The cavitation type and extent were predicted using the inlet data, flow conditions and blade geometry. The cavity volume shed was then used to predict the cavitation damage rate. Finally, recommendations for a redesign are given that should significantly reduce the cavitation damage rate.

2. Analysis of Existing Design

2.1 Inviscid Flow Calculations

The flow through the High Pressure Oxidizer Turbopump (HPOTP) is very complicated and the design of its components is critical. It consists of five blade rows, three of which are stationary, and the flow is turned four times in a very short distance. This compact geometry is illustrated in Figure 2. The blade rows are identified as (1) the inlet casing vanes, (2) the stator vanes, (3) the inducer, (4) the centrifugal impeller, and (5) the exit diffuser vanes. The flow analysis begins with an examination of the first two blade rows.

The inlet casing is a very difficult component to analyze. Flow enters through a pipe and is split in half to form a double-suction entrance. The flow is then divided again in each side inlet (left and right), and is thus symmetric about a vertical axis, but each side inlet is asymmetric about the axis of rotation. Only a three-dimensional (3-D) code would be able to give a true prediction of the flow in this element. While there may exist 3-D codes to solve for the inlet casing alone, it is doubtful that a code exists at this time that would be able to include the stationary vane rows as well.

Since flow through the inlet casing is predominantly radial for the stationary vane rows, a two-dimensional (2-D) approximation for the inlet

casing was chosen. A side view of this geometry is illustrated in Figure 8 and allows computation of the flow components in the radial (R) and circumferential (θ) directions only. The flow will be considered to be uniform in the axial (Z) direction.

Based on the design drawings of the HPOTP, a 2-D configuration can be constructed for the inlet casing boundary, the inlet casing vanes, and the stator vanes which is illustrated in Figure 9. The fifth stator vane at the bottom of the inlet has been blended into the casing boundary and provides for vertical symmetry of the flow in the inlet. It is still impractical, however, to solve for the flow in this configuration. A transformation must be performed to convert this radial flow geometry into a linear cascade geometry.

It is possible to solve for the flow in this geometry if all the stationary vanes are removed. The resulting singly-connected domain can be solved by using a finite element method. A grid-work of triangular elements is illustrated in Figure 10. A total of 647 nodes and 1180 elements were used in this configuration.

If the flow is assumed to be incompressible (Mach number below 0.3), the continuity equation in cylindrical or polar coordinates can be written as follows:

$$\frac{\partial V_r}{\partial r} + \frac{1}{r}\frac{\partial V_\theta}{\partial \theta} + \frac{V_r}{r} = 0 \quad . \tag{1}$$

This equation can be made an identify by defining a streamfunction:

$$V_r = \frac{1}{r}\frac{\partial \psi}{\partial \theta} \quad , \quad V_\theta = -\frac{\partial \psi}{\partial r} \quad . \tag{2}$$

Thus, one has

$$\frac{1}{r}\frac{\partial^2 \psi}{\partial r \partial \theta} - \frac{}{r^2}\frac{\partial \psi}{\partial \theta} - \frac{1}{r}\frac{\partial^2 \psi}{\partial \theta \partial r} + \frac{1}{r^2}\frac{\partial \psi}{\partial \theta} = 0 \quad . \tag{3}$$

For irrotational flow (ω=0), the Laplace equation results from the definition of angular momentum and can be written as

$$-\omega r = \frac{\partial V_r}{\partial \theta} - \frac{\partial V_\theta}{\partial r} - V_\theta = \frac{\partial^2 \psi}{\partial r^2} + \frac{\partial \psi}{\partial r} + \frac{1}{r}\frac{\partial^2 \psi}{\partial \theta^2} = \nabla^2 \psi = 0 \quad . \qquad (4)$$

This equation can be readily solved by even the most basic of finite element methods.

The boundary conditions for the streamfunction are a value of 0.0 on the right vertical boundary and a value of 1.0 on the outer casing boundary. The value of ψ increases linearly from right to left for the top boundary and from top to bottom counterclockwise for the inner boundary. This results in a uniform normal velocity at the top inlet and at the inner circular exit. This does not mean that the tangential velocity at these locations will necessarily be equal to zero. Because of the geometry of the top inlet, the flow is everywhere parallel to the side boundaries and there is nothing capable of sustaining a pressure gradient across the channel which would allow a tangential component of the flow to exist. As the radius of the inner circular boundary is reduced to zero the flow here must also be uniform, and thus no tangential flow component will exist at this boundary. There will however exist a substantial V_θ component at the radii of interest, that is the exit of the inlet casing vanes and the exit of the stator vanes.

The finite element solution is illustrated in Figure 11. The streamlines that are plotted (constant values of ψ) represent equal increments of flow. Lines that are close together indicate high velocities and lines that are further apart indicate lower velocities. It can be seen that the flow is indeed uniform at the inlet and the exit. At the indicated radii a substantial V_θ component of the flow is shown to exist. It will be the task of the stationary vanes to remove this tangential velocity.

The solution technique employed to solve for the 2-D configuration with vanes is the Modified Douglas Neumann Cascade Program [6]. In this approach each body or vane is divided into many small segments and at each is located a source/sink of unknown strength. The Neumann boundary condition is used by this method and requires that there be no flow normal to any boundary. For lifting bodies (those that are not symmetric normal to the flow direction), the Kutta condition is also employed to insure that the flows from both surfaces exit the body in parallel at the trailing edge. For a specified flow angle (for example the inlet flow angle) a solution is obtained for all of the source/sink strengths, the accuracy of which reaches one hundred percent as the number of points or segments on the bodies becomes infinite. With these values known the velocity can be calculated anywhere in the field. At locations far upstream and downstream the calculated velocity will necessarily be parallel and uniform.

The original Douglas Neumann Cascade Program was developed by the Douglas Aircraft Corporation [5] and extended the existing solution technique being employed for isolated airfoils to cascades of lifting or non-lifting bodies. The program has been modified to include cascades with radial flow, either inward or outward, and cascades with bodies of varying geometry. Radial flow cascades are solved by transforming them into linear cascades using a conformal transformation:

$$x = \ell n\ r$$
$$y = \theta \quad . \tag{5}$$

Velocities calculated for the linear cascade are converted to the radial-flow plane by simply dividing by the radius as follows:

$$V_r = \frac{1}{r} V_x \quad , \quad V_\theta = \frac{1}{r} V_y \quad . \tag{6}$$

Special considerations must be taken to account for the inlet casing boundary since one would not normally consider this element to be a body in a cascade.

If the inlet casing boundary shown in Figure 9 were transformed using Equation (5) the large body with the dotted lines shown in Figure 12 would be produced. With the flow proceeding from left to right it can be seen that a large portion of the flow (aproximately eleven-twelths) would be blocked by the inlet casing, body number 1. This is due to the flow entering the casing through the vertical inlet which only accounts for about 30 degrees of the circumference at a radius of 12 inches. It is therefore logical and accurate to represent the inlet casing boundary as the streamlined body shown in Figure 12 to facilitate the flow calculation procedure.

It is important to model the flow in the vertical inlet correctly. In Figure 2 the flow is uniform and directed downward toward the axis of rotation. At large radii this flow can be approximated as radial. This will result in a horizontal portion of the boundary in the transformed plane, Figure 12. Uniform linear flow in this portion of the transformed geometry most accurately models the vertical section of the inlet casing. This does result in boundaries in the 2-D geometry of Figure 9 which are radial at large radii. This type of adjustment is necessary for closure of body number 1 in the transformed cascade of Figure 12.

The Modified Douglas Neumann Cascade Program was first run for only one body, that of the inlet casing boundary. For the transformed geometry, 159 points were used to describe this body. The resulting flow solution is illustrated in Figure 13. If this figure is overlayed with the finite element solution shown in Figure 11, the two can be seen to correlate exactly. Thus one method validates the other.

The thirteen inlet casing vanes and four stator vanes were then added to solve for the flow in the 2-D configuration of Figure 9. Although the vanes are symmetric about a vertical axis they are each unique when plotted in the transformed plane. The inlet flow angle was set equal to zero to reflect this symmetry. The number of points used to describe these vanes ranged from 31 for the stators to over 50 for the largest inlet casing vane. In all, 780 points were used to describe this cascade consisting of 18 bodies. The spacing used for each body is 2π such that the entire geometry illustrated in Figure 12 is repeated at the top and bottom to form an infinite cascade. It took over an hour of CPU time to solve this problem on the VAX 11/782 computer.

The flow solution is first illustrated in the transformed plane in Figure 14. The velocity vectors are plotted based on information at over 300 off-body points. In Figure 15 the flow solution has been transformed back to the radial 2-D configuration. When compared with the solution for the inlet casing boundary alone in Figure 13 it can be seen that the vanes have indeed taken out a large portion of the turning. However, a substantial amount of tangential velocity still exists and this will have a marked effect on the inlet flow at the inducer.

The flow through the entire cross-section of the HPOTP can be analyzed using a streamline curvature method (SCM) [7]. In the SCM program used at ARL/PSU the effect of each blade row is accounted for by specifying the blade advance ratio (flow coefficient) and the particular distribution of V_θ at the trailing edge station. The V_θ profile determines the change in angular momentum effected by the blade row and the advance ratio computes the change in energy if the blade row is rotating. The SCM program can only solve for axisymmetric flow, which is essentially 2-D in that no derivatives are allowed

in the circumferential (θ) direction. It solves the continuity, momentum and energy equations for the real variables: velocities and pressure. In the process, the streamline locations are found as well.

The streamline curvature solution is illustrated in Figure 16. The location of the blade rows are highlighted, including the split impeller blades in the rotor. The exit diffuser vanes were omitted for this analysis, but could have easily been included. The inlet portion, although represented correctly, is not axisymmetric and merely serves to feed the flow into the axisymmetric stator, inducer and impeller portion of the flow channel. A significant circumferential variation in the flow field was previously found, since the channel geometry is not axisymmetric until just prior to entering the stator, station 14. It can be seen however that a plane passed normal to Figure 16 would closely correspond to the two-dimensional configuration used in Figure 8.

The flow solution illustrated in Figure 16 is for the case of no turning added by the blade rows, which for the HPOTP means that the stationary vanes have taken out the turning imparted by the asymmetric inlet. There is no appreciable difference between the location of the streamlines when a uniform (2-D) tangential velocity is added across the span of the inlet casing vanes and/or the stator. Essentially the SCM solves for the through-flow and this must be combined with the Douglas Neumann circumferential solution to obtain the 3-D picture of what is happening at the inducer inlet.

It now becomes necessary to describe the flow along the various streamlines in Figure 16 as the flow turns the corner. Five streamlines from the SCM solution were selected which divide the flow into four equal portions. There are three locations of primary importance in this part of the analysis: (1) downstream of the exit of the inlet casing vanes (R = 3.5 in), (2) the

exit of the stator vanes (2.13 in $\leq$ R $\leq$ 2.46 in), and (3) the inducer measuring station (1.325 in $\leq$ R $\leq$ 2.37 in). The corresonding stations for the SCM solution are shown in Figure 16 as numbers 13, 18 and 22. The flow will be computed at these locations as it turnes the corner.

The first location at a radius of 3.5 inches will illustrate the flow as it exits the inlet casing vane row and enters the stator vane row. Here the flow is assumed radial and is calculated from the Douglas Neumann solution of the vane geometry in Figure 9. Data points are distributed about the circumference at every ten degrees. These are spline fit and plotted in Figure 17. The velocities are dimensionalized for the design condition at 100% power level, but could easily be changed to another condition by multiplying the ratio of the volume flow rates at these two conditions. The zero degree location corresponds to the top of the circle at this radius, just downstream of inlet casing vane number 2. Although this is a potential flow solution the obvious location of the stator vanes illustrates the blockage that results with these two vanes in the flow on this side of the pump. It is at this radius that the wakes produced by the inlet casing vanes will be added to the potential or inviscid flow (see Section 2.2).

In a similar manner the second location illustrates the flow exiting the stator vane row. Again the flow is assumed radial and is calculated from the Douglas Neumann solution. Although the stator was calculated as a 2-D blade shape the actual length of the vane decreases from hub-to-tip. Five radii are therefore employed at station 18 to account for this variation. Since the stator vane exit radius was fixed in Figure 9, the blockage effect at the tip will be more pronounced than that at the hub. This is illustrated in Figures 18 through 22 for each of the five selected streamlines.

For both of these locations the radial velocity is integrated to check on the massflow and dimensionalize the velocity components. The average or normalized velocity is indicated for each of the radial positions plotted. When the integration is performed the stream function is calculated as a function of circumferential location. From Equation (2) with r constant the streamfunction becomes

$$\Delta\psi = r \sum_{o}^{\pi} V_r \, \Delta\theta \quad . \tag{7}$$

These values are normalized by the design massflow to produce values of the streamfunction from zero to one as theta increases from 0 to π radians.

Since constant values of ψ represent streamlines, the location of a selected fluid particle can be calculated at each of the two radii. This links up the locations of importance as the flow turns the corner.

The third location at the inducer station where experimental data are available is analyzed in a similar fashion with two major exceptions. First, the streamline changes from the radial direction to the axial direction which results in a different average through-flow velocity with which to normalize the flow due to area changes. Second, the law of constant angular momentum which is employed in the SCM cannot be used for this portion of the analysis. Recall that the SCM solution is valid for axisymmetric flow only. As the fluid particle changes radius from that at the stator vane exit to that of the inducer inlet, the casing will continue to act on it and produce a variation in the angular momentum of the fluid around the circumference. Thus the tangential velocity will not always increase as the radius decreases.

The potential flow field at the inducer station is depicted in Figure 23. There is a noticeable indication of blockage at the two stator locations at

radii towards the tip streamline. This results from the close proximity of the stator vanes and the inducer leading edge at the outer tip boundary. It is important to note that the massflow falls off towards the bottom of the inlet. This would be expected for an inlet with flow entering at the top.

2.2 Addition of the Viscous Effects to the Inviscid Flow Analysis

The viscous boundary layer growth on the stationary blade rows will lead to flow deviation and wake velocity deficits downstream of the vanes. These effects can readily be included in the flow analysis. In the real fluid flow case turning vanes will always achieve less turning than that indicated by their camber lines. The fluid will not exit at the blade angle, but at a lesser angle. In the inviscid analysis the flow is constrained by the Kutta condition to exit at the specific trailing edge angle. In order to achieve the proper flow condition downstream of the vane rows, the fluid deviation must be added to the inviscid calculation. This was accomplished by fixing the vane shapes at the leading edge and increasing the stagger angle so as to force the flow to exit at the deviated flow angle. This is illustrated in Figure 24. Thus the flow downstream of the vanes will be at the corrected angle.

The deviation angle was estimated from the blade geometry and the blade incidence angle obtained from the inviscid flow analysis. The deviation can be expressed as

$$\delta = \delta_o + \Delta\delta^* - \Delta\delta' \qquad (7)$$

where δ_o is the deviation angle due to camber, $\Delta\delta^*$ is the deviation angle due to vane thickness and $\Delta\delta'$ is the deviation angle due to flow acceleration.

The deviations due to thickness and camber were obtained by utilizing empirical data which have been collected by Lieblein [8]. The work by Lakshminarayana [9] was used to estimate the deviation due to flow acceleration.

It is important to note that cascade relationships were used to estimate the deviation angles for the vanes inside the casing. However since all of the vanes in the HPOTP are of different geometry, the calculated deviation angles are only approximate.

The resulting Douglas Neumann solution shown in Figure 25 indicates an even greater disparity of the mass flow from top to bottom. Also due to viscous effects the casing vanes will fail to reduce the tangential velocity even as much as shown in Figure 15.

The calculated wakes are also added to the flow at the exit to the stator vanes. Effectively the potential velocity distribution is multiplied by a wake deficit factor which will be greater than one between vanes and much less than one at the vane trailing edge location. The wakes will have different widths and depths due to the process of accounting for the wake diffusion prior to reaching the inducer leading edge. From Figure 16 it is obvious that the wakes at the hub streamline will be able to diffuse (or decay) substantially prior to entering the inducer, whereas the wakes at the tip streamline will remain narrow and deep. The wakes are diffused by introducing the streamwise distance between the vane exit station and the inducer station. This wake deficit factor was obtained in the following manner.

It was assumed that the leading edge of the inducer is located sufficiently downstream of the casing and stator vanes that the far wake equations may be used. Schlichting [10] developed an analytical solution for

the velocity profile in the far wake region using a mixing length concept. In the far wake region the velocity profile is of the form

$$\frac{V_\infty - V}{V_\infty} = \frac{\sqrt{10}}{18\ \beta}\left[\frac{S}{C_d\ \ell}\right]^{-1/2}\left[1 - \left(\frac{y}{b}\right)^{3/2}\right]^2 \tag{8}$$

where β is a constant that relates the mixing length to the wake width ($\beta = 0.18$),

S is the streamwise distance from the vane trailing edge,

y is the distance from the wake center,

b is the wake half width:

$$b = \sqrt{10}\ \beta(S\ C_d\ \ell)^{1/2} \quad \text{and} \tag{9}$$

C_d is a drag coefficient.

The term $C_d\ell$ is found from momentum consideration:

$$C_d\ell = 2\ \delta_{12}\left(\frac{V_1}{V_\infty}\right)^{3.2}, \tag{10}$$

where δ_{12} is the momentum thickness at the vane trailing edge and V_1/V_∞ is the local velocity at the same location. The momentum thickness, δ_{12}, is calculated by applying Truckenbrodt's energy-integral method [11] to calculate the turbulent boundary layer with a pressure gradient.

After the wake profiles are calculated they are repositioned at the trailing edge of the casing vanes. The mass flow at this location is corrected for the wake blockage by integrating Equation (8) to give

$$2\int_0^b \frac{V_\infty - V}{V_\infty}\,dy = (2b)\ (9/20)\ \frac{\sqrt{10}}{18\ \beta}\left[\frac{S}{C_d\ell}\right]^{-1/2}. \tag{11}$$

The average velocity deficit over the wake is given as

$$\Delta V = \frac{9}{20} \left[\frac{V_\infty - V}{V_\infty}\right]_{max} , \tag{12}$$

since for y = o at the wake centerline one has

$$\left[\frac{V_\infty - V}{V_\infty}\right]_{max} = \frac{\overline{10}}{18\ \beta} \left[\frac{s}{C_d\ \ell}\right]^{-1/2} . \tag{13}$$

The vane spacing is larger than the wake width so all velocities must be multiplied by the

$$\text{velocity factor} = \frac{9}{20} \frac{2b}{L} \left[\frac{V_\infty - V}{V_\infty}\right]_{max} \tag{14}$$

to account for wake blockage, where L is the spacing for a particular vane.

The effect of the calculated wakes on the potential flow field is shown in Figures 26 through 30 for the inlet casing vanes and the stator vanes. The wake half-width for each numbered vane calculated at the inducer inlet location is shown in Figure 31. Figure 32 shows the corresponding vane numbers.

By making use of the streamfunction in the circumferential direction, the flow is calculated downstream. Thus the wakes from the inlet casing vanes are transferred to the smaller radius; and, because of the residual tangential velocity, are shifted to larger values of θ. In several cases the two wakes combine to complicate the flow. For each of the wake distributions the massflow is integrated and checked. The curves will not all reach 180 degrees due to blockage of the boundary (fifth stator vane) at that point.

In a similar manner the wakes are transferred to the inducer station in Figure 33. The circumferential shift is more obvious when comparing this figure to the previous ones due to the reduction in radius and streamwise distances traveled by the flow.

3. Experimental Verification of Analysis

3.1 Rocketdyne Data

The prediction of the inlet flow to the inducer is a critical part of the damage analysis. The computational procedure has several key assumptions which need to be verified. The flow solution given in Figure 33 shows that the inducer inlet flow is non-uniform, producing large incidence variations which result in unsteady cavitation. This type of cavitation causes severe cavitation damage and high unsteady forces.

Rocketdyne [12] conducted a series of experiments on the SSME HPOTP inlet in air. For these experiments, a 5-hole probe [13] fabricated at ARL/PSU was utilized to obtain flow data in the inducer inlet plane. Total and static pressure, axial velocity and swirl angle were obtained as a function of circumferential angle at four radii. The axial velocity data are shown in Figure 34 and the swirl angle data are shown in Figure 35.

A brief comparison between the predicted flow field given in Figure 33 and the measured flow field given in Figure 34 shows similar trends. However the magnitude of the wakes are significantly different at the 2.23-inch radius. It is proposed that these differences are due to separation occurring along the wall in this wake region. The trends in the axial velocity with the radius and the circumferential location are in good agreement.

A better comparison is given in Figure 36 for the axial velocity and in Figure 37 for the swirl angle at the 1.977-inch radius. For this comparison the Rocketdyne data were integrated to obtain an average velocity which then was used to normalize the data given in Figure 34. These results are in excellent agreement.

3.2 Student Model Data

Three students from the Department of Aerospace Engineering designed, built and tested a 2-D model of the inlet casing. This work was part of an Undergraduate Thesis Program at The Pennsylvania State University.

A full-scale model of the casing was constructed as shown in Figures 38 and 39 with some modifications. The model was designed to be 2-D with uniform depth in the axial direction. All of the vanes were supported by pins so that their angle-of-attack could be varied. The shape of the throat area was the same as the inducer area on the turbopump. The inner throat and diffuser cone were made to rotate as a unit. This enabled a probe to be rotated circumferentially at the inducer inlet plane. A honeycomb was placed in the inlet to reduce incoming air turbulence.

Results of using fluorescent mini-tufts on the casing walls and vanes for flow visualization showed that separation was occurring. To eliminate this flow separation on the casing, suction was applied at various points along the wall to keep the boundary layer attached. Flow separation was also observed on several vanes.

Inducer inlet velocity data were obtained using a 5-hole probe. During these tests, the inlet flow velocity was approximately 175 ft/sec. The amount of suction required to maintain an attached casing boundary layer was set at a minimal value which was approximately 1% of the total flow.

A comparison between data obtained by Rocketdyne with the 3-D inlet casing and the student 2-D casing is given in Figure 40. Although the circumferential axial velocity profiles are in good agreement, the position and magnitude of the wakes are not.

4. Cavitation Analysis of Existing Design

4.1 Observed Damage

The locations of damage to the SSME-HPOTP are shown in Figures 3, 4, 5, 6, 41, 42 and 43. Since the damage that currently limits the life of the pump is the deep pitting on the inducer casing, (Figures 4 and 5) the causes and recommendations for reducing this damage are of primary consideration. The bands of cavitation damage on the casing (Figures 6 and 41), the light damage on the inducer blades (Figure 43), and the erosion of the inducer blade tips (Figure 3) will also be included in this analysis. The damage at the impeller exit (Figure 42) and possible causes for premature bearing failure will also be discussed.

The deep pitting on the inducer casing as seen in Figures 4 and 5 is concentrated downstream of the stator vanes mainly on the counterswirl side and to a less extent on the preswirl side. The damage could not be due to cavitation on the stator vanes, since the local cavitation number is too high for cavitation to occur. For the flow over the stator vanes the cavitation number can be defined as:

$$\sigma = \frac{P_\infty - P_v}{\frac{1}{2} \rho V_\infty^2} \tag{15}$$

where P_∞ and V_∞ are the local values of static pressure and velocity. At the trailing edge of the stator vanes for the 109% power level* $\sigma \approx 4.7$. This is much to high for any significant amount of cavitation. The damage must be due to other causes.

---

*Note: All damage calculations will be for the 109% power level unless stated otherwise.

The local cavitation number on the inducer blade can be defined as

$$\sigma = \frac{P_\infty - P_v}{\frac{1}{2} \rho W_\infty^2} \tag{16}$$

where W_∞ is the local relative velocity of the blade section. For uniform flow and no preswirl at the inducer blade, a value of $\sigma = 0.108$ was calculated. With a blade angle of 13.12° (r = 2.32 inches), the relative flow angle is 4.3° and a cavity length of approximately 33% of the chordlength should exist. The cavity length was approximated by the analysis discussed in Appendix A. At the hub a value of $\sigma = 0.318$ was found and the cavity length was calculated to be only 7% of the chord length. The calculated cavitation pattern for this 'steady state' condition is superimposed upon the measured damage on the inducer blades and is shown in Figure 44. The trailing edge of the cavity at the tip corresponds to the region of damage on the blade. For this uniform flow condition the damage should be produced equally around the circumference of the casing. But how then could the damage be concentrated at certain areas on the casing?

To answer this question the area where the damage is located provides part of the answer. In general the deep pits are downstream of the stator vanes. It is probable that, given the close proximity to the inducer leading edge, the wakes from the stators could be disturbing the flow. A decrease in axial velocity would increase the relative flow angle and thus the amount of cavitation. As the blades pass through these wakes some of the cavity is shed and the resulting collapses are creating the damage. For this reason the wake analysis was undertaken.

4.2 Cavitation Pattern Prediction

As a first approximation the cavity length calculation will be performed assuming steady-state conditions locally in the wake. The local flow velocity at the inducer blade location can be calculated using the data given in Figure 33. The axial and tangential velocity components and the flow angle were calculated through the wake for both preswirl and counterswirl sides of the pump. The cavitation number based on the local velocity on the blade was calculated using Equation (16). The cavity length was then calculated at points through the wakes using the analysis discussed in Appendix A.

The cavity length calculations for the existing turbopump design are shown in Figures 44 and 45 and in Table 3. It would be expected that the most erosion should occur for both the preswirl and counterswirl sides between 24° and 51°, downstream of casing vane 3 and stator vane 15 (see Figure 32). As the inducer blade rotates circumferentially there would be a negligible cavity prior to entering the wake region. A large cavity would grow on the blade surface as the wake center is reached. Upon leaving the wake the cavity would be shed from the blade. Table 3 and Figures 44 and 45 also indicate a growth in the cavity as it passes through the wakes downstream of casing vanes 5 and 6 and stator vane 16. For the preswirl condition the cavities exiting the wakes are longer than the cavities upon entering. The opposite is true for counterswirl. Thus, the volume of cavity shed should be larger on the counterswirl side of the pump. This correlates well with the observed damage patterns.

4.3 Damage Rate Model

The damage rate ($\dot{D}$) is a function of a distribution of bubble collapse energies, the material response to the bubble collapse, and the duration of exposure. A general expression for the damage rate would take the form :

$$\dot{D} = F\,(V_\infty^n,\ \alpha,\ \sigma/\sigma_D,\ \Delta\sigma(t),\ T_\infty,\ D_m,\ h) \cdot G(M,\ HT,\ D_G) \cdot H(t/t_o) \qquad (17)$$

where for hydrodynamic considerations,

V_∞ = reference velocity

α = total gas content of the liquid

σ/σ_D = normalized cavitation number

T_∞ = reference temperature

D_m = characteristic size

h = flow shape parameter

$\Delta\sigma(t)$ = time dependent cavitation number

for material response,

M = test material (includes erosion resistance and corrosion resistance)

HT = heat treatments of the material

D_G = grain size/microstructure of the material (due to method of fabrication, etc.)

and for the exposure time

t/t_o = dimensionless exposure time.

The total damage for cavitation damage sites would be

$$\dot{D}_T = \sum_{i=1}^{n} \dot{D}_i t_i \qquad (18)$$

and can be expressed as either a total volume loss or as a mean depth of penetration where the volume loss is divided by the damage area.

Equation (17) for a particular case is very difficult to determine due to the many variables; however, for the HPOTP some assumptions can be made. First of all, one is only interested in comparing damage rates due to changing flow conditions. Thus, the material response enters as a constant and Equation (17) reduces to

$$\dot{D} = F(V_\infty^n,\ \sigma/\sigma_D,\ \Delta\sigma(t))\ H(t/t_o) \quad . \tag{19}$$

For different flow conditions, the geometry of the pump also remains the same; however, the pump rpm and inflow conditions vary.

The heavy cavitation damage that occurs on the housing has been shown to be caused by the change in cavity length as the inducer passes through wakes. Therefore, the damage rate is going to be different for each wake encountered by the inducer and Equation (19) reduces to a solution of $\Delta\sigma(t)$ which is approximately the change in cavitation volume.

The change in cavity length as the inducer blade passes through a wake has been considered using a steady state analysis. It has been assumed that the cavity reaches a length corresponding to the incident flow at any point in the wake. If the wakes were large with respect to the blade chord this would be true. For the problem in question the wakes are narrow with respect to the chord and the time spent in a 20°-wide wake is approximately 0.1 millisecond. The cavity would thus not have time to reach a steady state condition. The actual volume of the cavity shed can only be estimated for this condition.

It will be assumed that (1) a steady state cavity is reached before the blade enters the wake and that a steady state cavity will exist some time after the blade passes through the wake, (2) a disturbance generated along the cavity wall will propagate with a velocity of $W_c = W_\infty \sqrt{1 + \sigma}$ which is the velocity along the free surface bounding a cavity, (3) the disturbance in the

cavity will follow a path corresponding to the flow at the leading edge where the disturbance was produced, and (4) the cavitation number is nearly constant through the wake.

As a blade with a steady-state cavity starts to move through a wake, the blade will see a fluctuating flow angle due to the reduced axial and tangential velocity at each position. The change in incident flow angle will therefore create a disturbance at the leading edge of the cavity. The disturbance will propagate at the fluid velocity along the cavity wall. The magnitude and direction of the velocity vector at the leading edge is a function of the position in the wake. If the width of the wake is less than the length of the cavity on the blade as it enters the wake, then the blade leading edge will reach the other side of the wake before the initial disturbance to the cavity shape reaches the cavity trailing edge. This is important since for the wake cavity model there is no closure condition specified at the trailing edge. A closure condition could be specified but is not required for the cases that will be investigated on the inducer blade.

The 'perturbed' cavity shape and shed volume can be calculated by the following procedure:

(1) The inducer blade leading edge is placed at the exit point of the wake.

(2) The flow angle and velocity at any point through the wake are used to calculate the cavity contour at the same point on the blade.

(3) The volume of the shed cavity is

$$\Delta Vol = Vol_{perturb} - Vol_{exit_{ss}} \quad .$$

Qualitatively, the results of such an analysis are shown in Figure 46. For case 2 in Figure 46, the steady-state cavity after passing through the wake is smaller than the cavity upon entering (typical counterswirl case for the wakes

from vanes 5 and 6). The shed cavity comes from two sources: the perturbation to the original cavity due to the wake, and the fact that the cavity volume must decrease even from the incident steady state condition. This occurs on the counterswirl side since the axial velocity is increasing as the inducer blades move from 180° to 0°. For case 3 in Figure 46 (wakes from vanes 5 and 6 on the preswirl side) the opposite is true. The cavity leaving the wake is typically larger than the cavity on the blade when entering the wake. Some of the volume in the 'perturbed' cavity must be used to 'fill' the cavity leaving the wake. If the wake is not very 'severe', there may be no shed cavity at all. As can be seen from Figures 6 and 41 for the casing damage, the erosion on the counterswirl side is much worse than on the preswirl side for the positions behind vanes 5 and 6 and stator vane 15.

For both preswirl and counterswirl sides the heaviest pitting was downstream of casing vane 3 and stator vane 15. The steady state cavities entering and leaving the wake are small (less than 0.1 ℓ/c) for both preswirl and counterswirl. Thus nearly all the cavity volume generated while the blade was in the wake would be shed. The analysis for this wake can be applied if the incident and exit cavities are neglected (this is done because no closure condition is used for the cavity wake model). This cavitation should be very severe since the entire 'perturbed' cavity is shed. The amount of damage can be approximated by the volume of the cavity shed.

Emphasis has been on damage from unsteady cavitation created when the inducer enters a wake. An analysis is presented in Appendix B which clearly shows that this type of damage is at least an order of magnitude greater than its steady cavitation counterpart.

4.4 Cavitation Damage at the Impeller Exit and Premature Bearing Failure

The cavitation damage at the impeller exit is due to the difference in pressure across the blade at the trailing edge. The high pressure fluid on the pressure side will flow towards the low pressure region on the suction side. Because of the sharp trailing edge geometry this flow will separate.

Even though the exit pressure is almost 5000 psia, the local cavitation number at this location is $\sigma = 0.818$ since the impeller tip speed is 878 ft/sec. This means that cavitation would occur in a separated region. Breaking the sharp edge at the impeller blade trailing edge by rounding the pressure surface should reduce this problem with a minimum loss in performance.

The premature bearing failure is likely due to the unsteady forces generated by the unsteady cavitation on the inducer blades. The proposed design change should also reduce this problem.

5. Recommendations for Cavitation Damage Reduction

5.1 Casing Vane Modifications

The analysis of the existing stationary vanes in the HPOTP clearly indicates that the vanes must be altered to improve the turbopump's cavitation performance and hence reduce cavitation damage. Modifications will strive to minimize the fluid turning at the inducer, equalize the massflow around the circumference of the inlet, and reduce the sensitivity to flow incidence. The last of these criteria will be considered first.

There is a bonafied reason to use airfoil shapes in the redesign of the inlet casing vanes. Regardless of the camber or amount of turning that a vane is to accomplish, typical vane shapes always employ a rounded leading edge and a sharp trailing edge. Due to the uncertainty in the exact angle at which the flow will encounter the vane at the leading edge, a rounded surface will allow

the flow to pass beyond the leading edge without flow separation on either the pressure or suction surface. The trailing edge is made as thin as possible to minimize the possibility of flow separation.

A standard NACA 65-0012 series vane shape was used as a base design for the new stationary vanes. The camber offset was increased for each vane until the desired amount of vane turning was produced. For this analysis the trailing edge thickness was set equal to zero. The thickness was added normal to either side of the camber line up to the maximum thickness at 30 percent of the chord. At this point it was then added to the suction side in an exponential manner until at the trailing edge all of the thickness was added to the suction surface.

The Douglas Neumann Cascade Program solves for the flow at any location in the cascade. Although the flow at the trailing edge must be in that direction, the inviscid flow between vanes can still exhibit a substantial degree of turning different from that indicated by the adjacent vanes. Thus some overturning may be required to direct the flow radially at the exit of the stationary vanes on the average.

Several redesigns were considered. Although the analytical results show that a substantial improvement in the flow field can be obtained, the vanes should not be considered a final design. As will be pointed out, the casing boundary plays a significant role in the guidance of the flow, and a new design should incorporate a redesign of the casing as well.

The stator vanes serve no useful purpose hydrodynamically. While they might be essential structurally, their presence in the flow field only serves to aggrevate the situation at the inducer because of their close proximity. The current redesign employs six vanes instead of four but makes them one-third shorter. The actual number and size of these vanes should be

dictated by structural considerations. The bottom stator vane should be incorporated into the redesign of the inlet casing boundary. While the new stator vanes will locally divert the flow, they will have no impact on the flow at the inducer and could readily be removed from the design considerations.

The inlet casing vanes were increased in number from 13 to 15. This will serve to maintain the force level on each vane since more turning will now be expected of the vane row to eliminate the tangential component of the velocity. They were spaced equally at their trailing edge (radius of 4 inches) between the top and the casing boundary at the bottom. The amount of turning was calculated to allow the flow to enter the vane row with no appreciable incidence and to exit radially. In some cases fluid turning angles close to 90 degrees was indicated. This is typical for inlets of this type where the flow is first directed tangentially by the casing near the upper inlet and then must be turned radially, effectively increasing the fluid turning before reducing it. Again, this emphasizes the important roll that the design of the casing boundary plays.

The vanes were uniformly decreased in chord length from the top casing vane, number 2 to the bottom vane, number 9. Vertical symmetry was employed to balance the side forces on the shaft. Obviously the downward force will still be substantial. The inviscid flow was calculated to produce radial flow at the radii corresponding to the inducer station, thereby eliminating any tangential velocity.

A typical vane shape of 45 points is illustrated in Figure 47. This vane is nondimensionalized by the chord and the dotted camber line illustrates how the thickness near the trailing edge is shifted towards the suction surface. In all, 22 bodies (vanes) are now used in the cascade with a total of 1092

points. The redesigned cascade took 2 1/2 hours to run on the computer. The flow solutions and new vane shapes are illustrated in Figure 48. The stators are now cut at the trailing edge at the same radius from inner to outer streamline and the wake flow produced by these two vane rows is shown in Figure 49. These wakes will be more diffused when they reach the inducer due to the increased distance between the stator trailing edge and the inducer leading edge.

The flow field at the inducer leading edge is shown in Figure 50. With the reduction of the tangential velocity the flow becomes more uniform at the inducer and the circumferential massflow distribution is nearly constant. Note that the casing boundary is still responsible for some fluid turning towards the bottom of the inlet at large values of θ. This turning can only be removed by redesigning the bottom of the inlet casing.

As can be noted in Figure 50, the deepest wakes are produced by the six stator vanes. It appears that due to the location of these vanes (in close proximity to the inducer leading edge) the wakes will always be the worst and perhaps be the controlling factor for cavitation damage. It is recommended that these vanes be removed if possible.

The vane shapes in Figure 48 were designed to produce radial flow by an inviscid flow analysis. Due to the viscous boundary layer, additional turning will have to be placed in the vanes to achieve the same turning as predicted by the inviscid solution. This is accomplished by adding the flow deviation angle to the blade camber angle. The leading and trailing edges were held in place (thus the chord remains constant) and the camber increased to include the fluid deviation angle. The camber offset distribution was altered to place most of the additional camber towards the trailng edge so as not to disturb the flow and hence the incidence angle at the vane leading edge. The

newly designed vanes with offset are illustrated in Figure 51. A typical vane is illustrated in Figure 51 and can be compared with Figure 47 to see the effects on the camber of the fluid deviation. Coordinate data for the redesigned vanes are given in Appendix C.

If it is required to thicken the trailing edges of the redesigned vanes, this thickness can easily be added to the suction surface as indicated by the dotted line in Figure 47. In this way the flow is still guided by the pressure surface and the vanes are thick enough to be cast.

The vane offsets were estimates from a deviation analysis similar to that discussed in Section 2.2. Using cascade data for the vanes in the casing is an approximation which has a high risk. The proposed vanes do more flow turning than the existing vanes and hence larger offsets are required. Due to the lack of available data for vanes in the accelerating flow created by the casing, it is strongly recommended that air tests be conducted to verify or adjust the vane geometry to meet the rquired flow performance.

5.2 Cavitation Damage Analysis

The cavity length calculations, based on the worst wakes, for the new designs with and without stator vanes are shown in Figure 53 and in Table 4. There are a number of improvements for both redesigns over the existing turbopump. These can be summarized as follows:

(1) The flow velocity is more uniform, thus the cavity lengths entering and leaving the wake are nearly equal.

(2) The velocity deficit is reduced significantly for the redesign with no stator vanes.

(3) The widths of the wakes are reduced.

The expected reduction in the rate of cavitation damage is proportional to the change in shed cavity volume. For the worst wakes, comparing the existing design to the redesign without stators.

$$\frac{\dot{D}_{old}}{\dot{D}_{new}} = \frac{(\text{shed cavity volume})_{old}}{(\text{shed cavity volume})_{new}} = 21.1 \quad . \tag{20}$$

6. Summary

A model has been developed that correlates the severe cavitation damage on the high pressure oxidizer turbopump (HPOTP) casing with the inducer unsteady cavitation. A computational procedure was used to analyze the flow through the inlet casing including the prediction of wakes downstream of the casing vanes. The predicted flow at the inducer inlet compares very favorably with the experimental data obtained by Rocketdyne.

The analysis of the HPOTP clearly shows that the inlet casing vanes must be altered to significantly reduce the cavitation damage rate. However, any redesign should reduce the vane sensitivity to flow incidence, equalize the distribution of the mass flow around the circumference of the inlet, minimize the swirl at the inducer inlet and, if possible, eliminate the stator vanes in front of the inducer.

Using the damage analysis presented, the damage rate for the proposed redesign is reduced by a factor of 21. The proposed redesign uses a conventional vane shape and the vanes are cambered more than the original vanes to significantly reduce the swirl component of the velocity. In addition, the inlet casing vanes were increased in number from 13 to 15 to reduce the forces on the vanes at the bottom of the casing.

The following conclusions can be made:

(1) The cavitation damage problem on the HPOTP results from the unsteady interaction of the inlet casing and stator vane wakes and the cavity flow over the inducer blades.

(2) The existing vanes produce separated flow and large wakes which combine to give severe velocity deficits at the leading edge of the inducer. Also, a significant amount of fluid turning exists downstream of the vanes.

(3) The stator vanes should be removed, if possible, due to their close proximity to the inducer blades.

(4) A redesign of the inlet casing vanes is required to greatly improve the cavitation damage rate occurring on the housing.

(5) A complete redesign should address the shape of the casing boundary as well.

(6) The redesign should also reduce unsteady cavitation and bearing forces.

An analysis was conducted which shows that the non-uniform flow entering the inducer causes the severe cavitation damage that exists in the HPOTP. The redesign of the stationary vanes is an initial attempt to significantly reduce the cavitation damage rate. It is strongly recommended that a series of tests be performed on any redesigned inlet casing to verify that the improvement in the cavitation damage rate will be met. These tests should be conducted along with continued efforts at refining the computational analysis.

7. Acknowledgments

This work was sponsored under Contract No. NAS8-34535 from the George C. Marshall Space Flight Center. Mr. Glen Wilmer, Jr. was the technical monitor of this program. The authors would like to thank Drs. R. E. Henderson and J. W. Holl on the Staff of the Applied Research Laboratory for their very

helpful discussions. Special appreciation is expressed to Dr. A. J. Acosta at the California Institute of Technology who served as a consultant.

References

[1] Silberrad, D., "Propeller Erosion," Engineering, p. 33, January 12, 1912.

[2] Hutton, S. P., "Cavitation Erosion - Where Do We Go From Here?," Proc. of Symposium on Cavitataion Erosion in Fluid Systems, ASME, Boulder, Colorado, June 1981.

[3] Knapp, R. T., "Recent Investigations of Cavitation and Cavitation Damage," Trans. ASME, 77, pp. 1045-1054, 1955.

[4] Stinebring, D. R., "Scaling of Cavitation Damage," M.S. Thesis, The Pennsylvania State University, ARL TM 76-51, 17 February 1976.

[5] Giesing, J. P., "Extension of the Douglas Neumann Program to Problems of Lifting, Infinite Cascdes," U.S. Department of Commerce, Report No. LB31653, AD 605207, Revised July 2, 1964.

[6] Yocum, A. M., "A Computer Program for Calculating Potential Flow Solutions for Flow Through Linear and Stationary Circular Cascades," Applied Research Laboratory TM 81-130, The Pennsylvania State University, June 1981.

[7] McBride, M. W., "A Streamline Curvature Method of Analyzing Axisymmetric Axial, Mixed and Radial Flow Turbomachinery," Applied Research Laboratory TM 77-219, The Pennsylvania State University, July 1977.

[8] Lieblein, S., "Experimental Flow in Two-Dimensional Cascades," NASA SP-36, 1965.

[9] Lakshminarayana, B., Discussion of Wilson, Mani, and Acosta's, "A Note on the Influence of Axial Velocity Ratios on Cascade Performance," NASA SP-304, Part I, 1974, pp. 127-133.

[10] Schlichting, H., Boundary-Layer Theory, 6th Edition, McGraw-Hill Book Company, New York, New York, 1968.

[11] Truckenbrodt, E., see Reference [10], pp. 634-644.

[12] Private Communication With Rocketdyne, letter dated 9 June 1983.

[13] Treaster, A. L. and Yocum, A. M., "The Calibration and Application of Five-Hole Probes," ISA Transactions, Vol. 18, No. 3, 1979.

[14] Stripling, L. B. and Acosta, A. J., "Cavitation in Turbopumps-Part 1," Trans. ASME, Vol. 84D, September 1962, pp. 326-338.

[15] Cumming, R. A., Dashraw, F. J. and Hackworth, J. V., "An Investigation of the Effects of Wake Nonuniformity on Cavitation Erosion Damage of Propellers," Proceedings of the Joint Symposium on Design and Operation of Fluid Machinery, Colorado State University, Ft. Collins, Colorado, June 12-14, 1978, 497-509.

[16] Wilson, M. B., McCallum, D. N., Boswell, R. J., Bernhard, D. D., and Chase, A. B., "Causes and Corrections for Propeller-Excited Airborne Noise on a Naval Auxiliary Oiler," DTNSRDC 83/097, ADA135731, November 1983.

Table 1

SPACE SHUTTLE MAIN ENGINE CHARACTERISTICS

Engine Operation	MPL - RPL - FPL
Thrust	
Vacuum	360K - 470K - 512K
Chamber Pressure	1957 PSIA - 3012 PSIA - 3283 PSIA
Area Ratio	77.5
Specific Impulse (Nom)	
Vacuum	455.2
Mixture Ratio	6.0
Life	7.5 Hrs 55 Starts
Specification Dry Weight	6957 Lbs

Table 2

HPOTP OPERATING CONDITIONS

Power Level	MPL	RPL	FPL
Percent Thrust Level	65	100	109
Pump Inlet Pressure, PSIA	3 4	377	390
Pump Inlet Temperature, °R	168	170	171
Pump Inlet Density, lb/ft^3	70.5	70.2	70.1
Pump Inlet Flowrate, lb/sec	712	1068	1160
Pump Disch Pressure, PSIA	2513	4290	4790
Pump Disch Temperature, °R	180	192	196
Pump Disch Density, lb/ft^3	70.6	70.3	70.2
Pump Head Rise, ft	4474	7915	8893
Pump Speed, RPM	20298	28349	30367
Pump Power, HP	8385	22571	27663

Table 3

Calculation of Cavity Lengths for the Existing Design
(Worst Wakes)
R = 2.37 Inches

	Position θ, Degrees	Flow Angle α, Degrees	Cavity Length / Chord Length	
Preswirl Side				
Entering Wake 3	24.3	-1.1	0.08	Pressure Side
In Wake 3	35.9	6.4	0.40	Suction Side
Leaving Wake 3	50.7	0.2	0.02	Suction Side
Entering Wake 5	81.9	2.2	0.20	Suction Side
In Wake 5	88.7	7.0	0.43	Suction Side
Leaving Wake 5	95.4	3.2	0.27	Suction Side
Entering Wake 6	95.4	3.2	0.27	Suction Side
In Wake 6	110.4	8.1	0.46	Suction Side
Leaving Wake 6	121.9	4.1	0.34	Suction Side
Counterswirl Side				
Entering Wake 3	50.7	1.3	0.08	Suction Side
In Wake 3	35.9	6.5	0.40	Suction Side
Leaving Wake 3	24.3	0.1	0.00	Suction Side
Entering Wake 5	95.4	4.3	0.35	Suction Side
In Wake 5	88.7	7.5	0.44	Suction Side
Leaving Wake 5	81.9	3.6	0.30	Suction Side
Entering Wake 6	121.9	4.7	0.36	Suction Side
In Wake 6	110.4	8.5	0.47	Suction Side
Leaving Wake 6	95.4	4.3	0.35	Suction Side

Table 4

Calculation of Cavity Lengths for the New Designs
(Worst Wakes)
R = 2.37 Inches

	Position θ, Degrees	Flow Angle α, Degrees	Cavity Length / Chord Length
Without Stators	51.2	3.6	0.30
	55.6	6.0	0.39
	59.6	3.6	0.30
With Stators	80.8	3.8	0.32
	85.2	7.0	0.43
	87.5	3.8	0.32

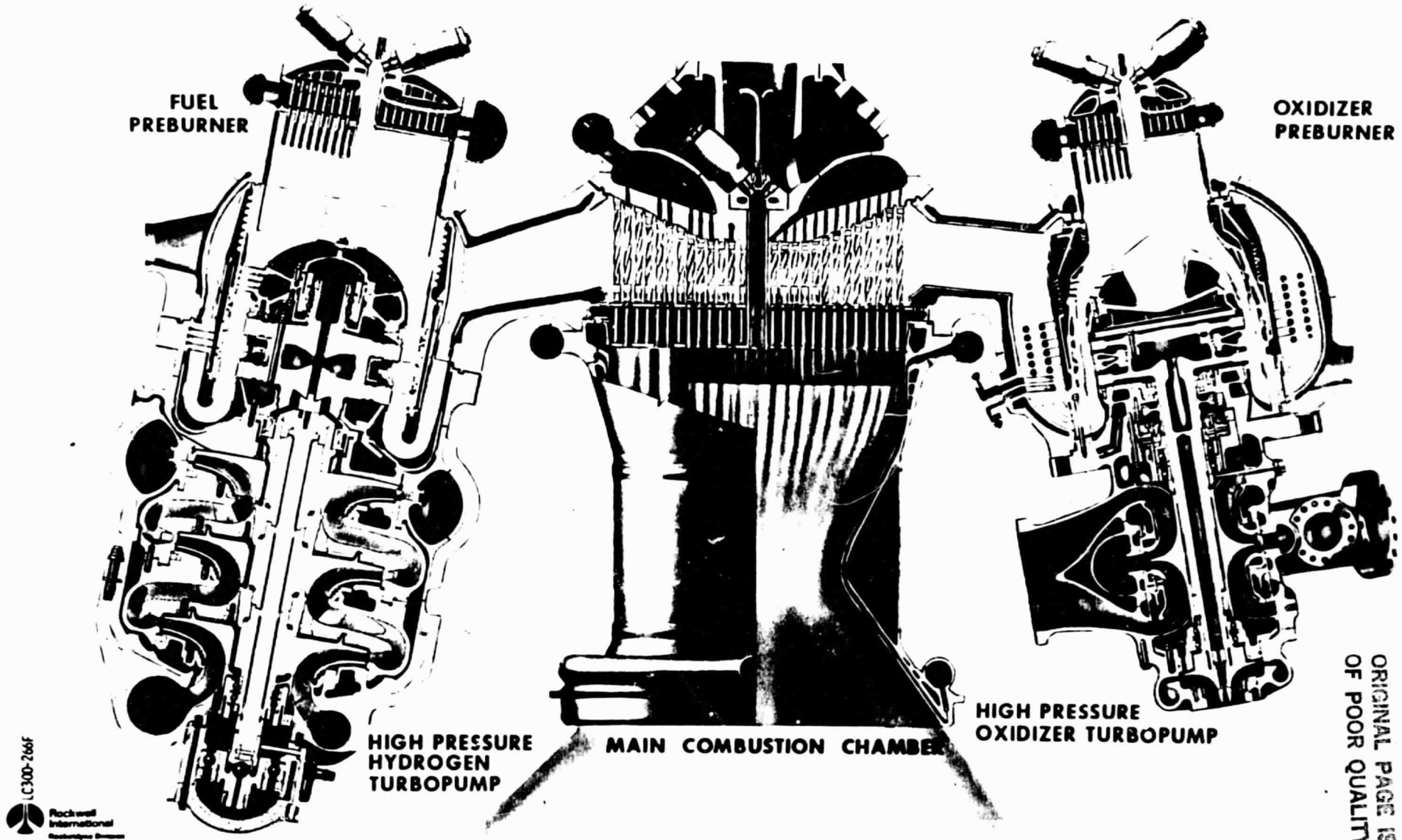

Figure 1. SSME Powerhead Component Arrangement (Rocketdyne)

HIGH PRESSURE OXYGEN TURBOPUMP

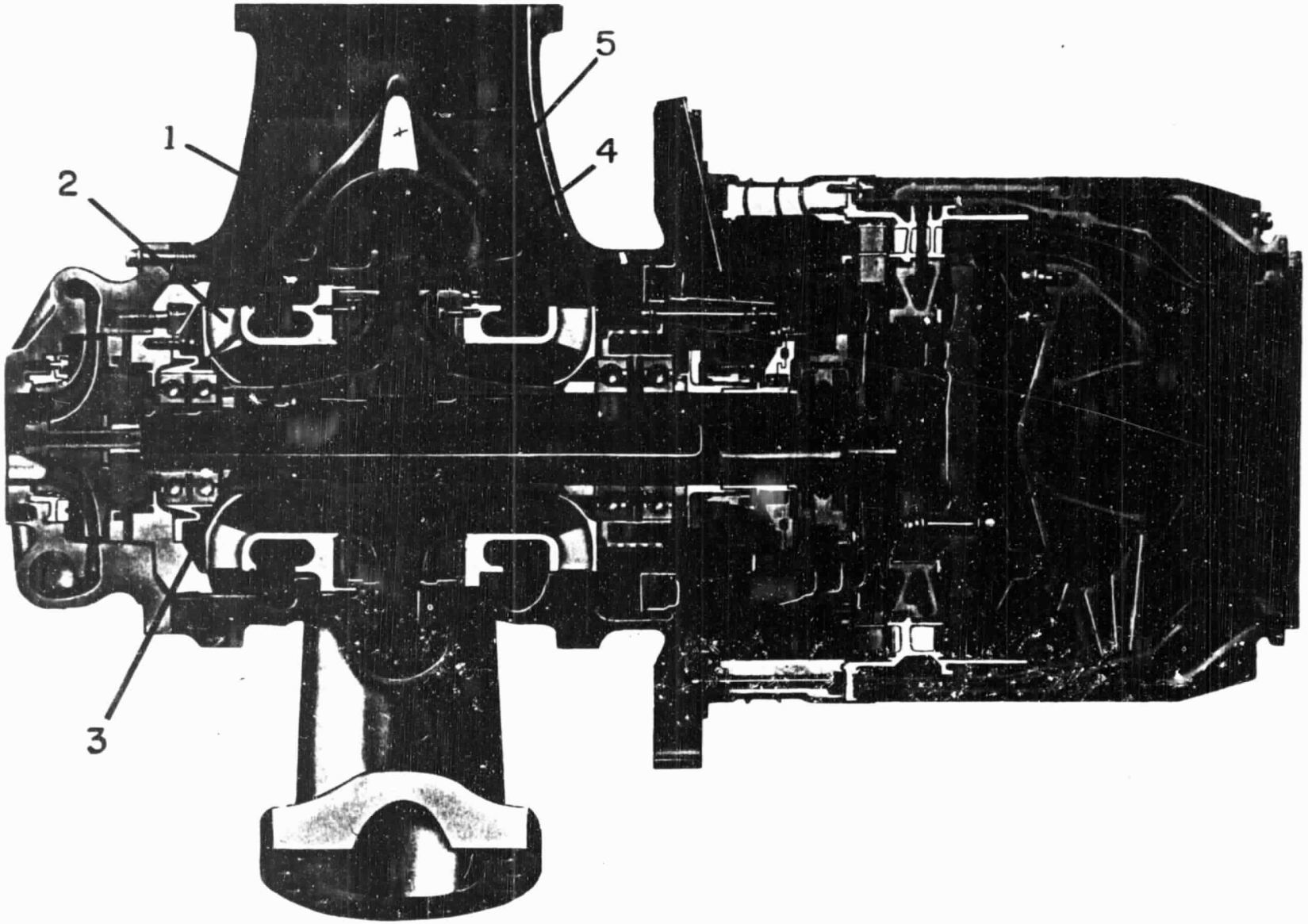

LC301-3801

Rockwell International

Figure 2. Schematic of the HPOTP (Rocketdyne)

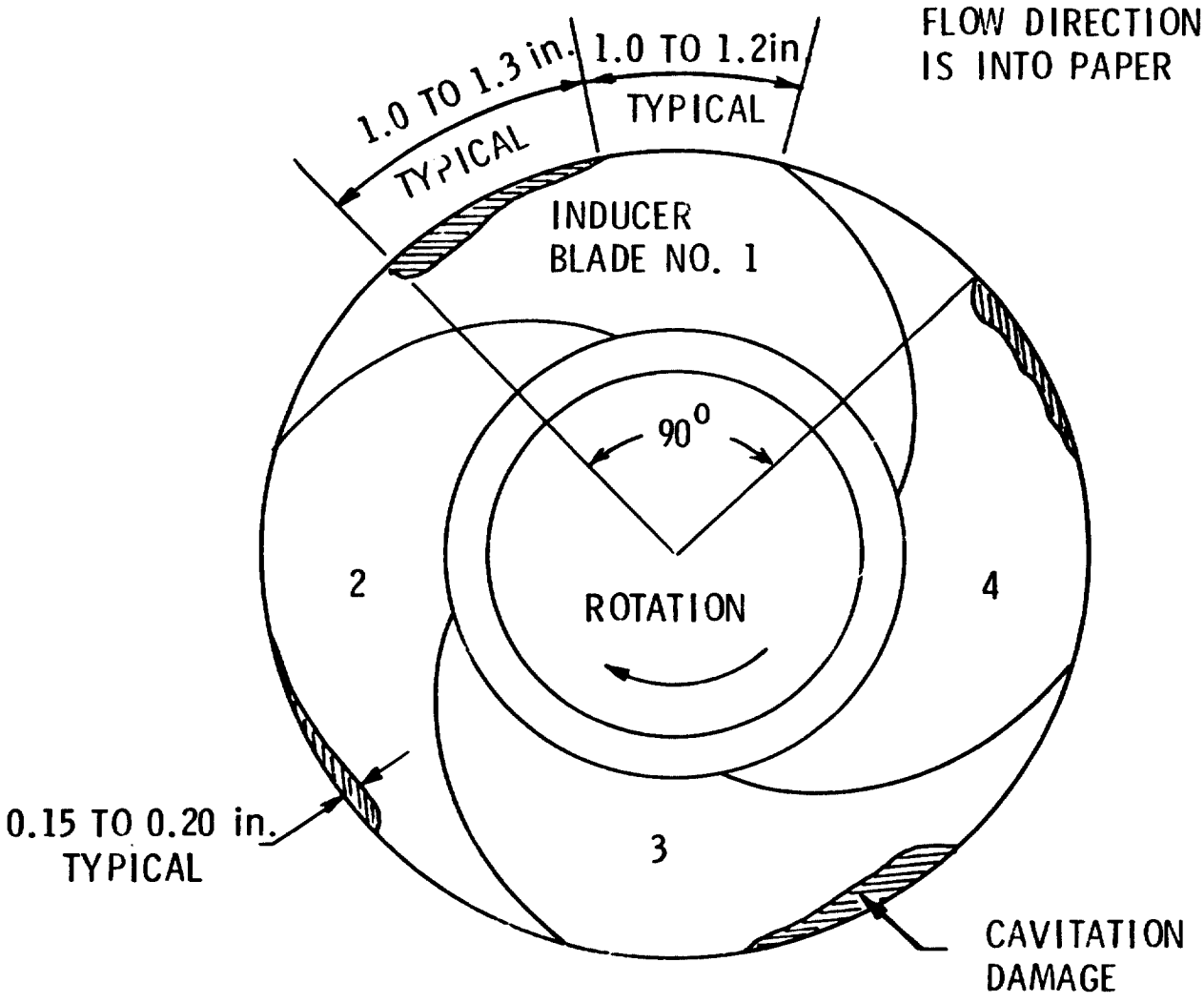

Figure 3. HPOTP Main Impeller Cavitation Damage Regions on the Inducer Blades (Rocketdyne)

Figure 4. HPOTP Inlet Vane Cavitation Damage Regions (Pocket Type)

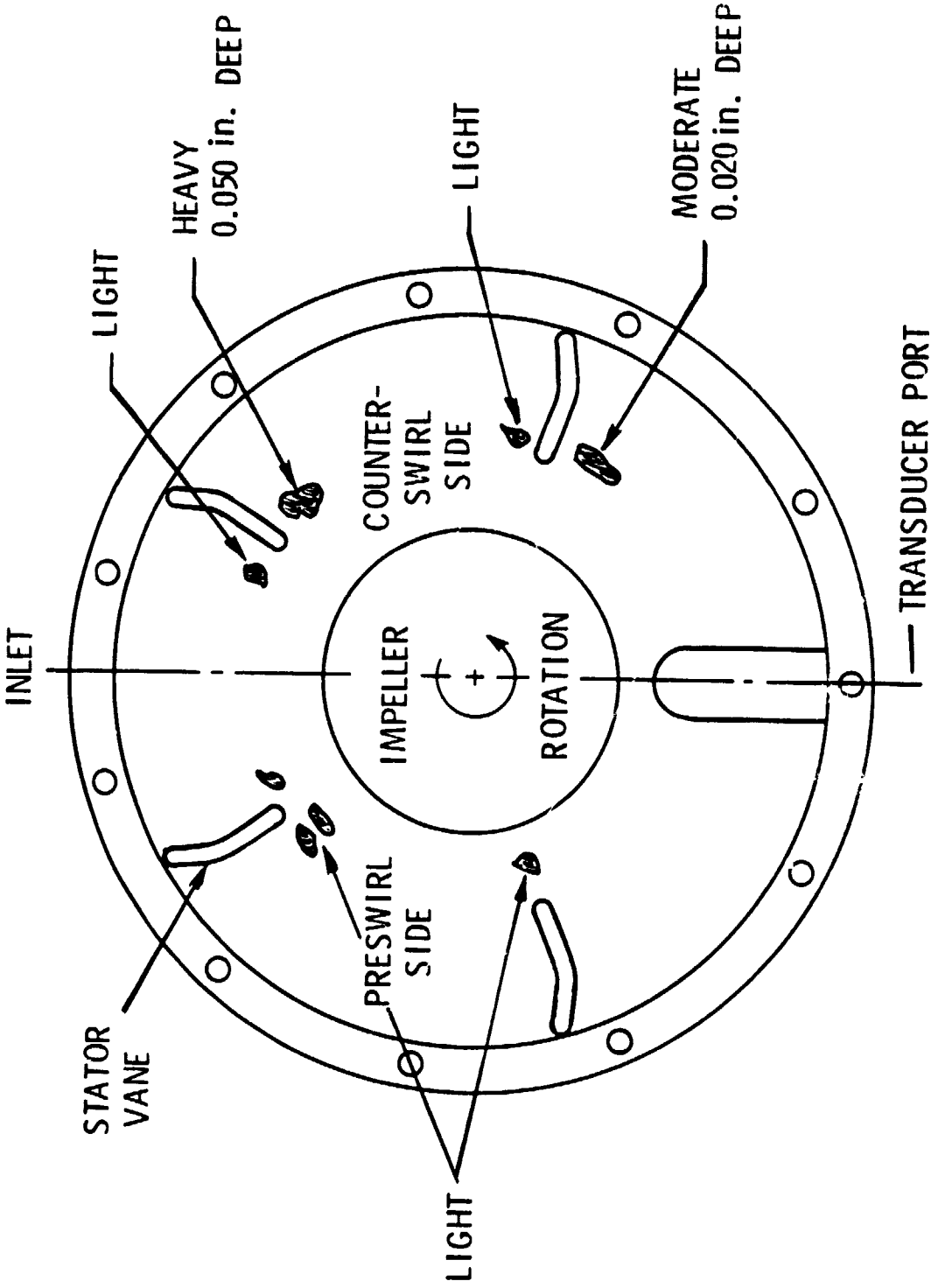

Figure 5. HPOTP Rail. Vane Cavitation Damage Regions (Rocketdyne)

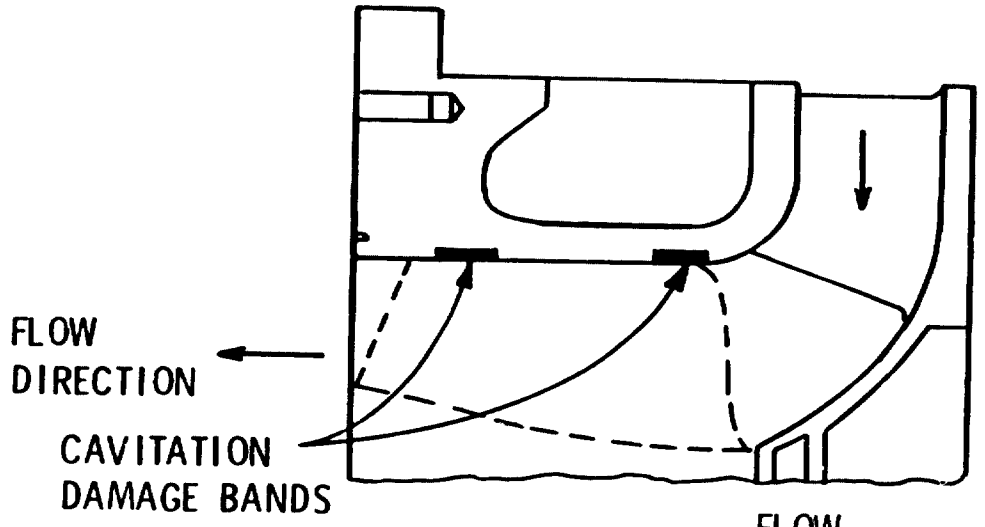

ALL DIMENSIONS
IN INCHES

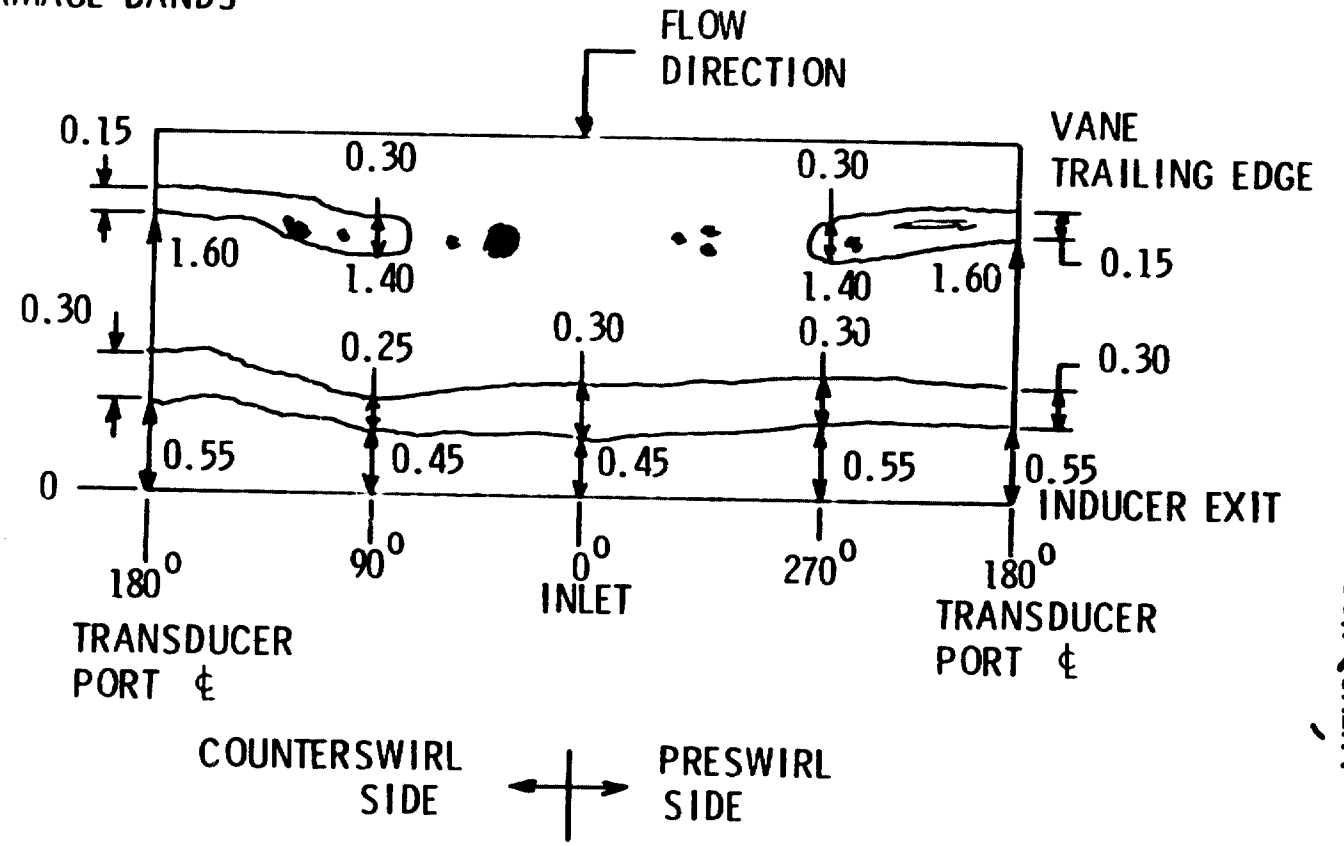

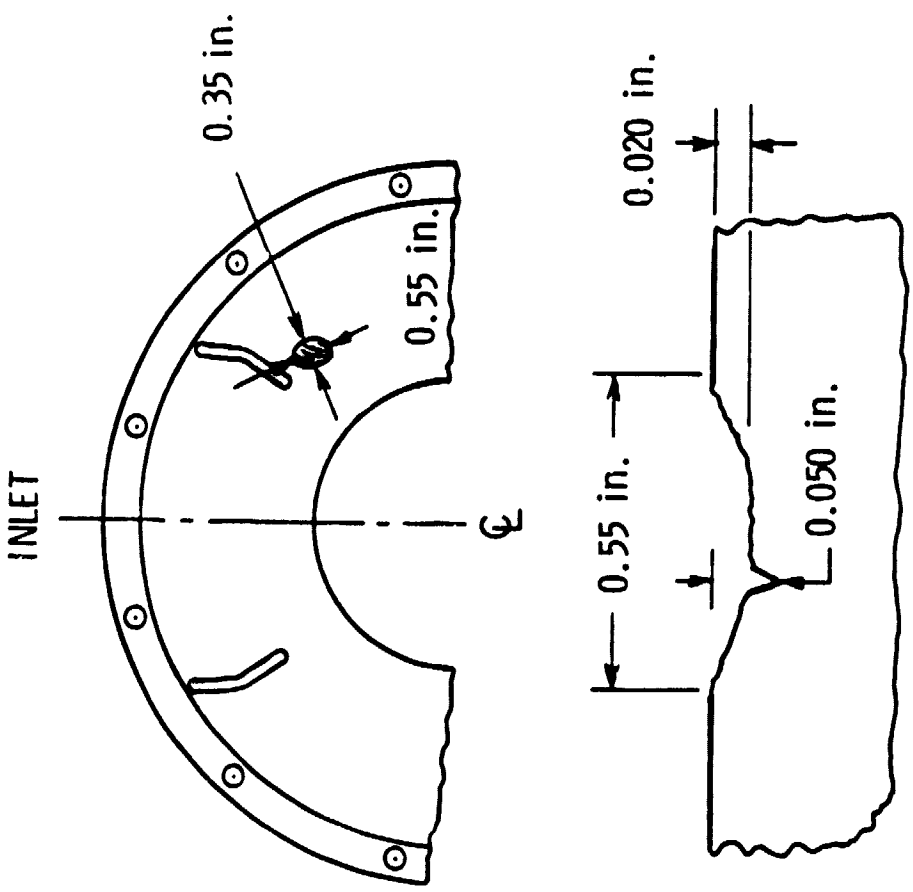

Figure 7. Typical [illegible] Installation [illegible] and Characteristics (Roughness)

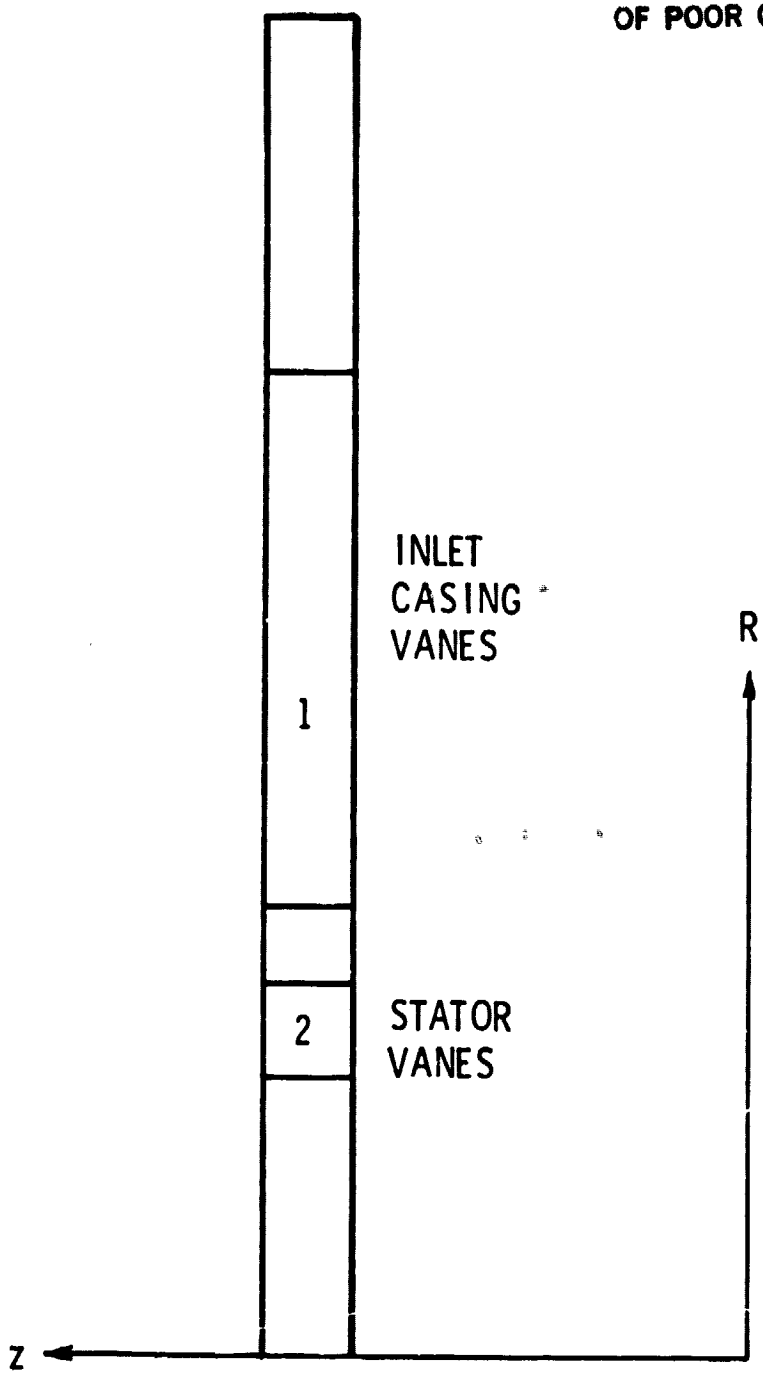

SCALE: 1" = 1.67'

Figure 8. Side View of the 2-Dimensional Model of the Inlet Casing

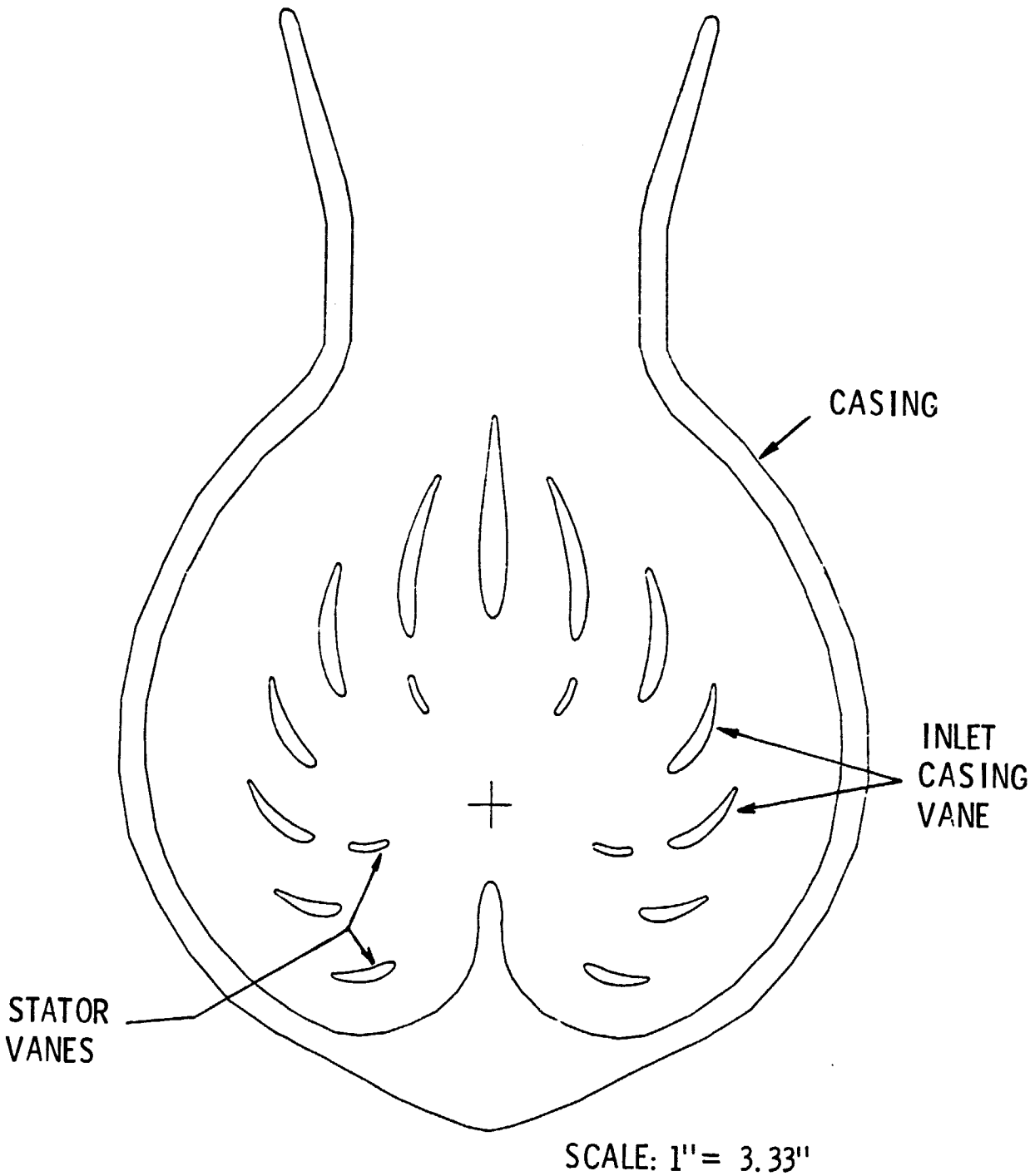

Figure 9. Front View of the 2-Dimensional Model of the Inlet Casing

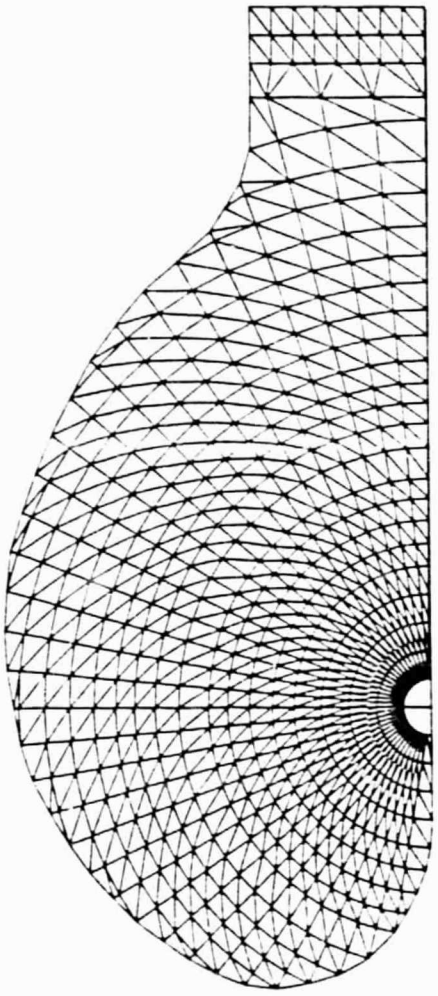

SCALE: 1" = 3.33"

Figure 10. Finite Element Grid

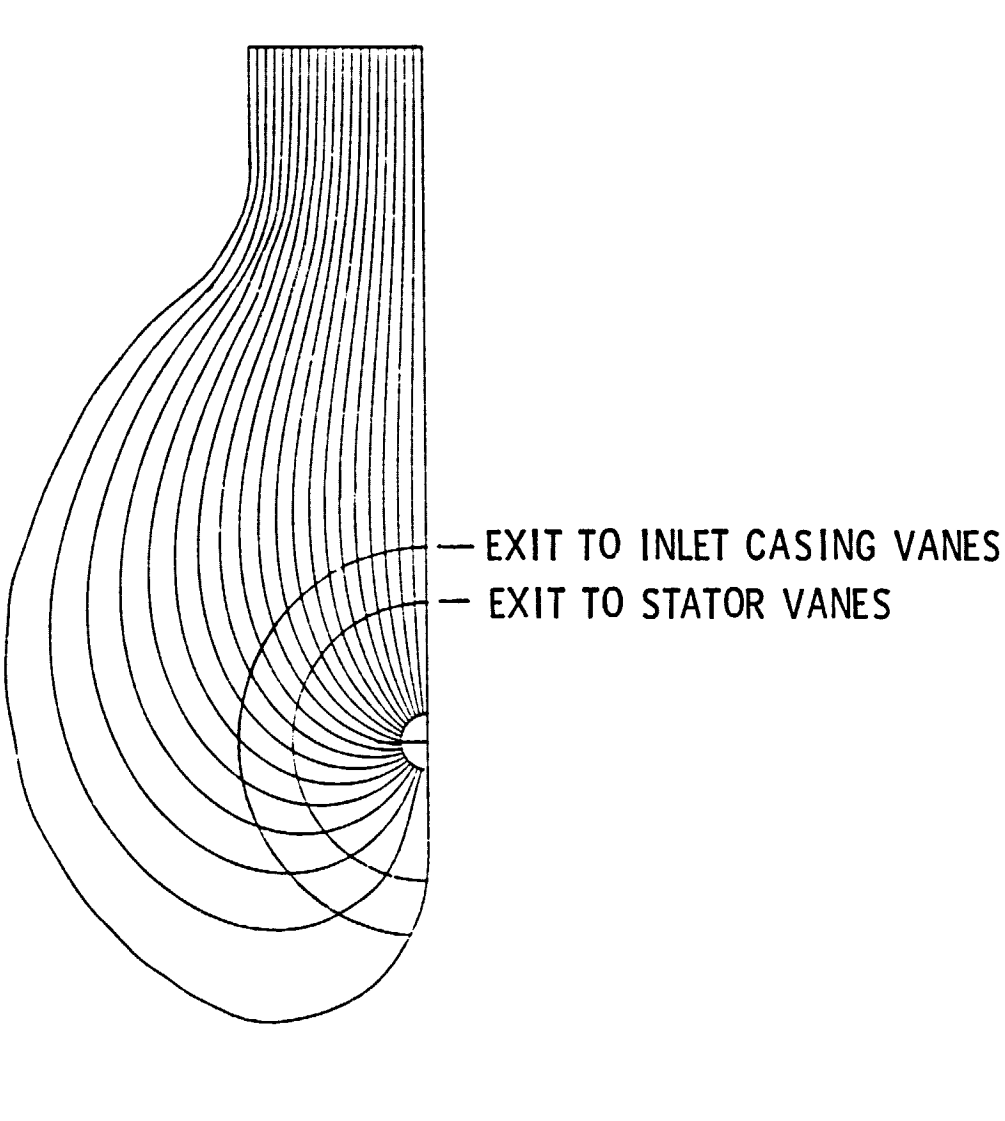

Figure 11. Finite Element Solution for the Inlet Casing

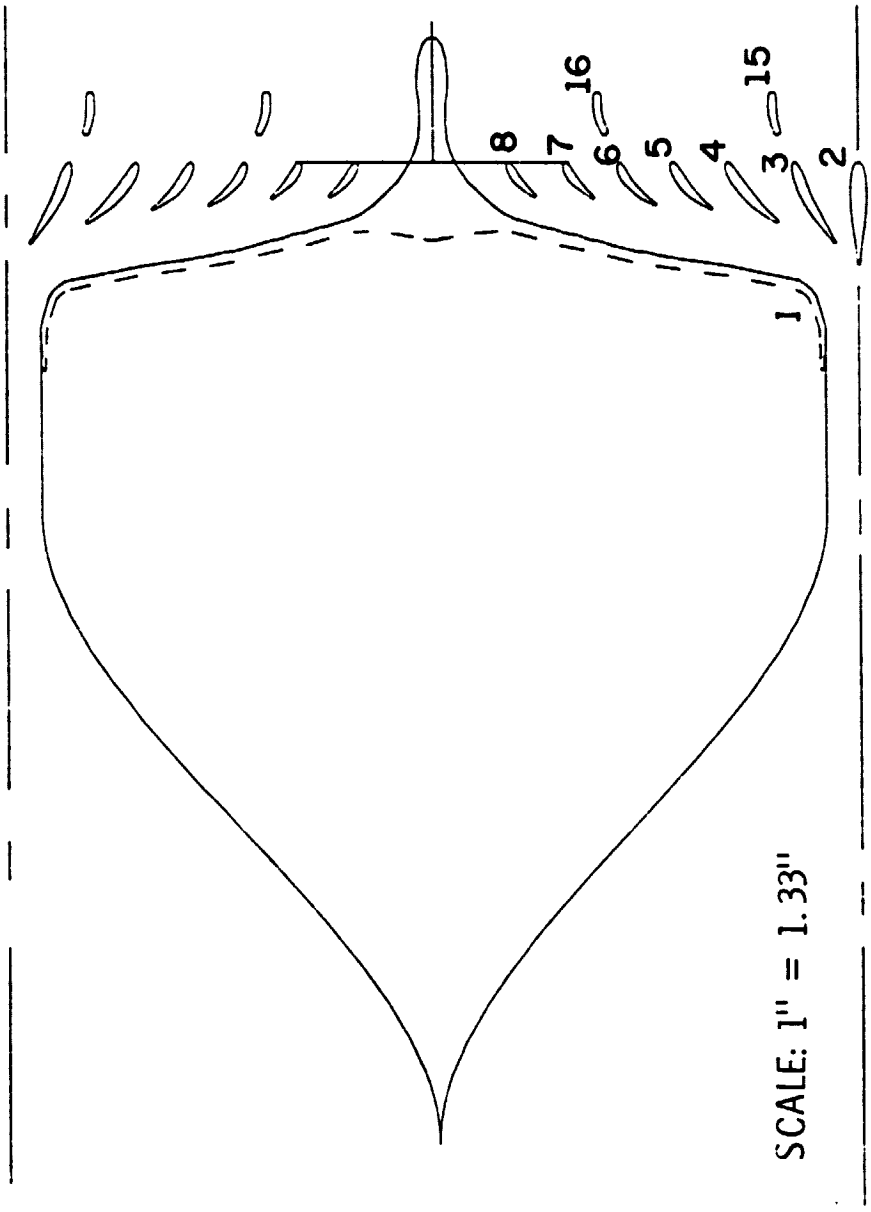

Figure 12. Transformed Cascade With Guide Vanes

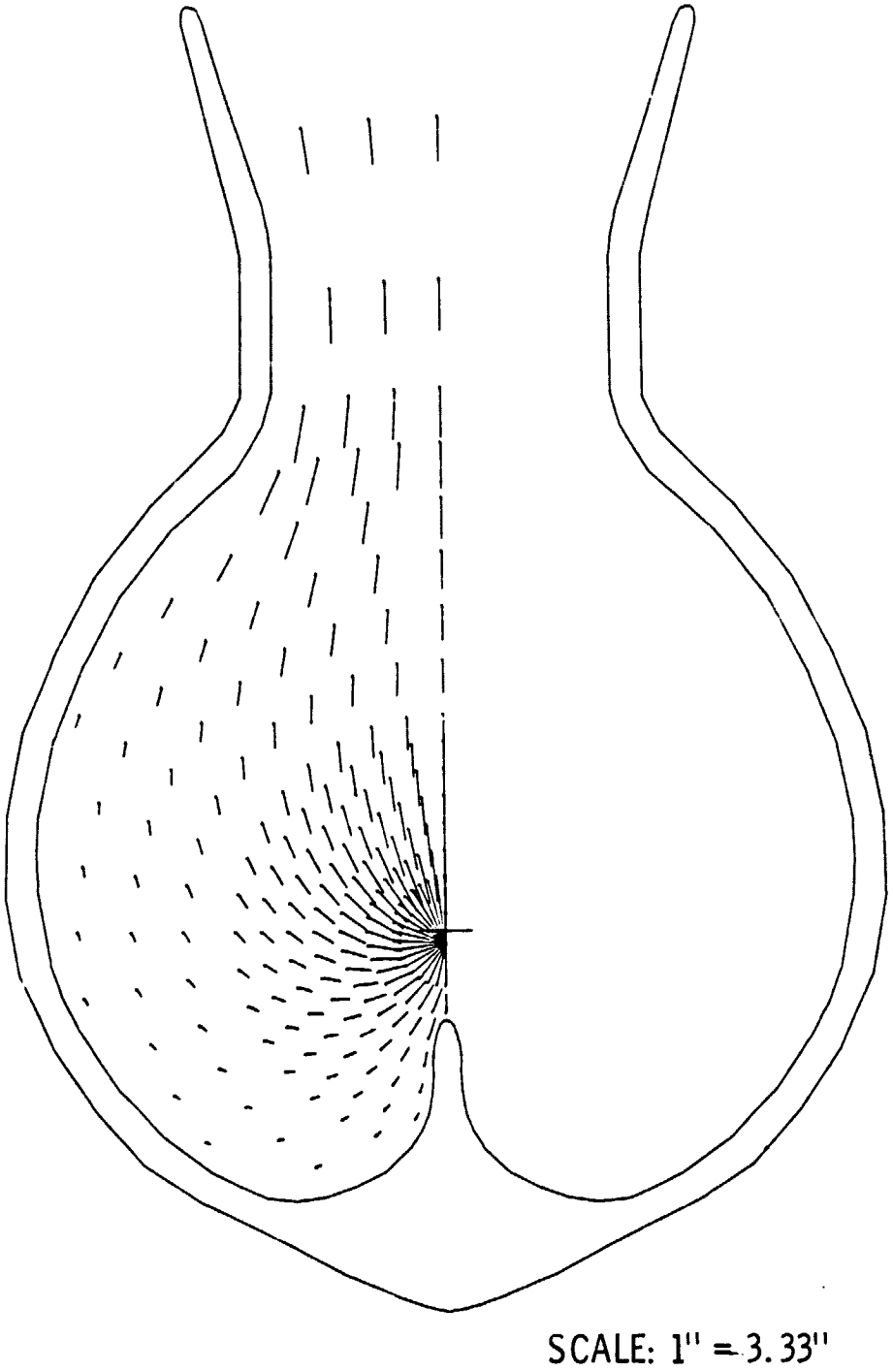

Figure 13. Flow Solution for the Inlet Casing Only

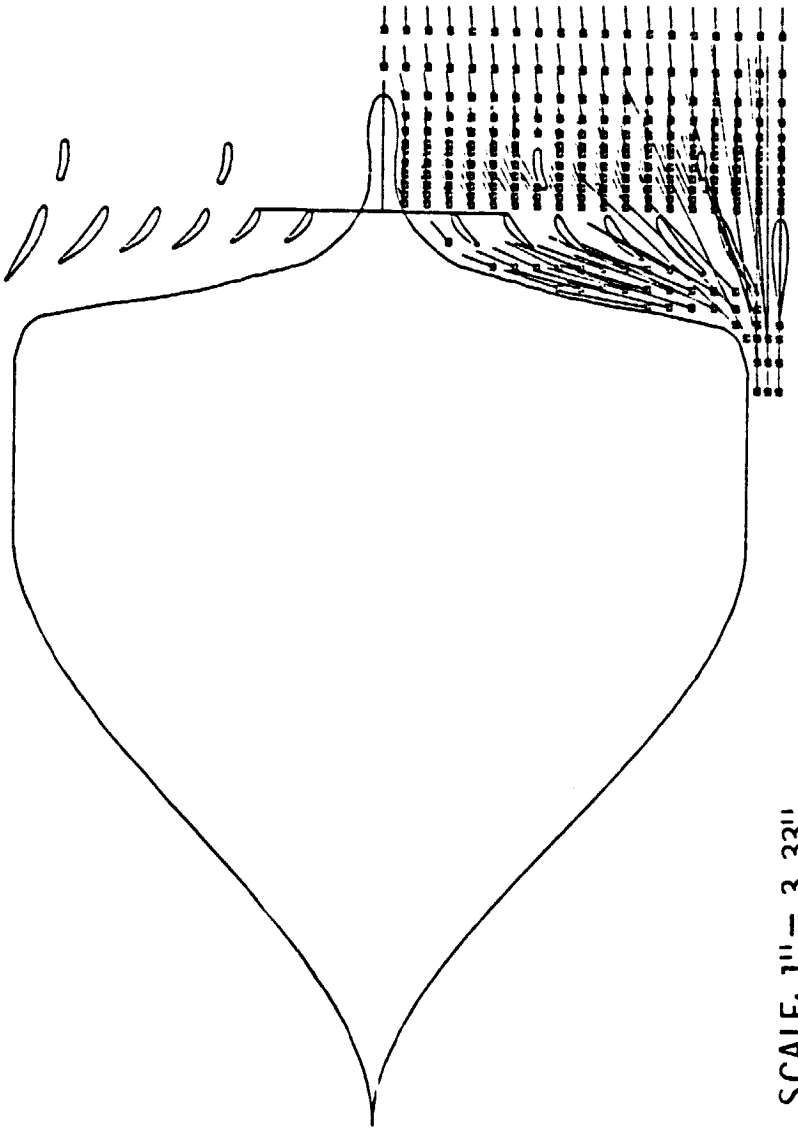

Figure 14. Flow Solution in the Transformed Plane for the Casing With Guide Vanes

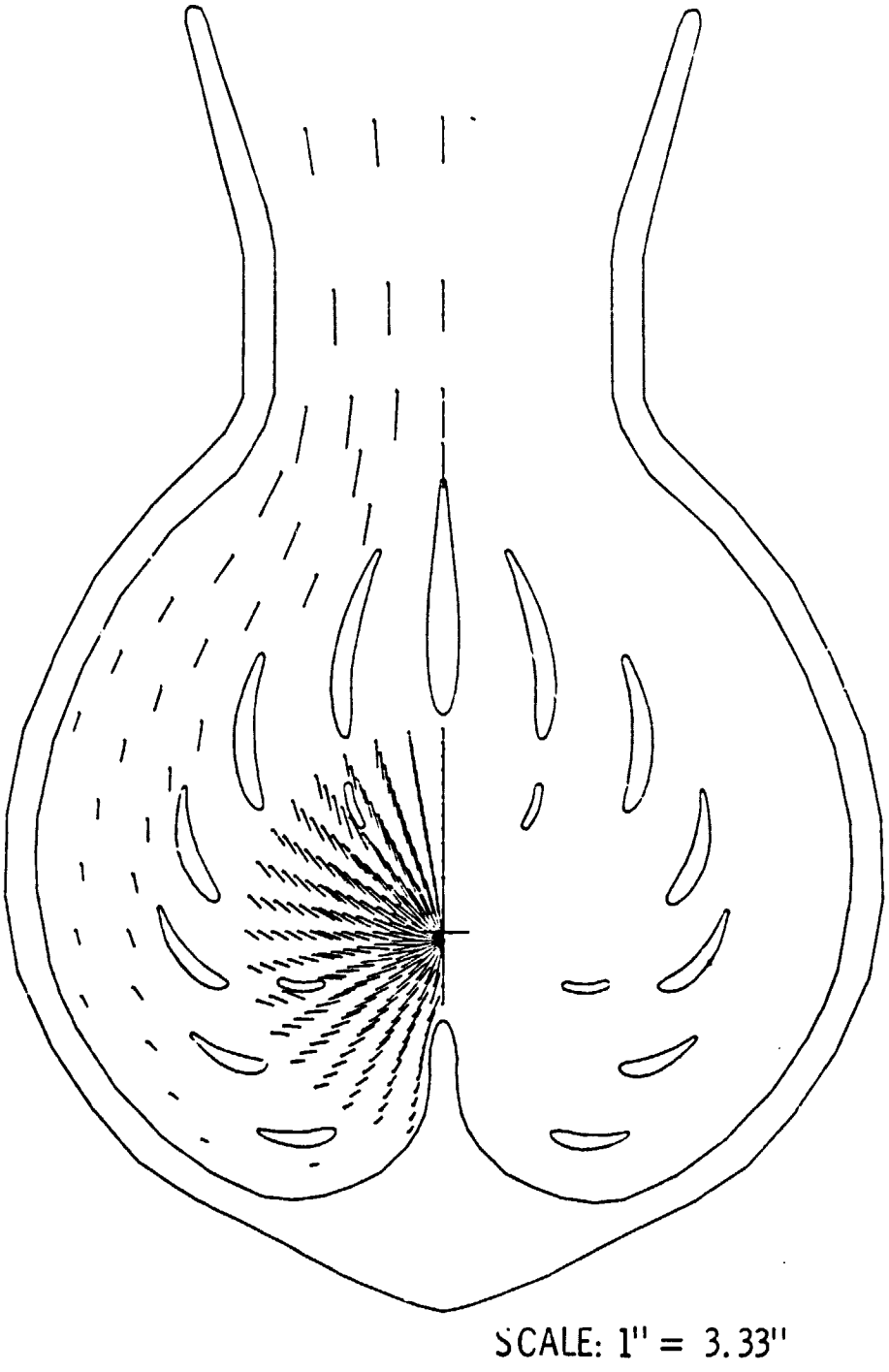

Figure 15. Flow Solution for the Casing With Guide Vanes

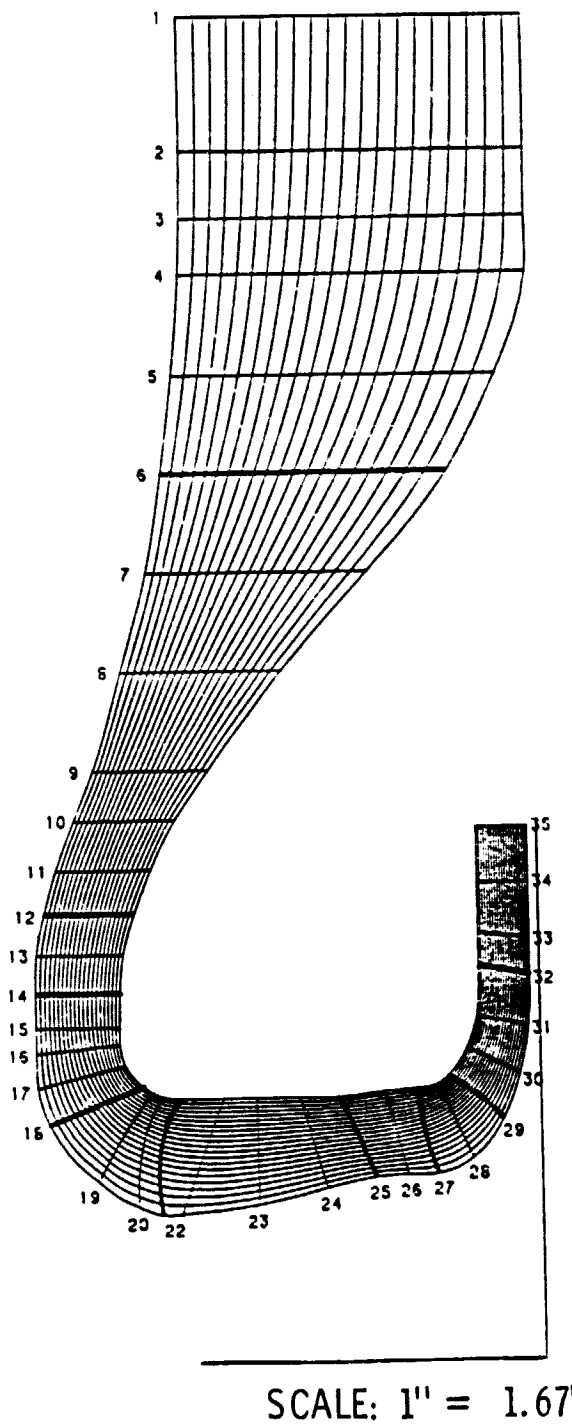

Figure 16. Streamline Curvature Solution for the Flow Through the Turbopump

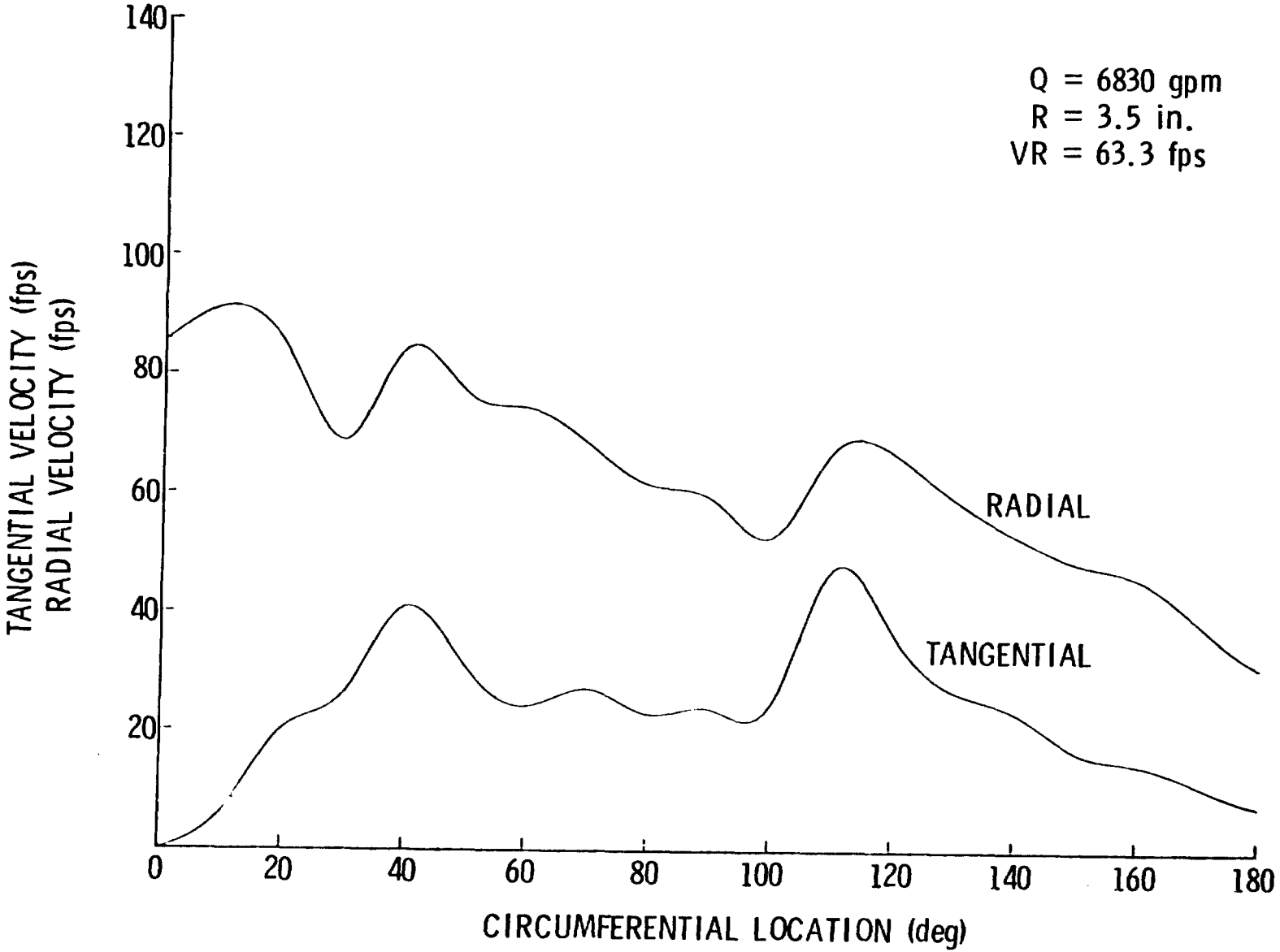

Figure 17. Cascade Potential Flow Solution at R = 3.5 Inches

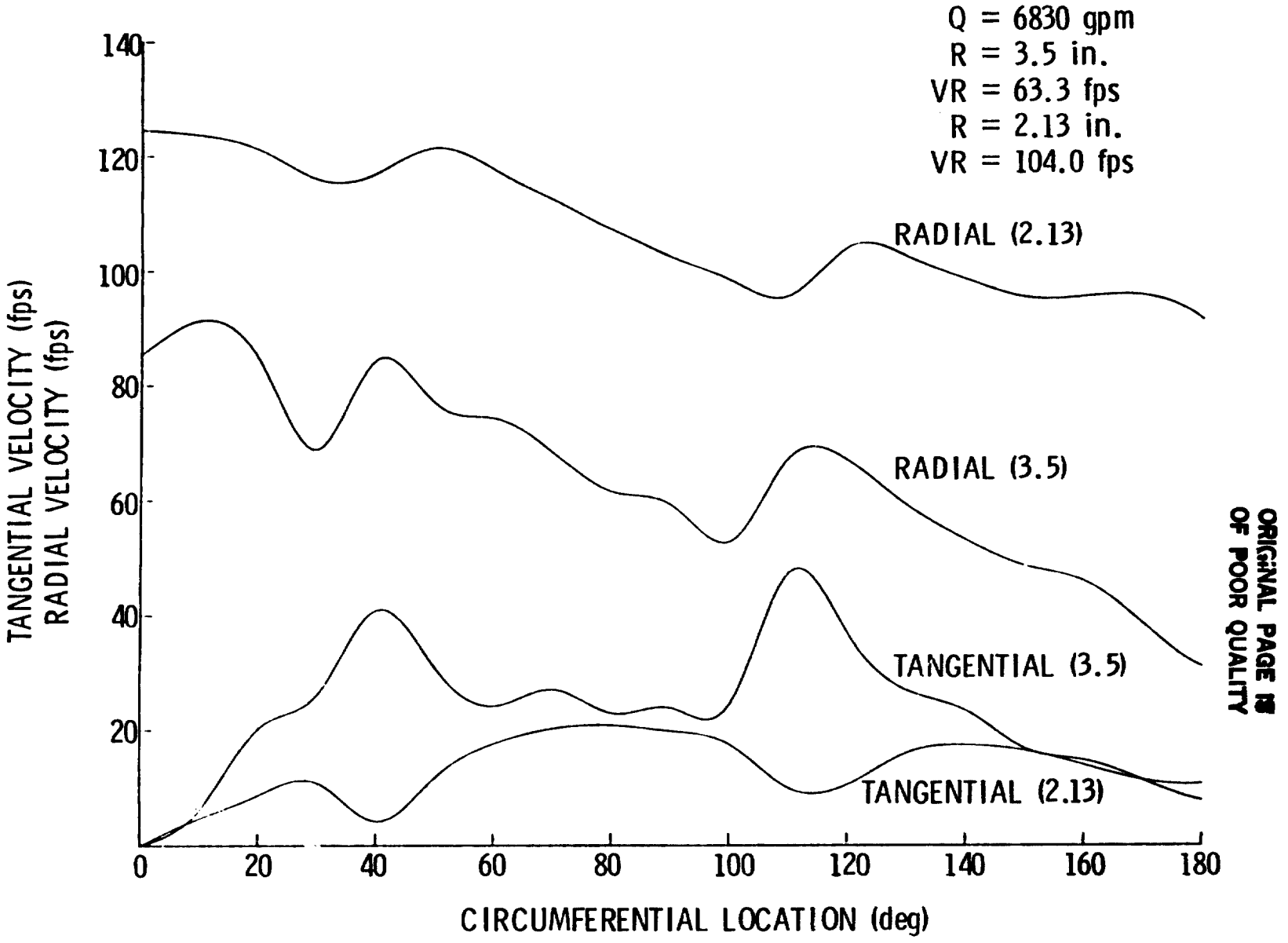

Figure 18. Cascade Potential Flow Solution at R = 2.13 Inches

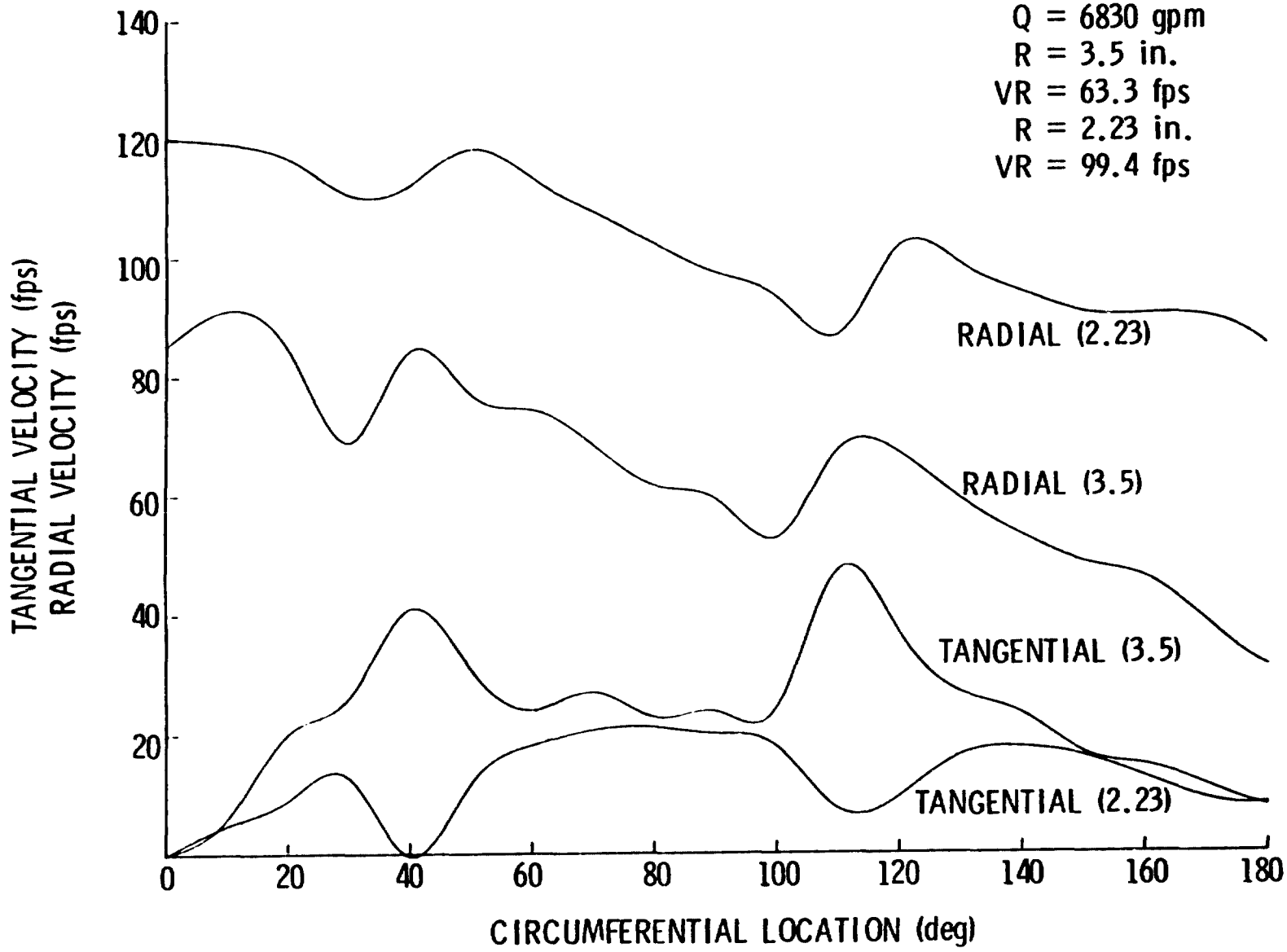

Figure 19. Cascade Potential Flow Solution at R = 2.23 inches

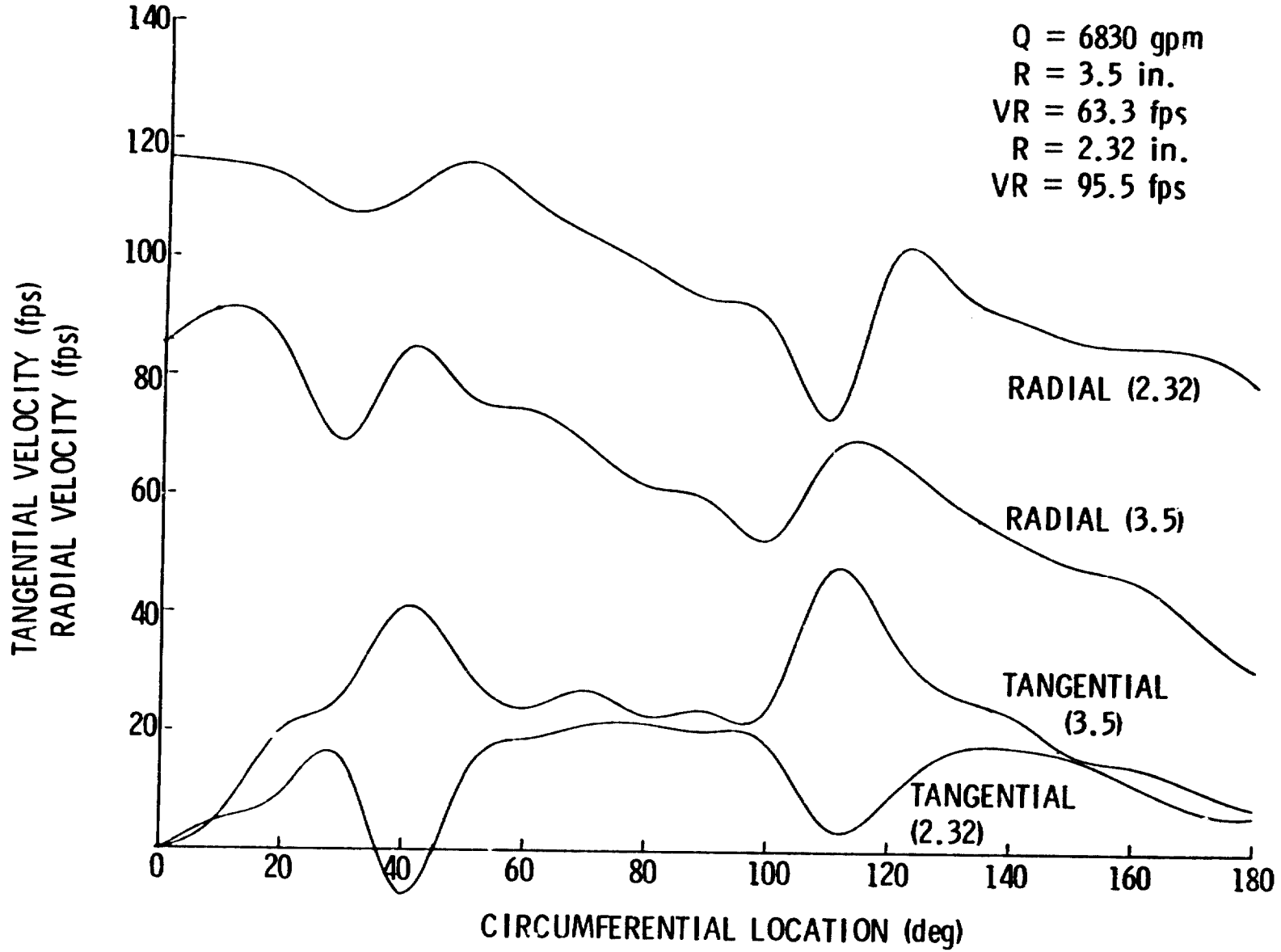

Figure 20. Case de Potential Flow Solution at R = 2.32 Inches

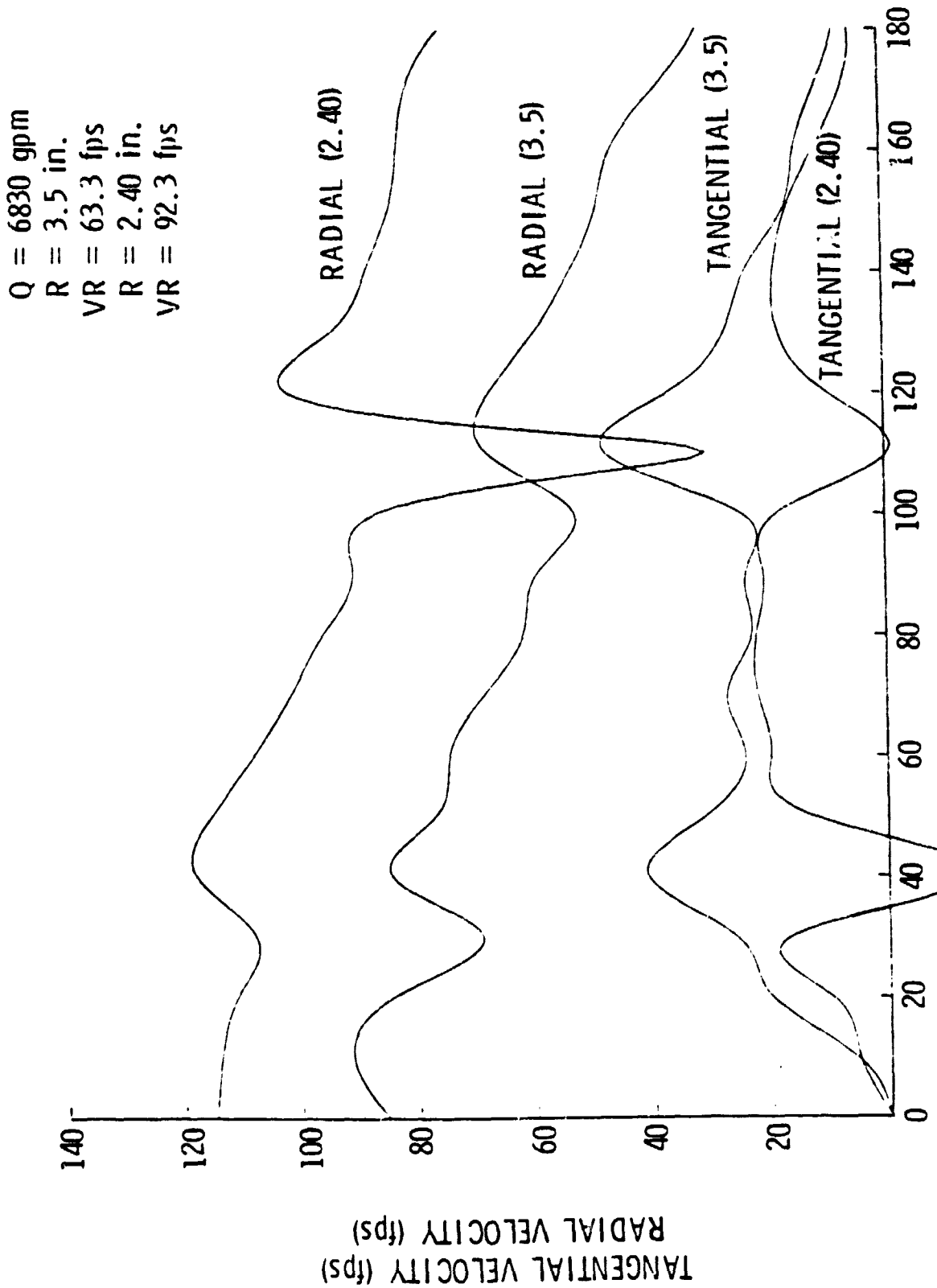

Figure 21. Cascade Potential Flow Solution at R = 2.40 Inches

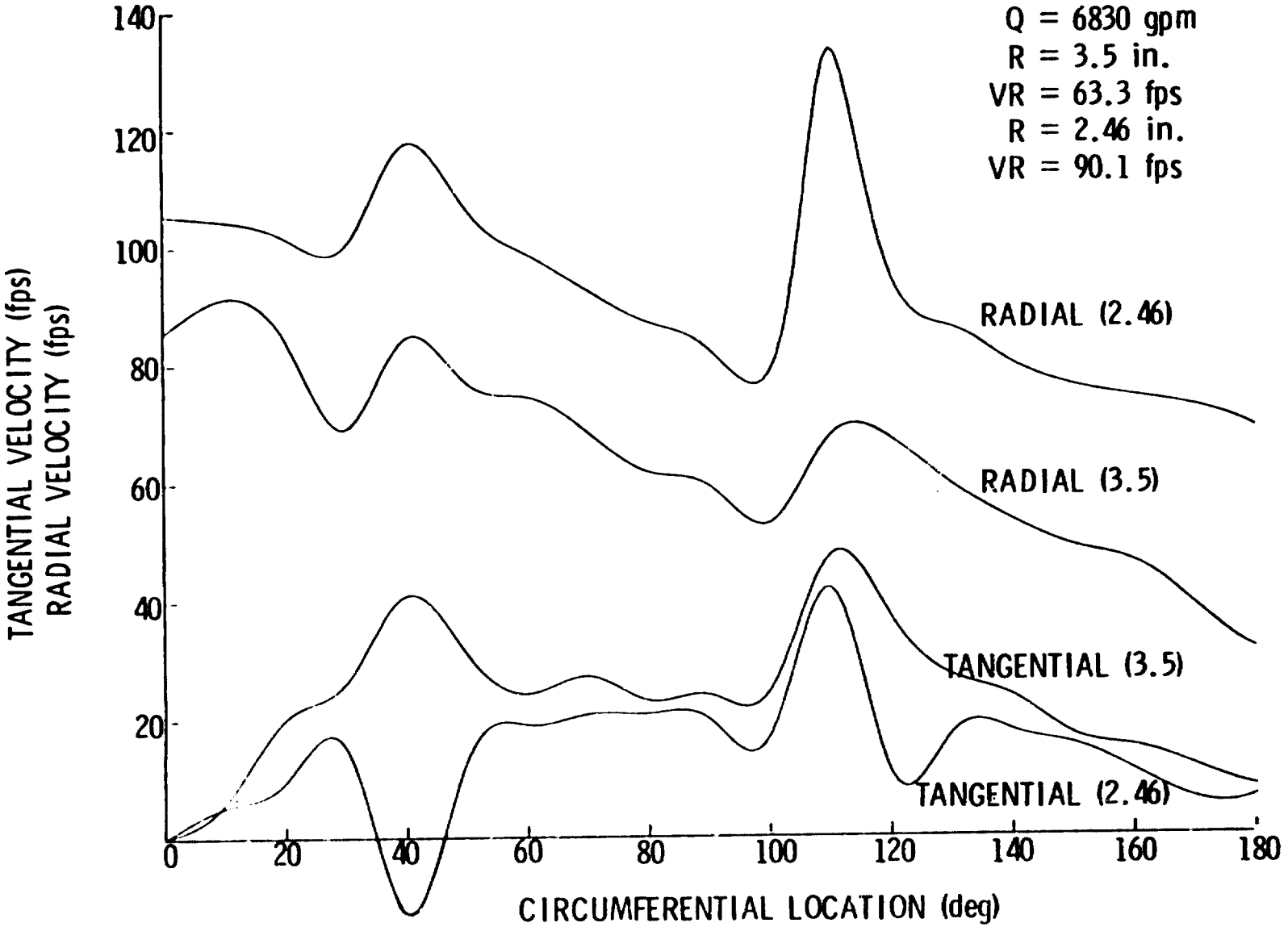

Figure 22. Cascade Potential Flow Solution at [illegible] Inches

ORIGINAL PAGE IS
OF POOR QUALITY

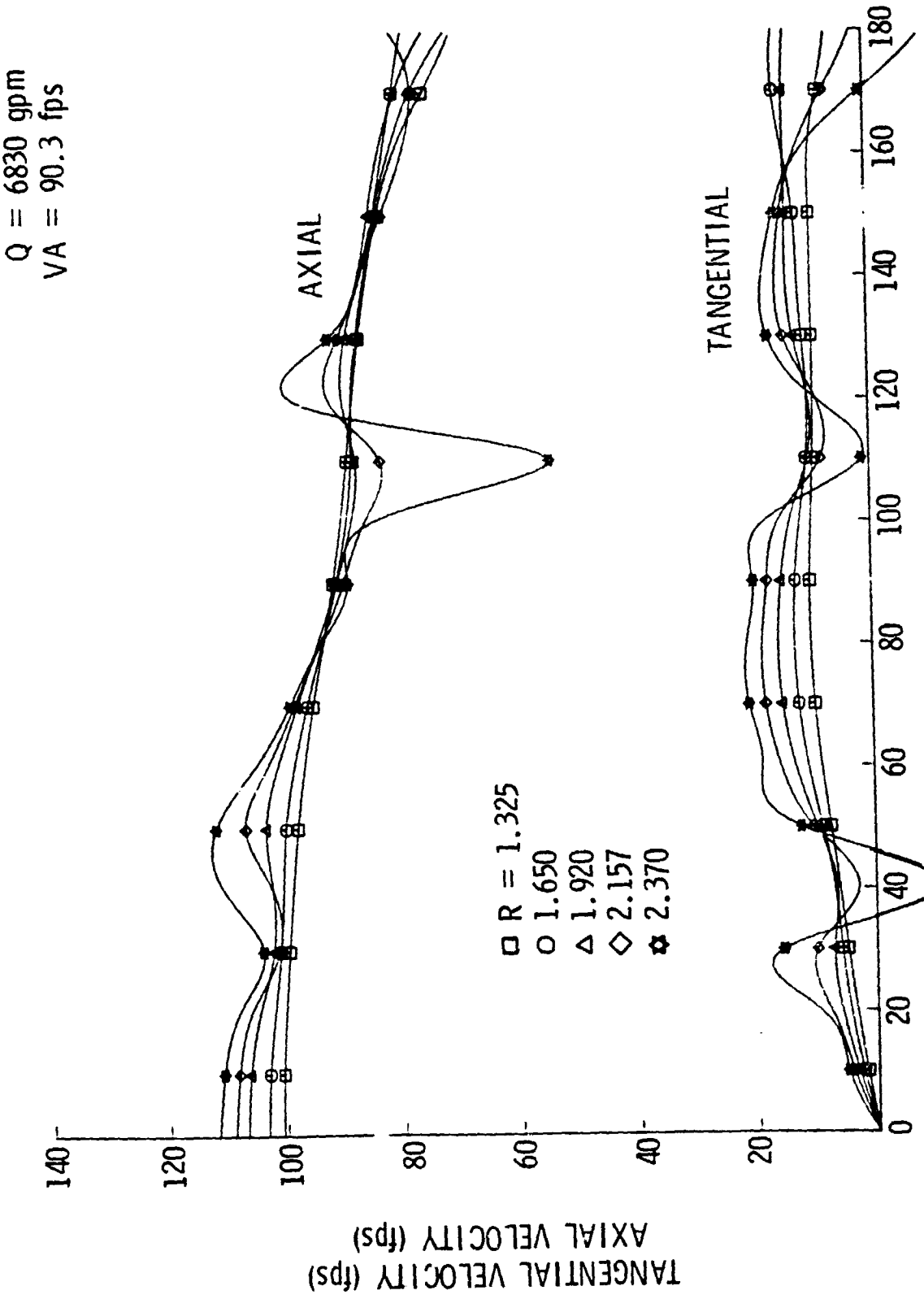

Figure 23. Inviscid Flow Solution at the Inducer Inlet

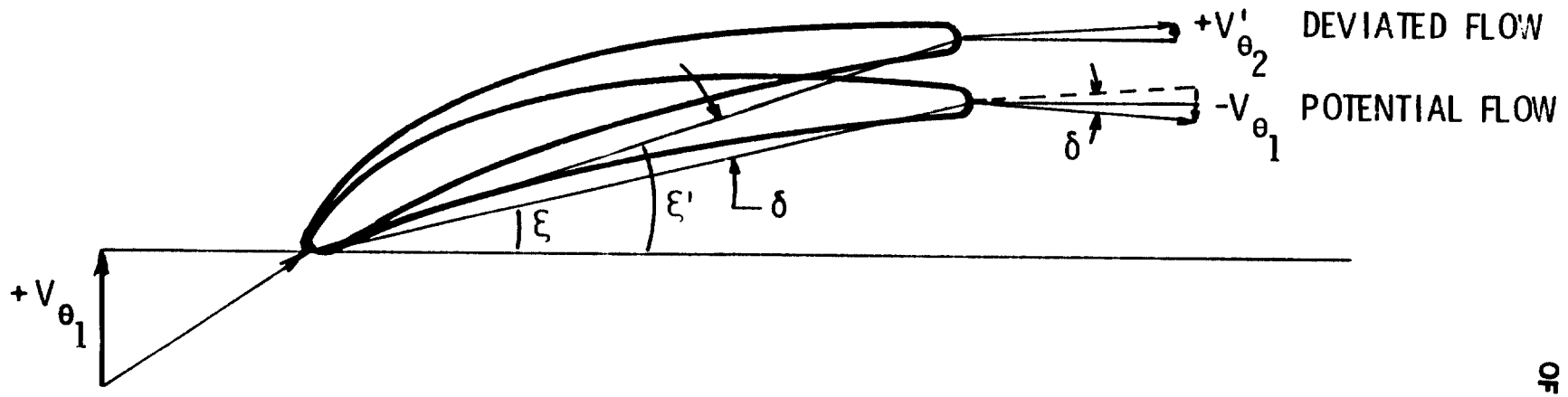

Figure 24. Deviated Vane Geometry

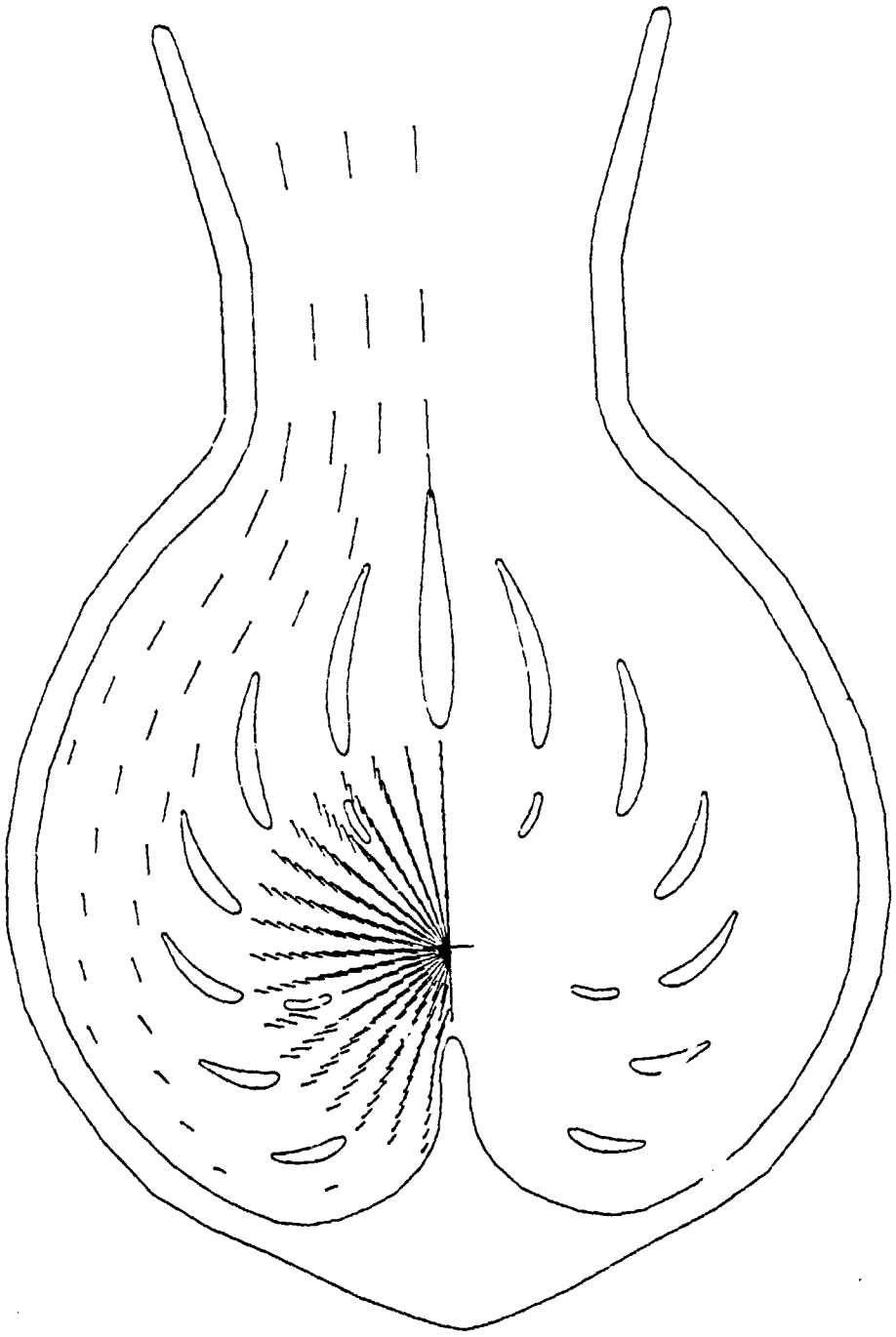

SCALE: 1" = 3.33"

Figure 25. Deviated Flow Solution for Casing With Guide Vanes

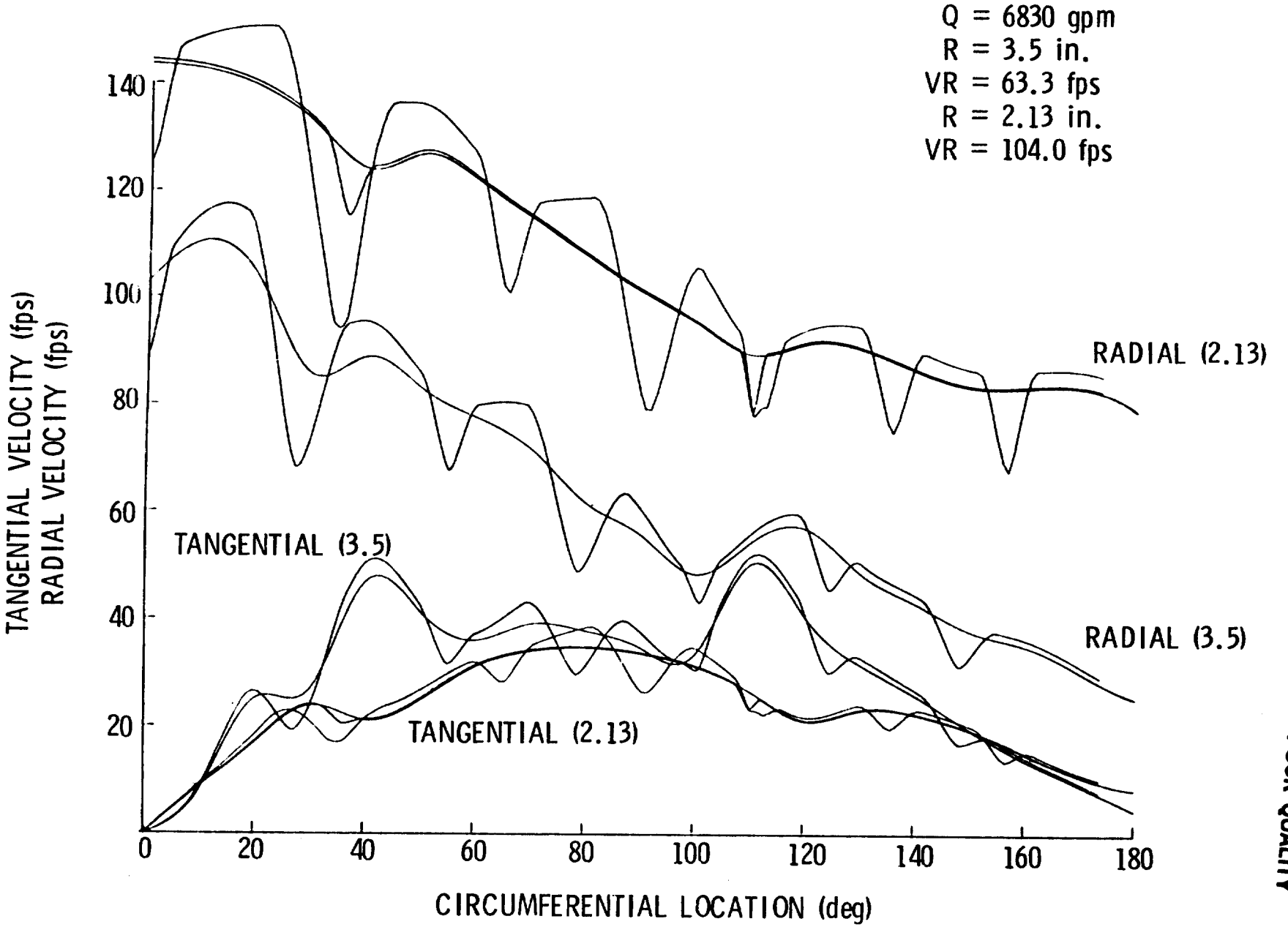

Figure 26. Wake Flow Solution at R = 2.13 inches

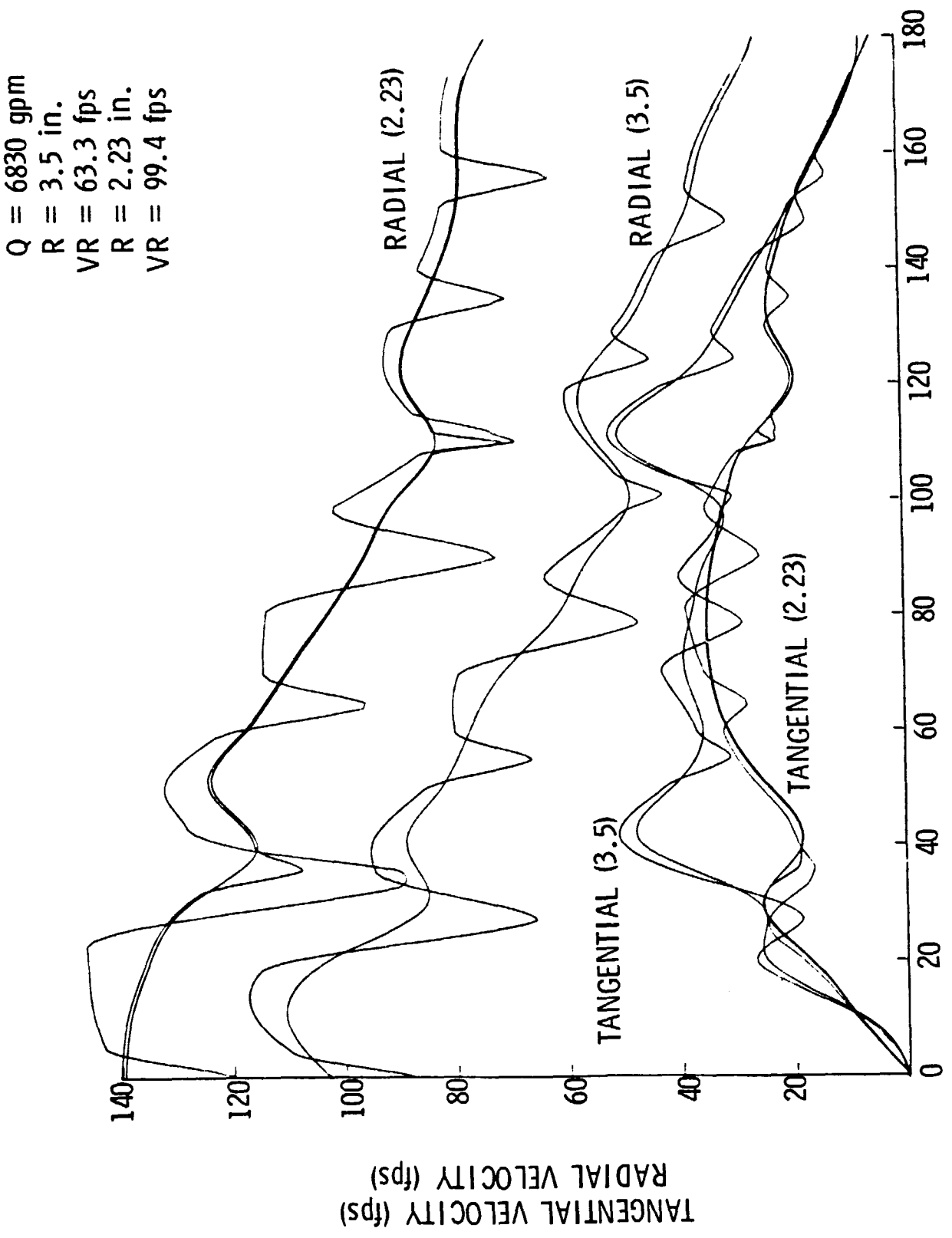

Figure 27. Wake Flow Solution at R = 2.23 Inches

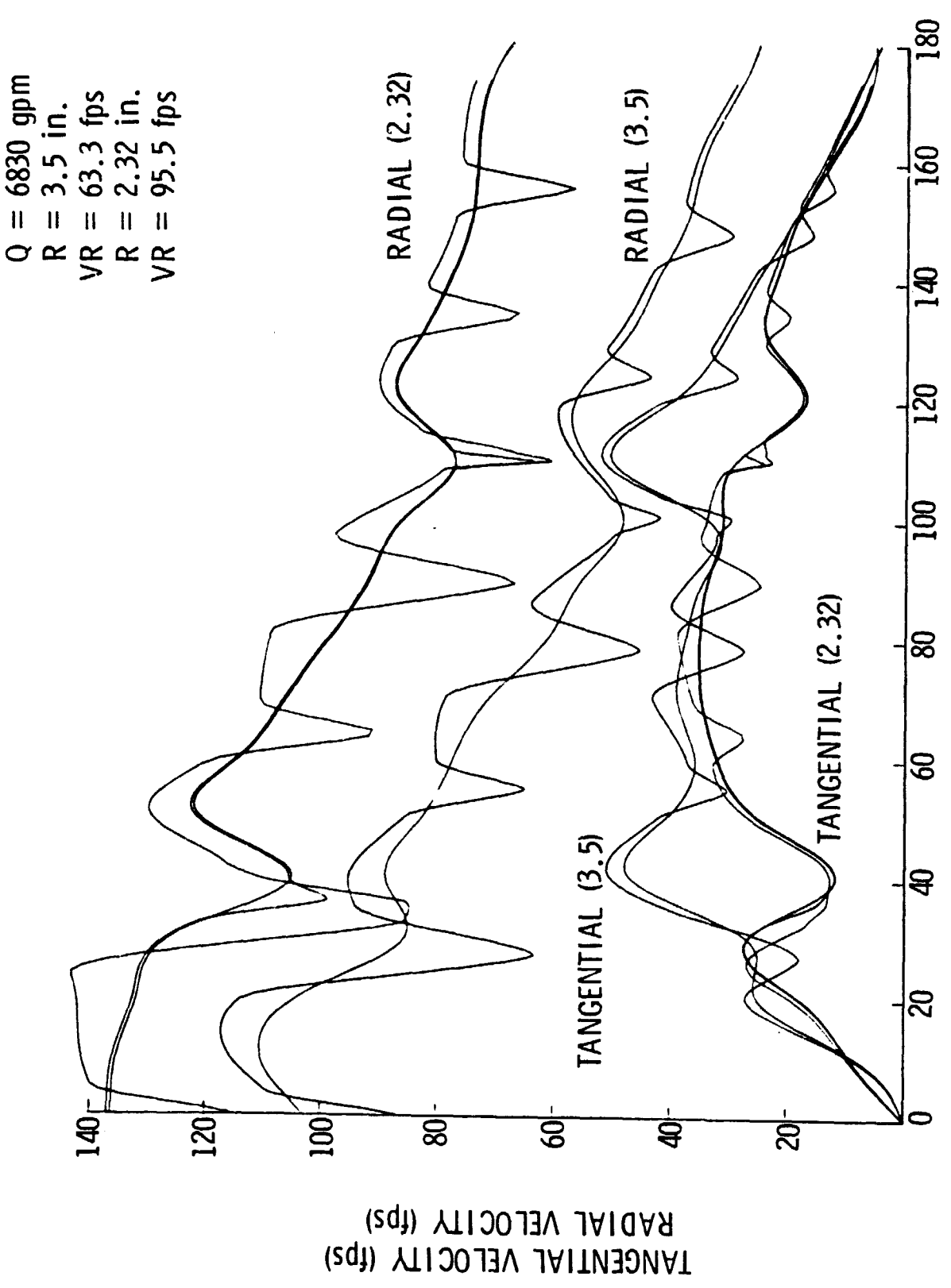

Figure 28. Wake Flow Solution at R = 2.32 Inches

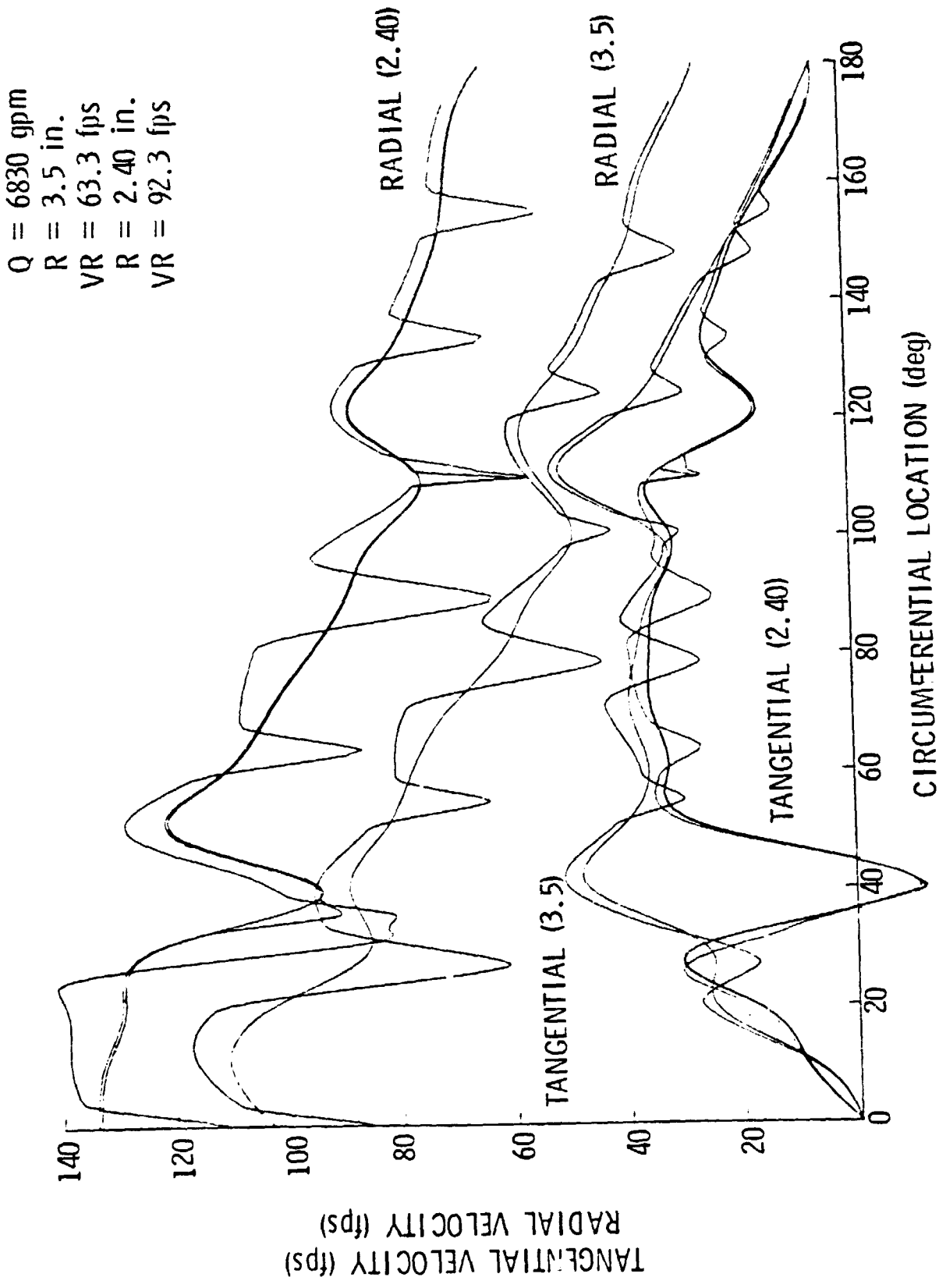

Figure 29. Wake Flow Solution at R = 2.40 Inches

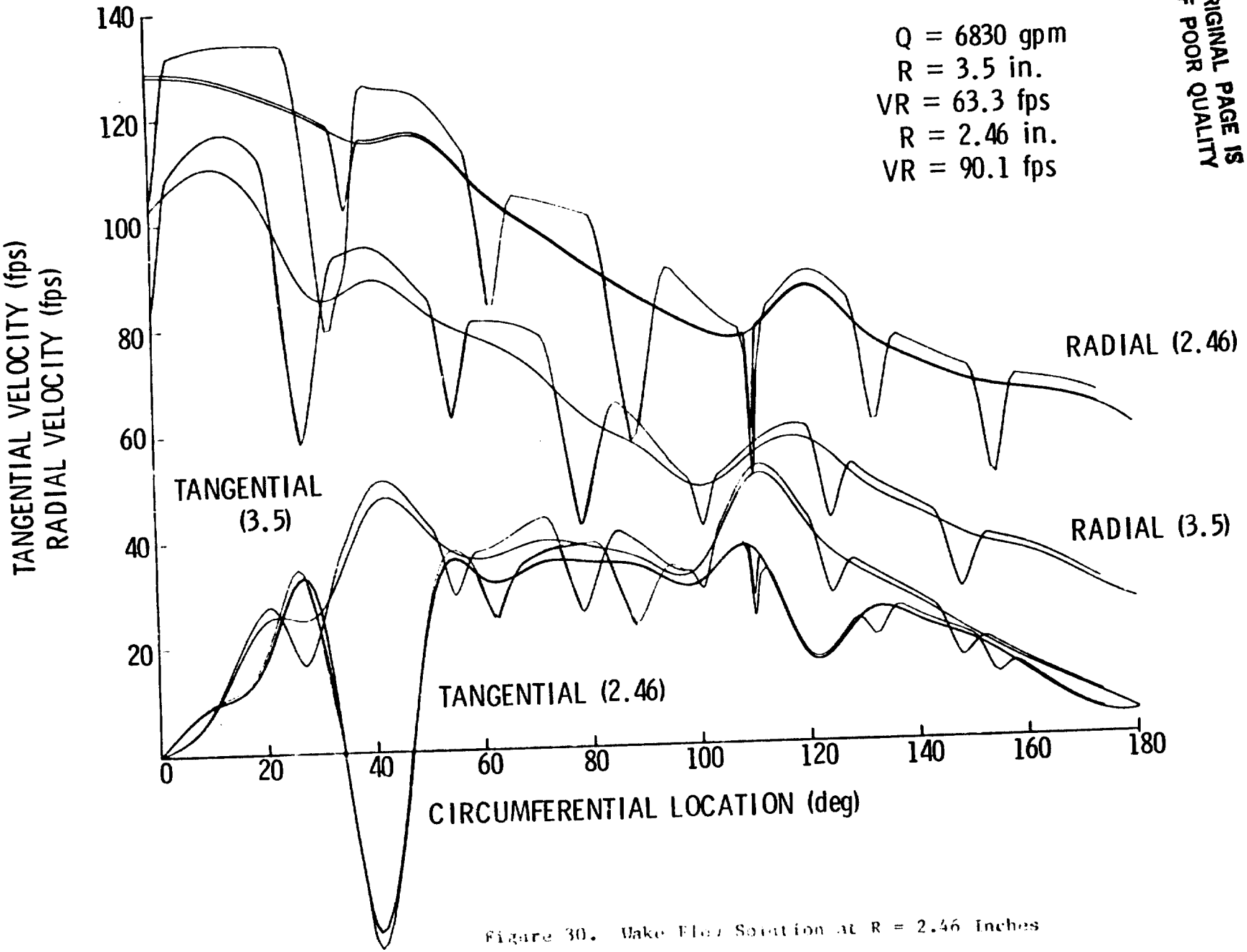

Figure 30. Wake Flow Solution at R = 2.46 Inches

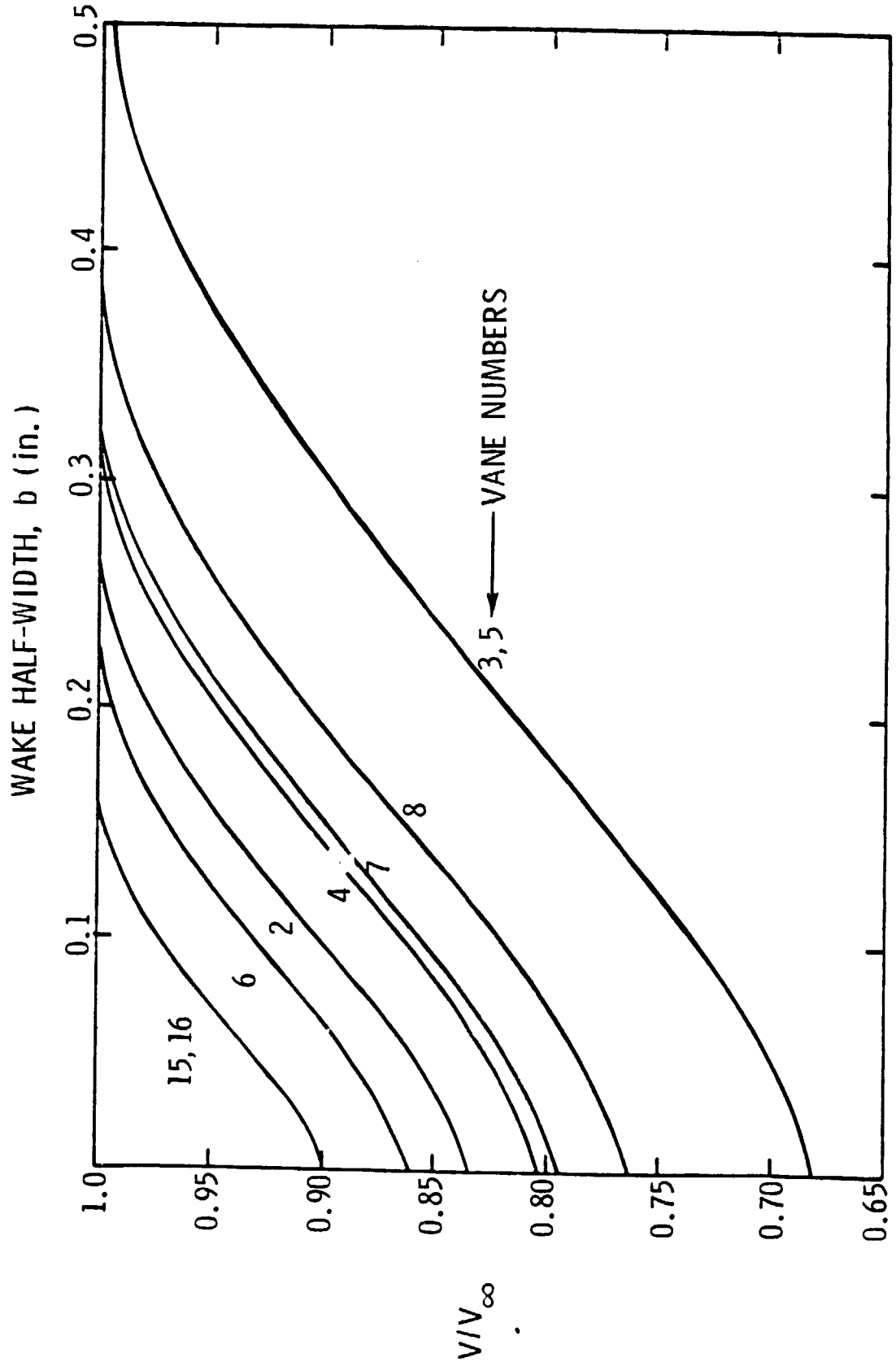

Figure 31. Calculated Wake Half-Widths for Cascade Vanes

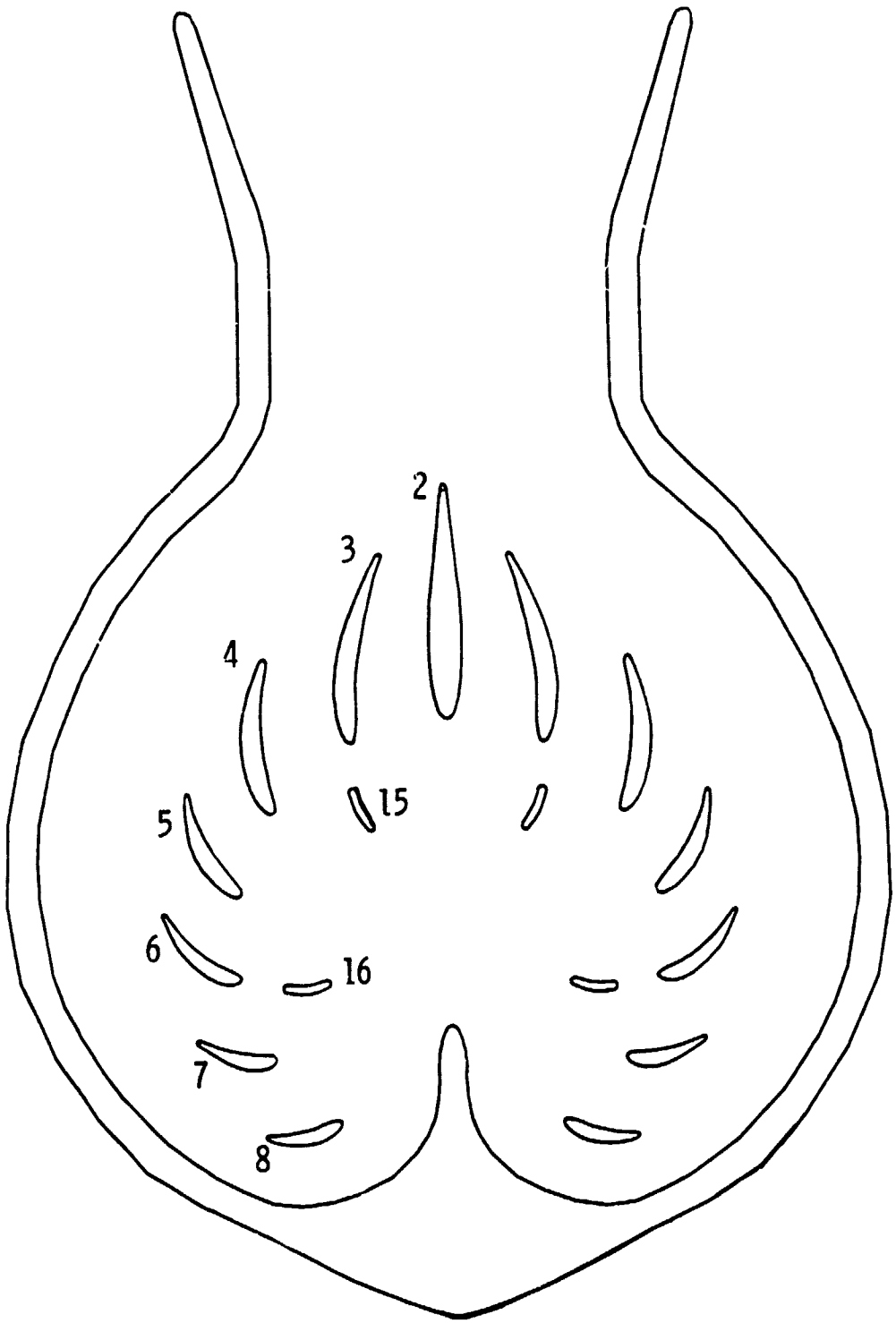

Figure 32. Schematic Showing Vane Numbers

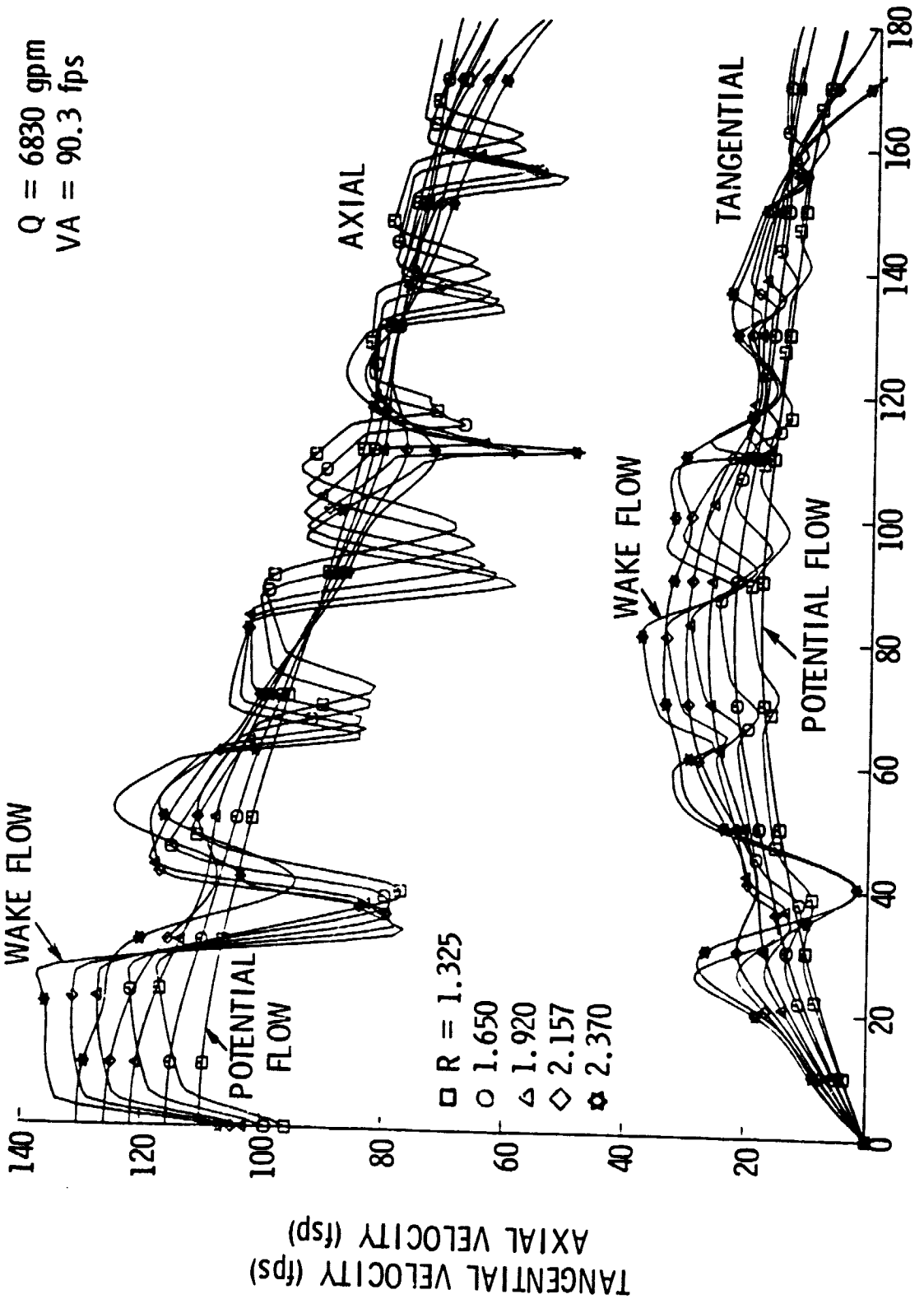

Figure 33. Flow Solution at Inducer Inlet

ORIGINAL PAGE IS
OF POOR QUALITY

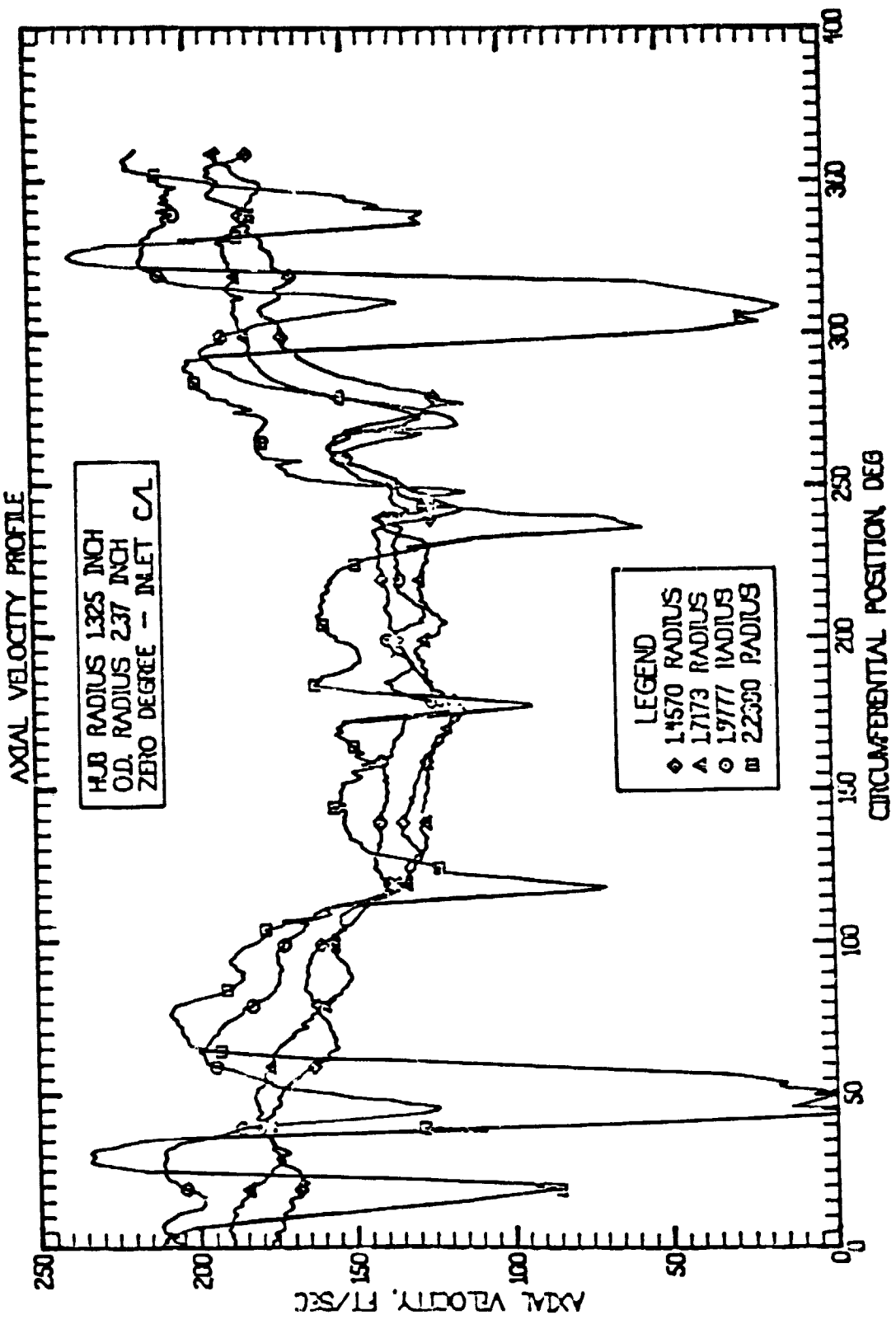

Figure 34. Measured Axial Velocity Profile (Rocketdyne)

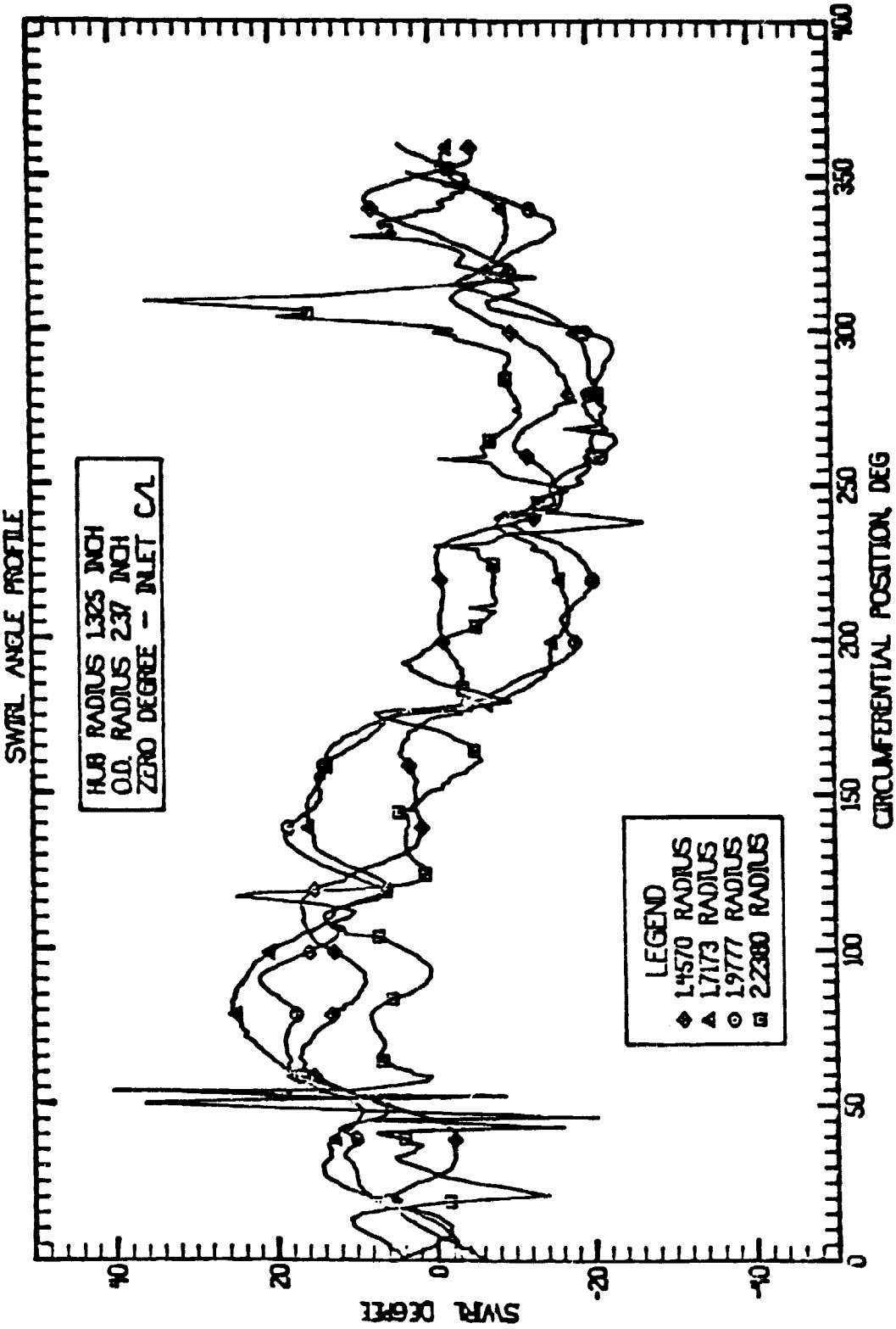

Figure 35. Measured Swirl Angle Profile (Rotor-stator)

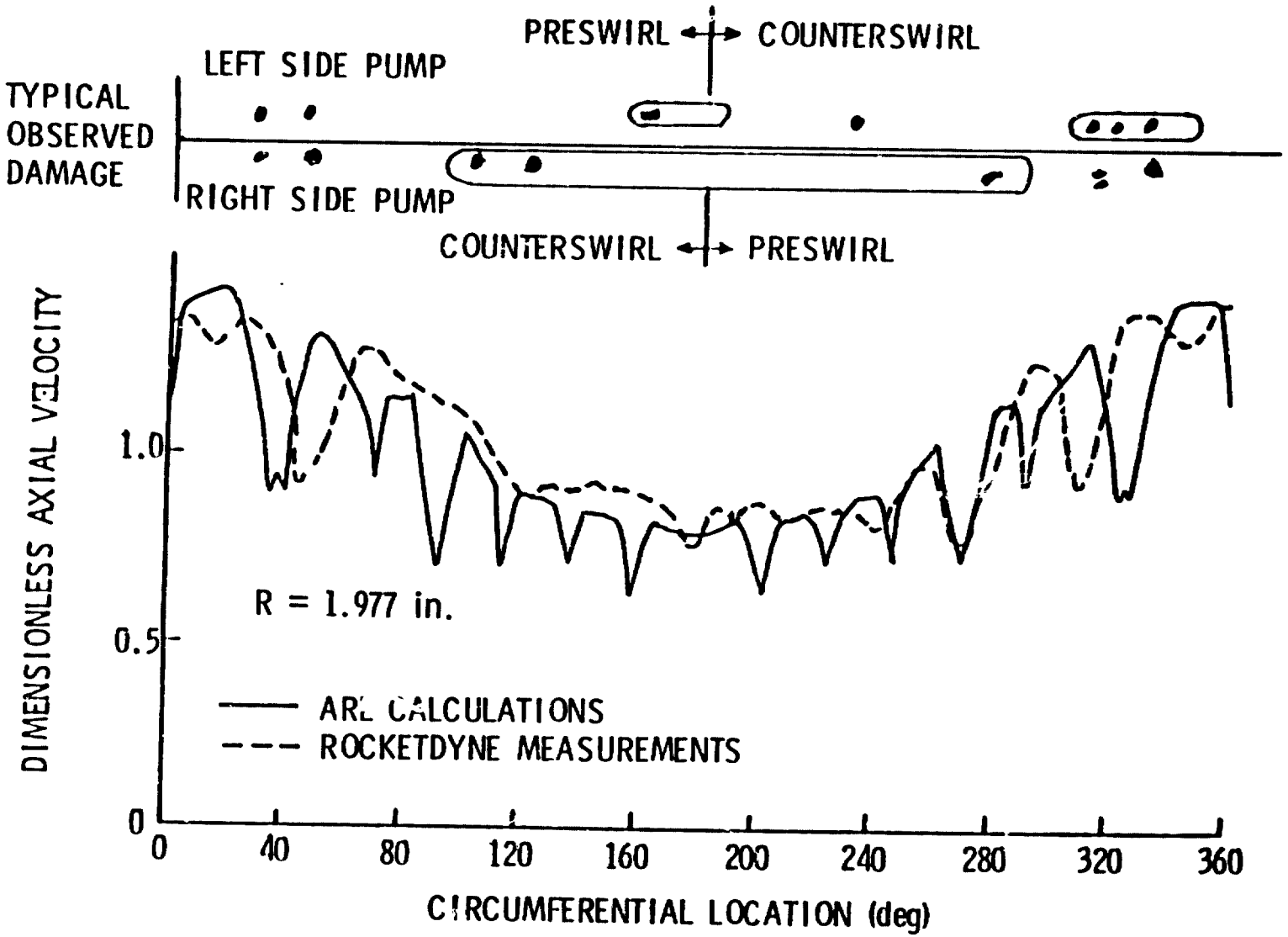

Figure 36. Comparison of Measured and Calculated Axial Velocity Profile at R = 1.977 Inches at the Inducer Inlet

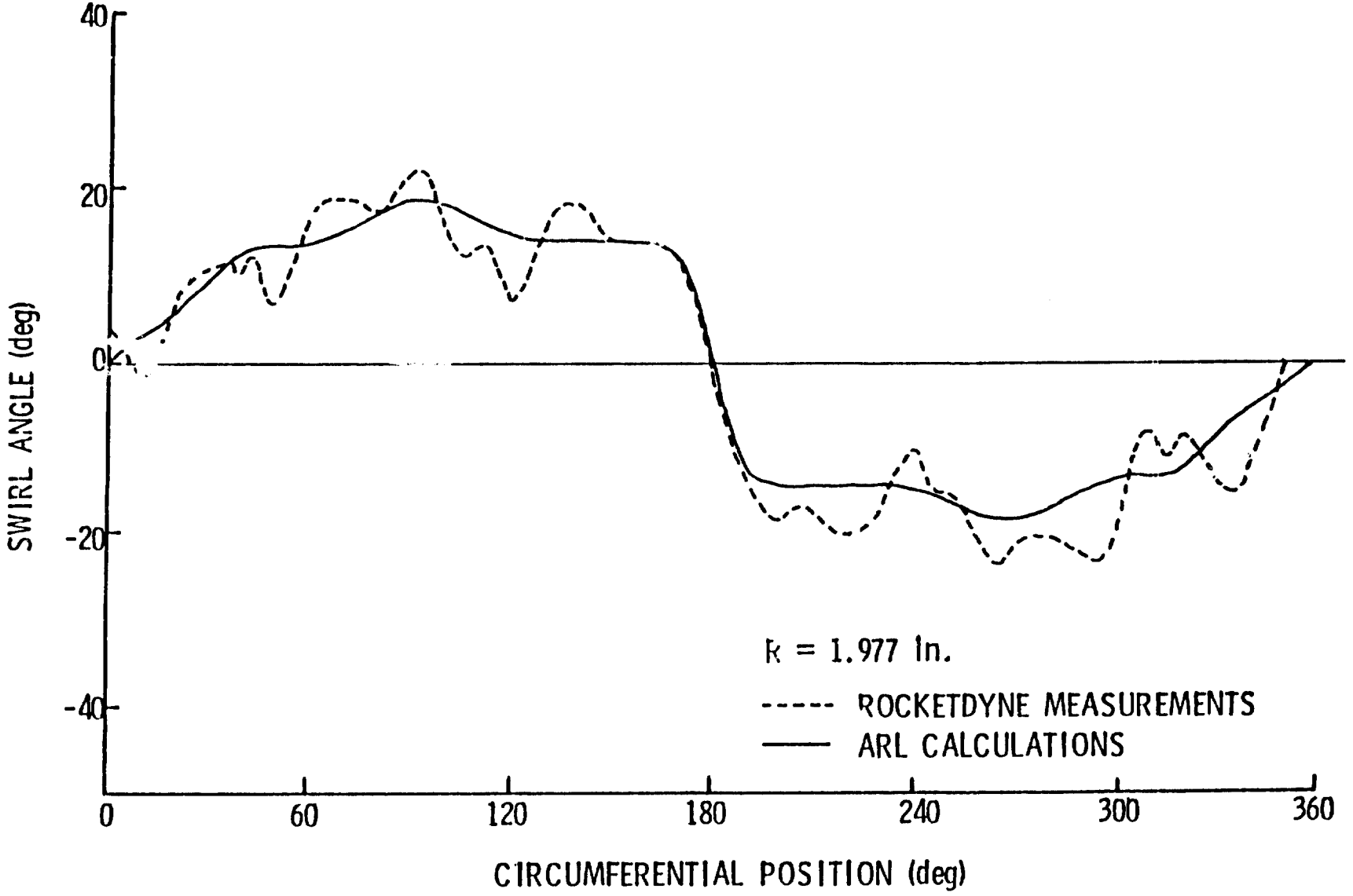

Figure 37. Comparison of Measured and Calculated Swirl Angle Data at R = 1.977 Inches at the Inducer Inlet

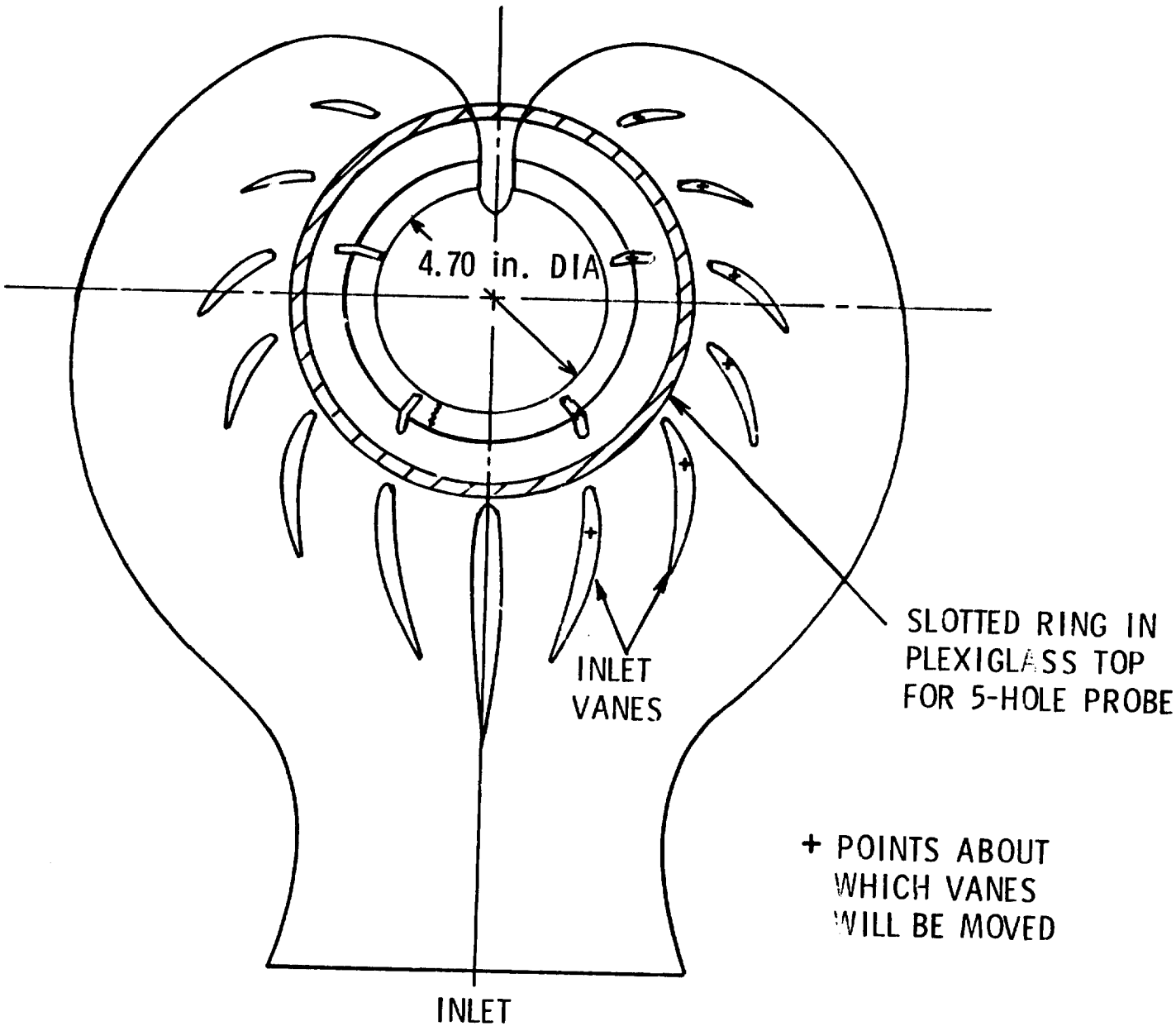

Figure 38. Schematic of the Top View of the 2-D Cascade Model

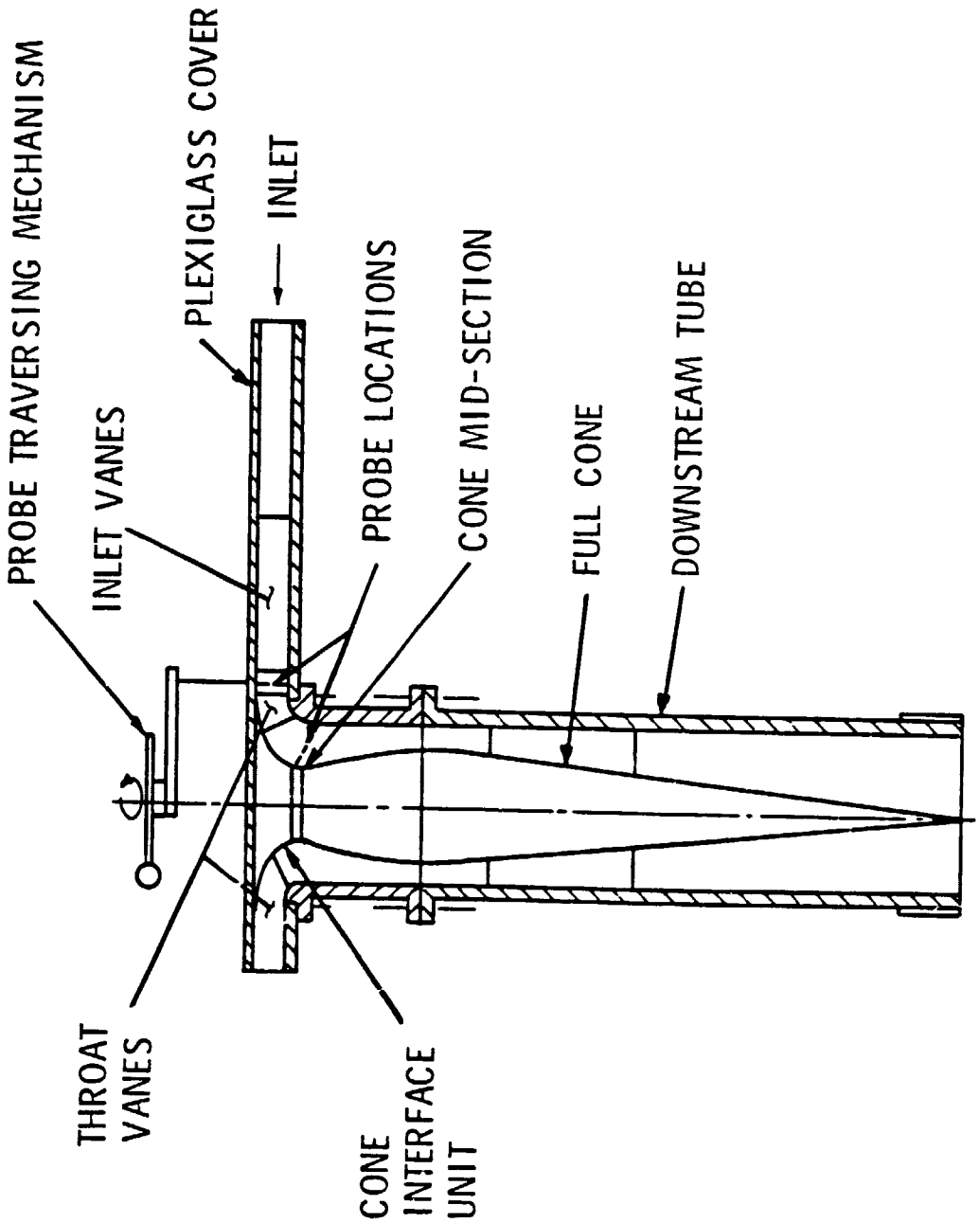

Figure 39. Schematic of the Side View of the 2-D Cooling Model

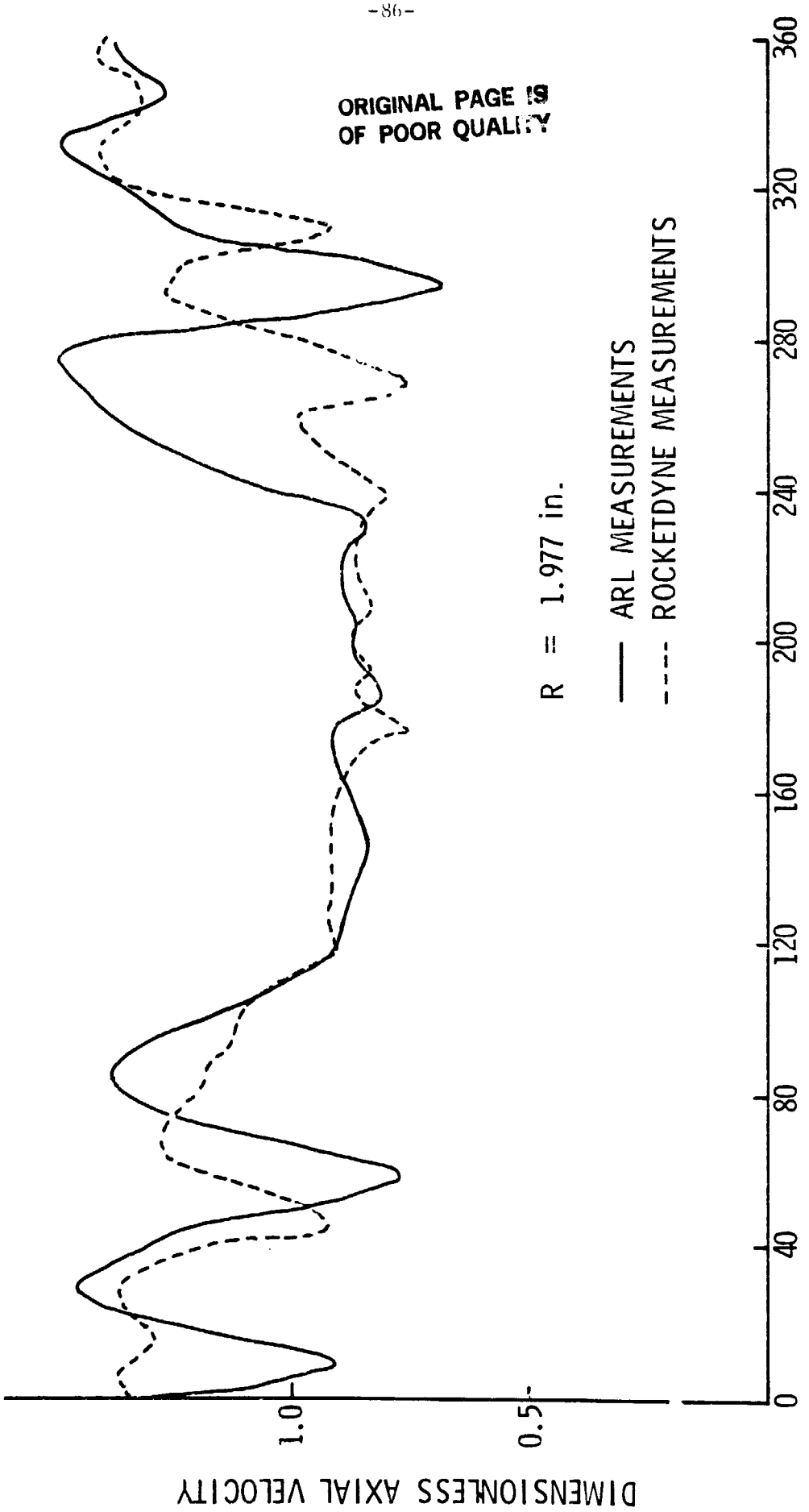

Figure 40. Comparison of 2-D Model Data With Rocketdyne Data

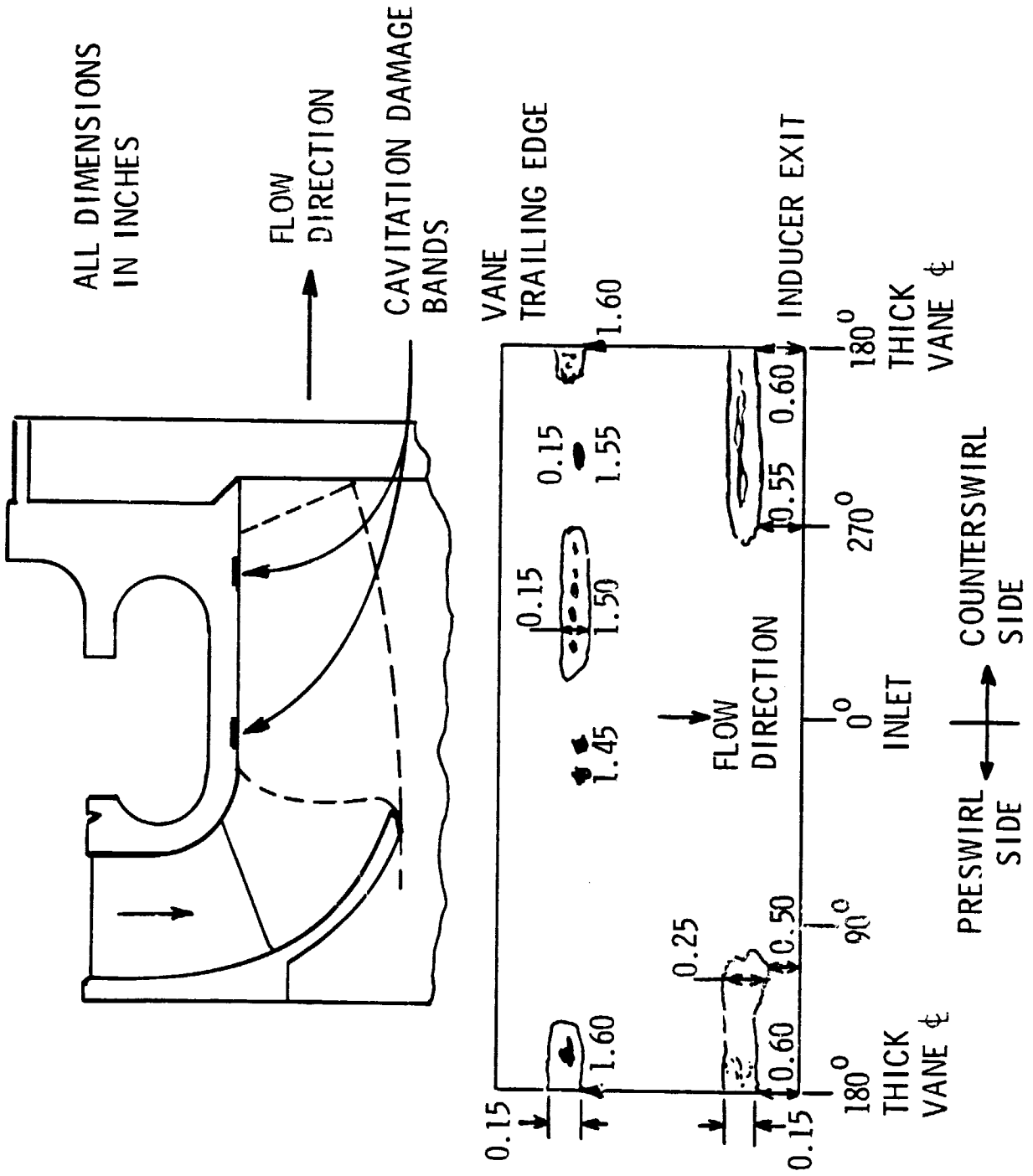

Figure 41. HPOTP L.H. Vane Cavitation Damage on Casting (Roughdown)

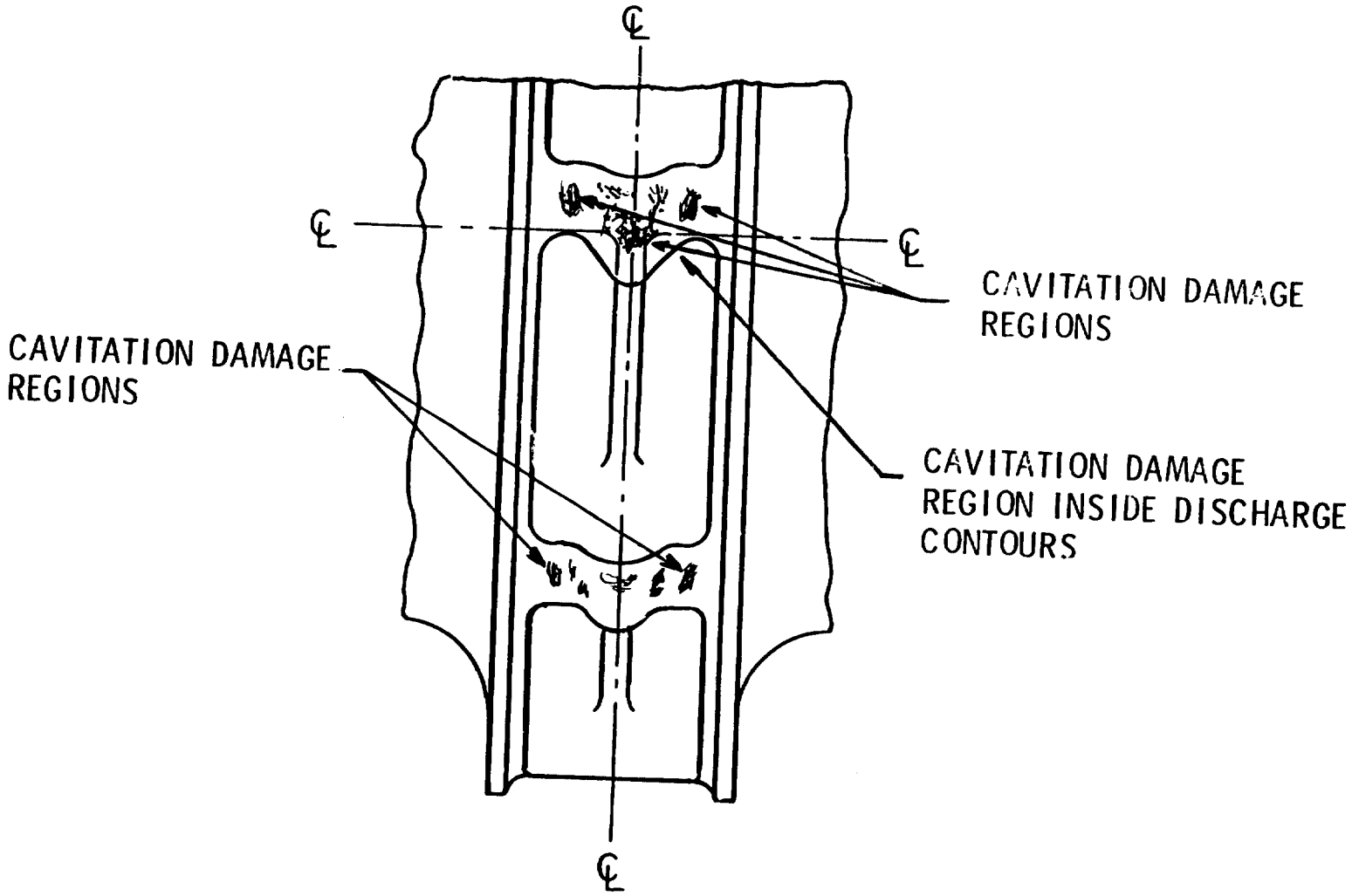

Figure 42. HPOTP Impeller Cavitation Damage Regions at the Trailing Edge of the Blades (Rocketdyne)

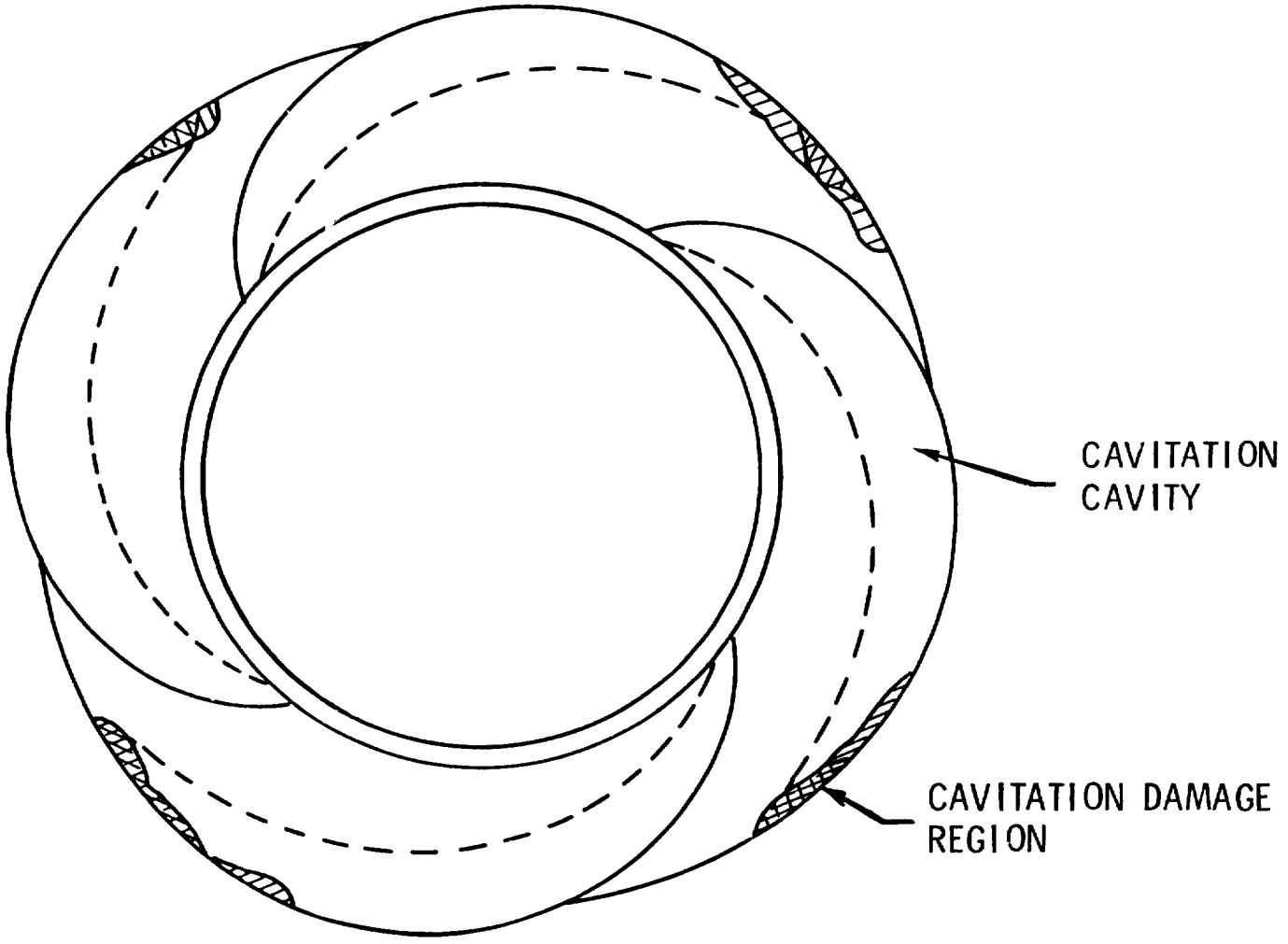

Figure 43. Location of Cavitation Damage on the Inducer Together With the Calculated Cavitation Pattern for Uniform Flow and No Preswirl

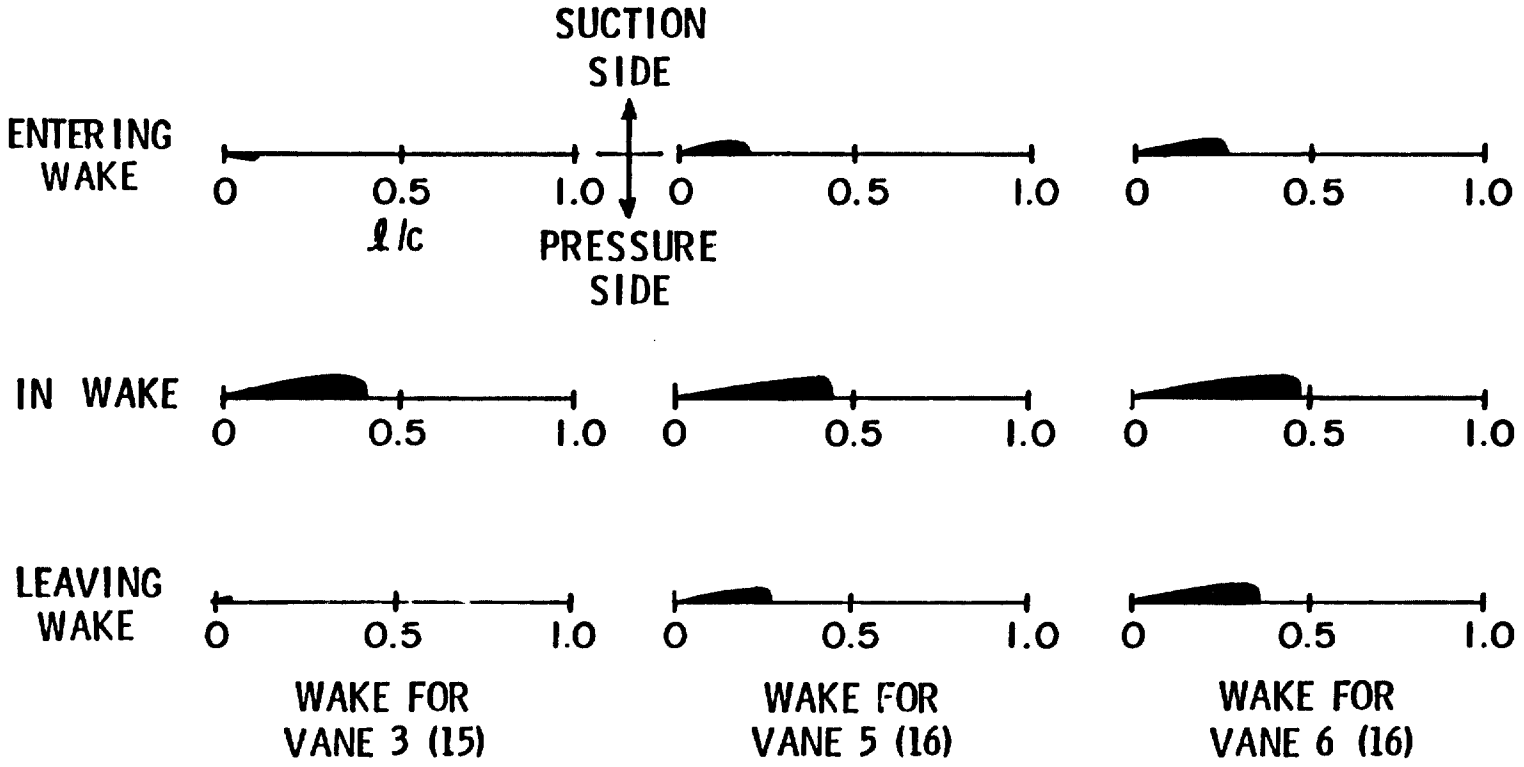

Figure 44. Calculated Cavity Lengths for the Existing Design With Wakes (Preswirl Side)

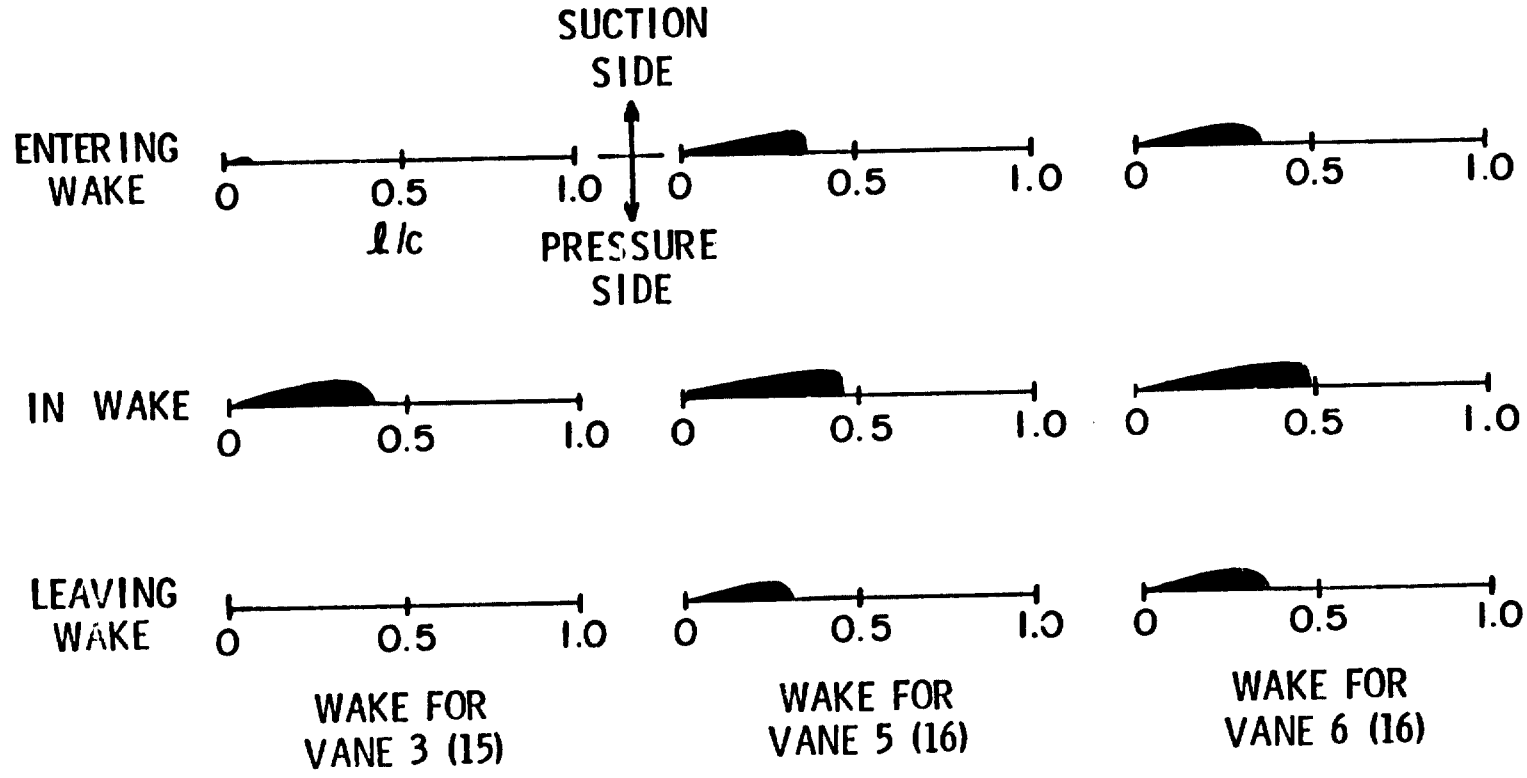

Figure 45. Calculated Cavity Lengths for the Existing Design Wake Wakes (Counterswirl Side)

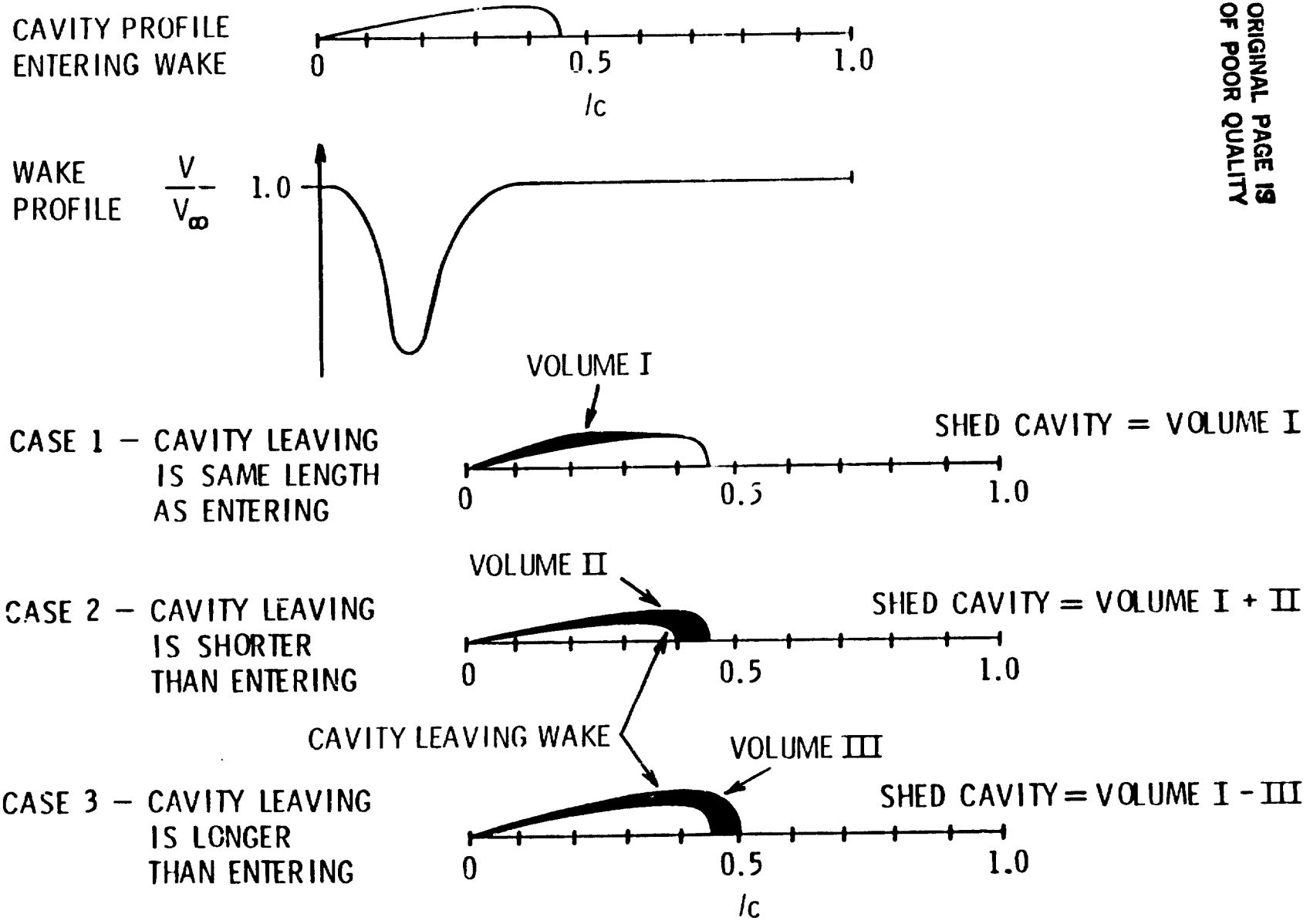

Figure 46. Schematic of the Method for Calculation of a Shed Cavity Through a Wake

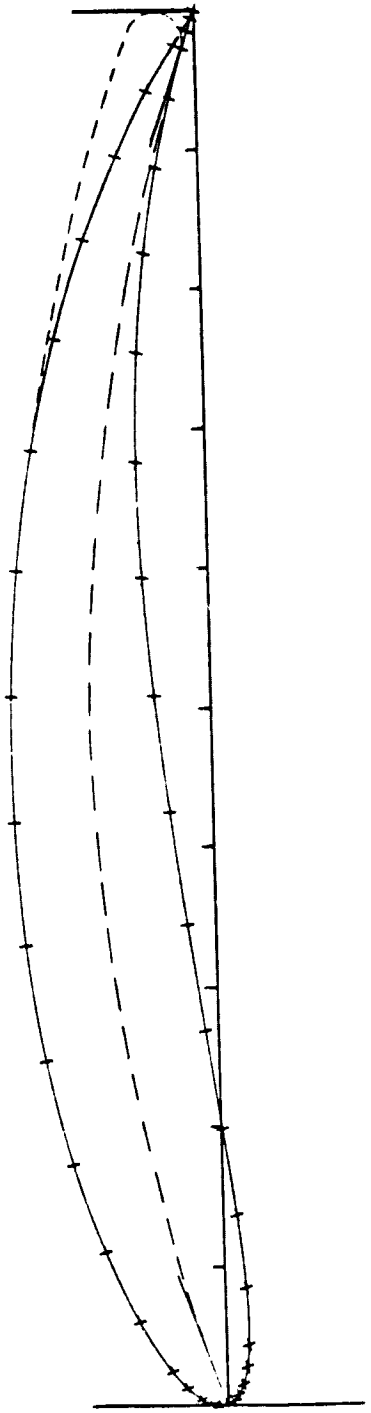

Figure 47. Typical Ramp Response for Project Mode Values

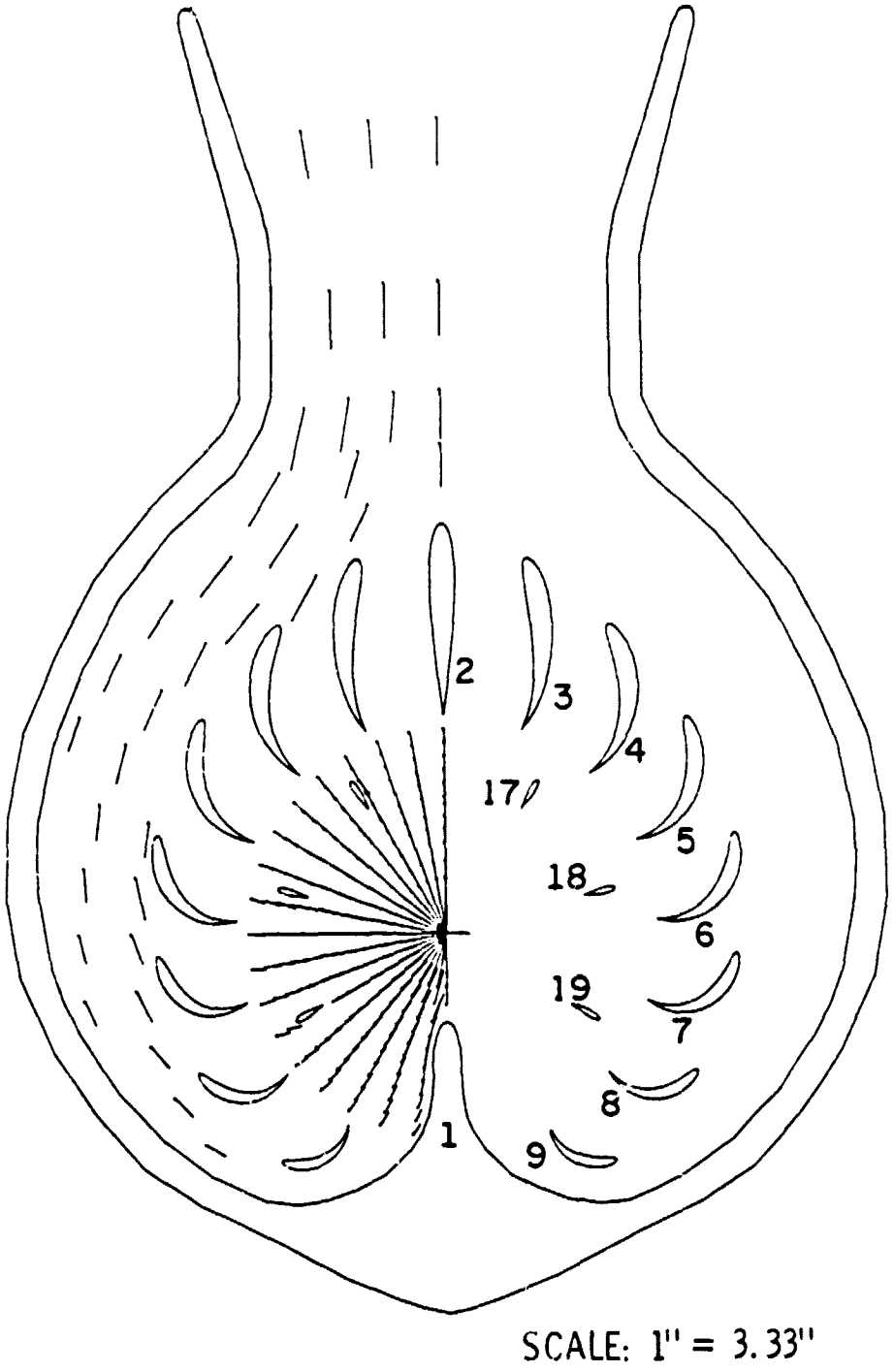

Figure 48. Potential Flow Solution for the Redesigned Vanes

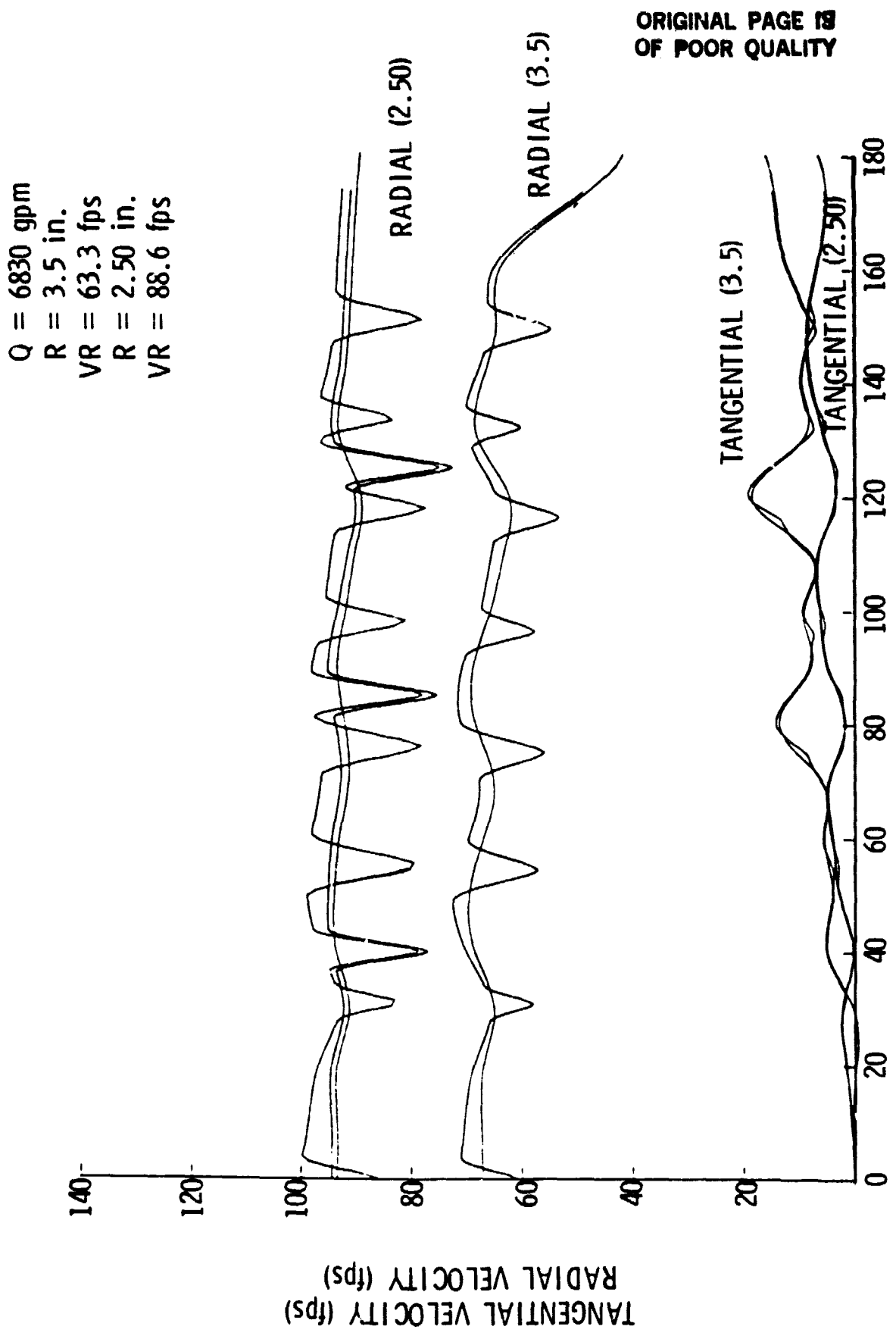

Figure 49. Wake Flow Solution for the Impeller at R = 3.5 Inches and R = 2.5 Inches

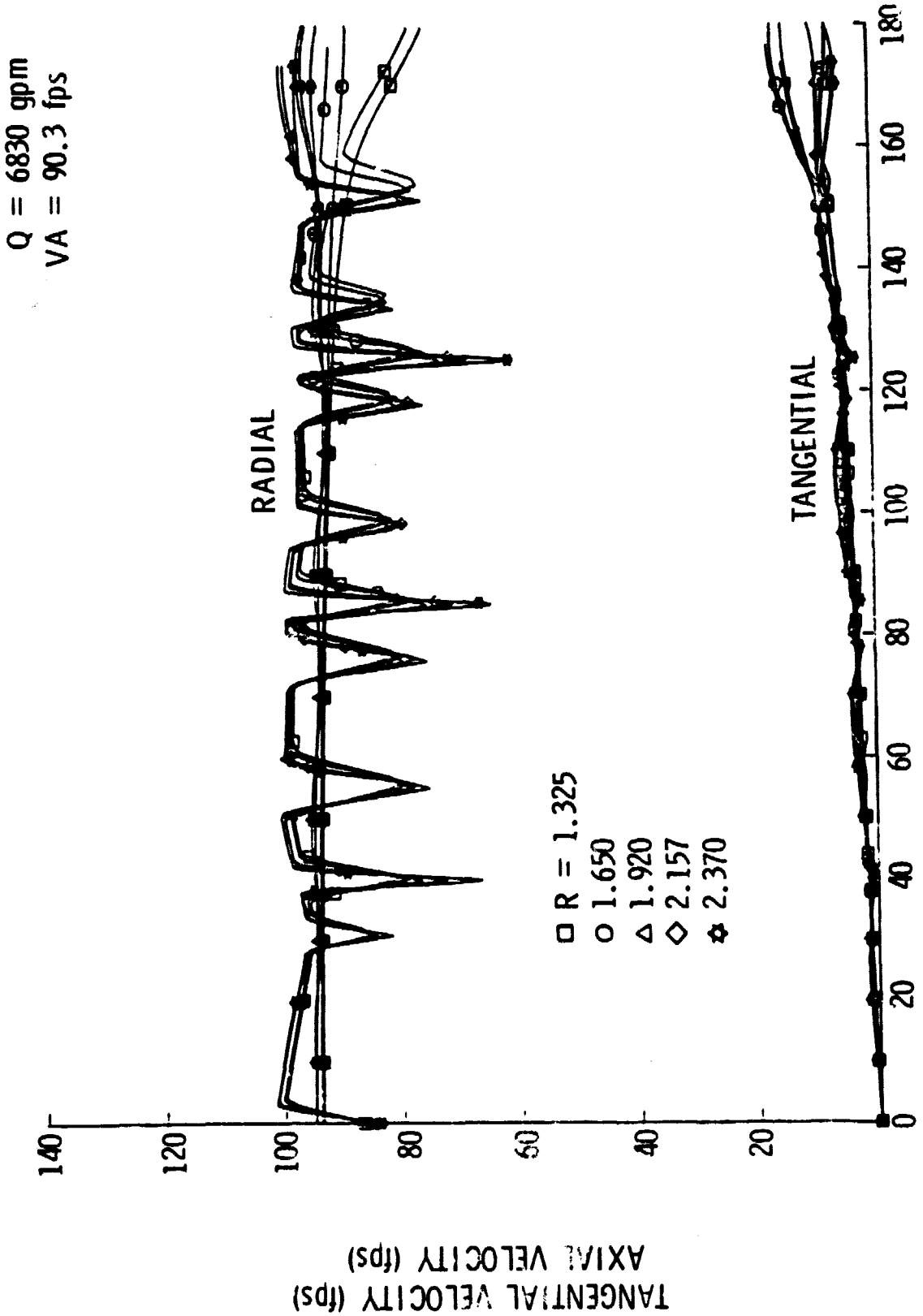

Figure 50. Wake Flow Solution at the Impeller Inlet for the Redesign

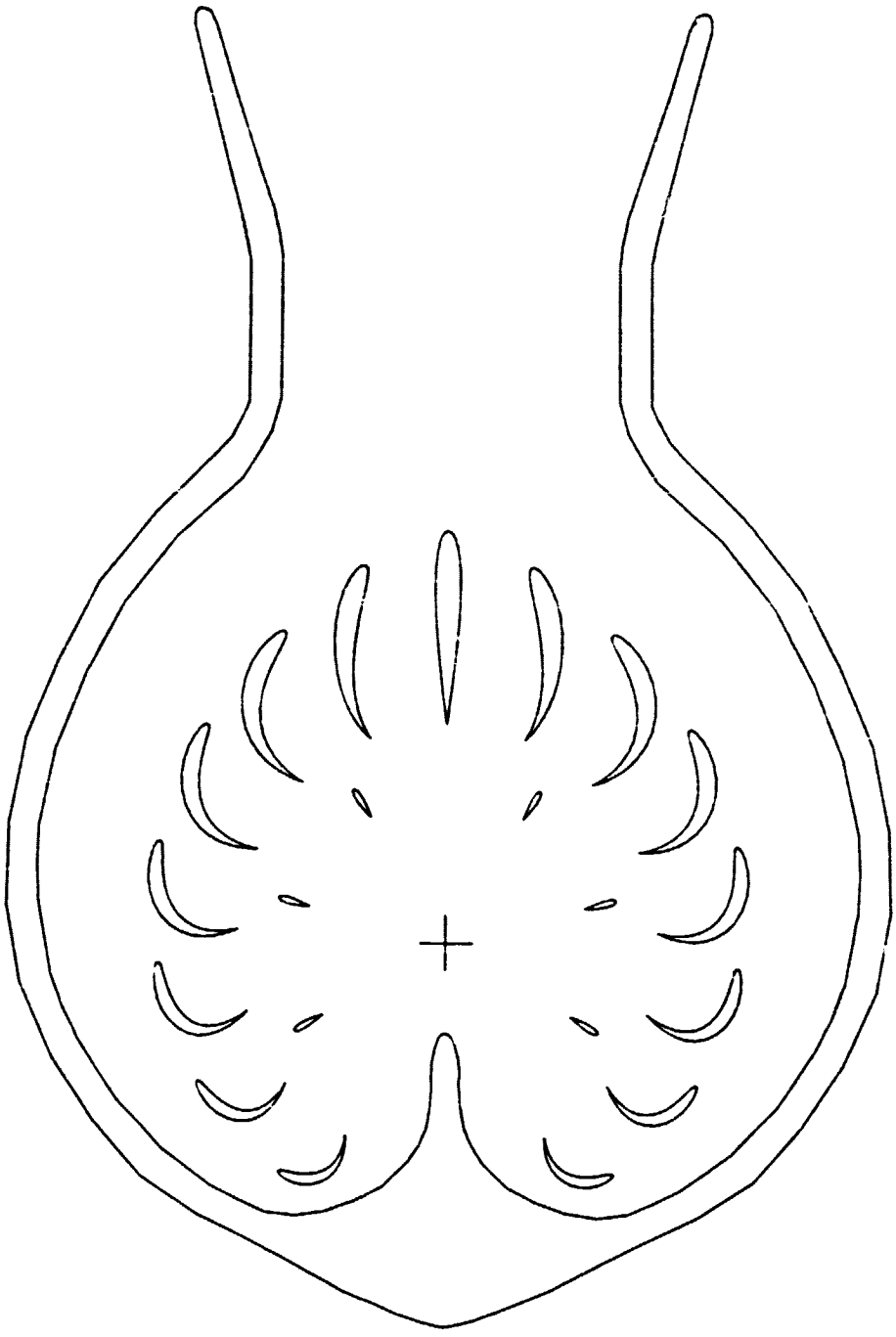

SCALE: 1" = 3.33"

Figure 51. Vane Geometry for the Redesign with Vane Offsets Included

C-2

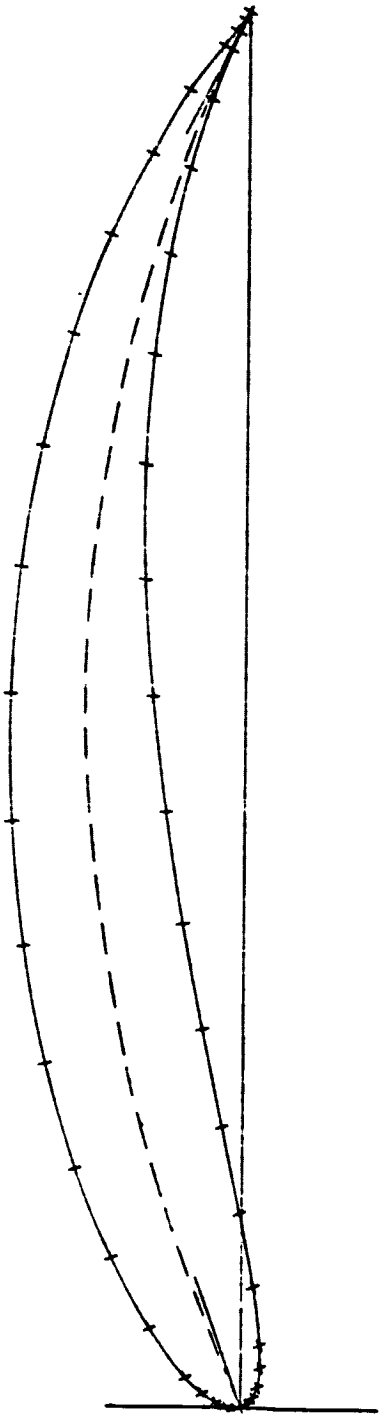

Figure 52. Typical Vane Geometry for the Recession With Offset Included

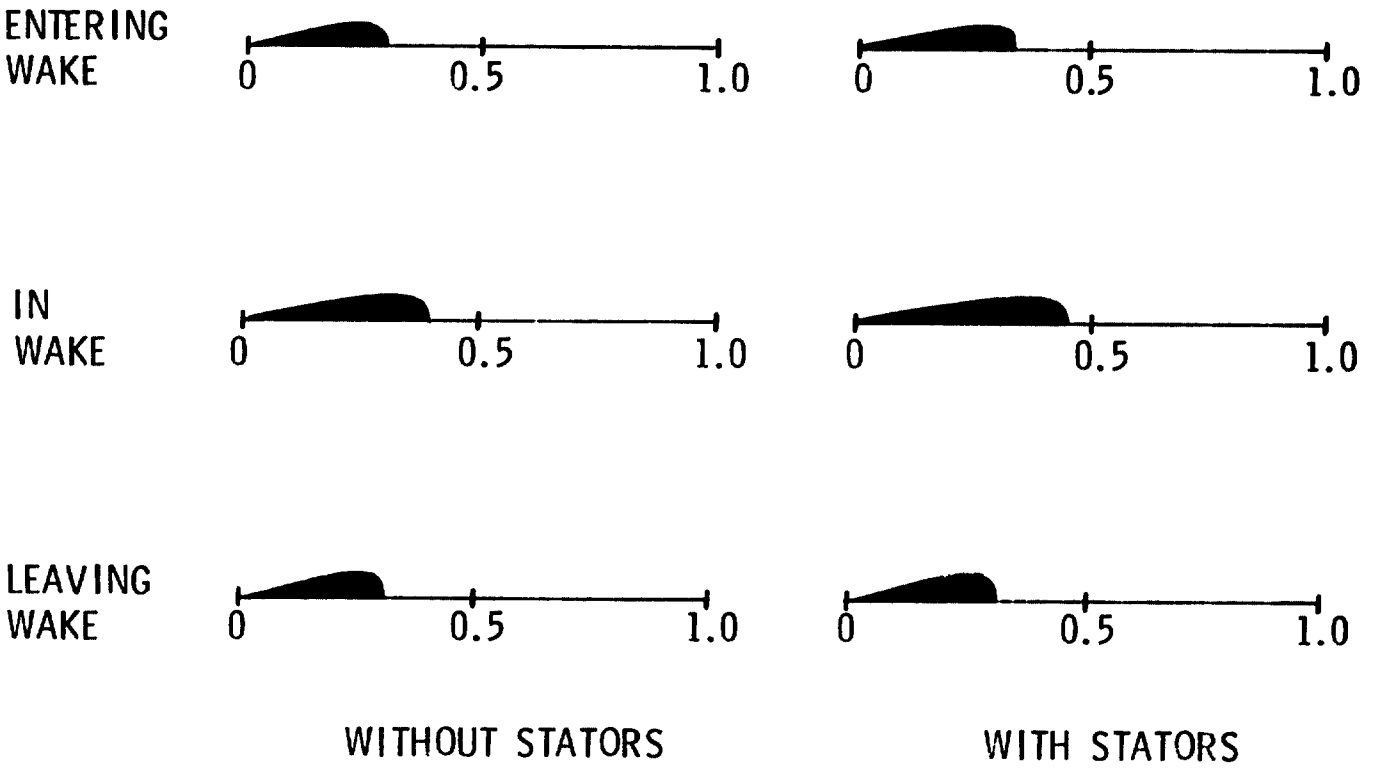

Figure 53. Calculated Cavity Lengths for the Rotation With Wake

APPENDIX A

Steady-State Cavity Calculation Procedure

A method developed by Stripling and Acosta [14] was used to calculate the size and shape of the cavity on inducer blades. The flow was modeled for a helical inducer by a free-streamline calculation of the flow through a semi-infinite cascade. The flow was assumed to be two-dimensional, irrotational and inviscid. A wake or dissipation model simulates the blockage that occurs due to the mixing at the cavity trailing edge which is the condition emphasized when the cavity is less than the chord length. The flow is then confined within the cascade blade passage and the chord assumed to be infinitely long.

The free-streamline flow is mapped in the hodograph plane to simplify the cavity calculations. A schematic of the flow in the physical and hodograph planes is presented in Figure A1. The hodograph variable is defined as:

$$\zeta = \frac{dF}{dz} = u - iv \tag{A.1}$$

where u and v are the x and y velocity components in the physical plane and $z = x + iy$.

$$F = \overline{\phi} + i\,\overline{\psi} \tag{A.2}$$

is the complex potential of the flow with $\overline{\phi}$ being the velocity potential and $\overline{\psi}$ the stream function. The physical coordinates of the flow are found by determining the functional relationship between F and ζ and integrating A.1:

$$z = \int \frac{dF}{\zeta} + \text{const} \quad . \tag{A.3}$$

To solve A.3 the following boundary conditions in the hodograph plane must hold:

(1) The real axis and $|\zeta| = W_c$ are streamlines

(2) $\zeta = 0$ is a stagnation point, therefore

$$\frac{dF}{d\zeta}(\zeta = 0) = 0$$

(3) Streamlines in the hodograph plane, near the origin corresponding to the flow at infinity, are uniform and inclined at an angle α to the axis.

From Bernoulli's equation the velocity along the cavity wall W_c is:

$$W_c = W_\infty \sqrt{1 + \sigma} \tag{A.4}$$

where ω_∞ is the upstream velocity and σ is the cavitation number given as:

$$\sigma = \frac{P_\infty - P_c}{\frac{1}{2} \rho W_\infty^2} \tag{A.5}$$

The coordinates of the flow are then found from A.3. The coordinates of the cavity length and height are found from:

$$z = x + iy$$

$$= c + ih$$

$$= z(\zeta = W_c) - z(\zeta = -W_c) \quad .$$

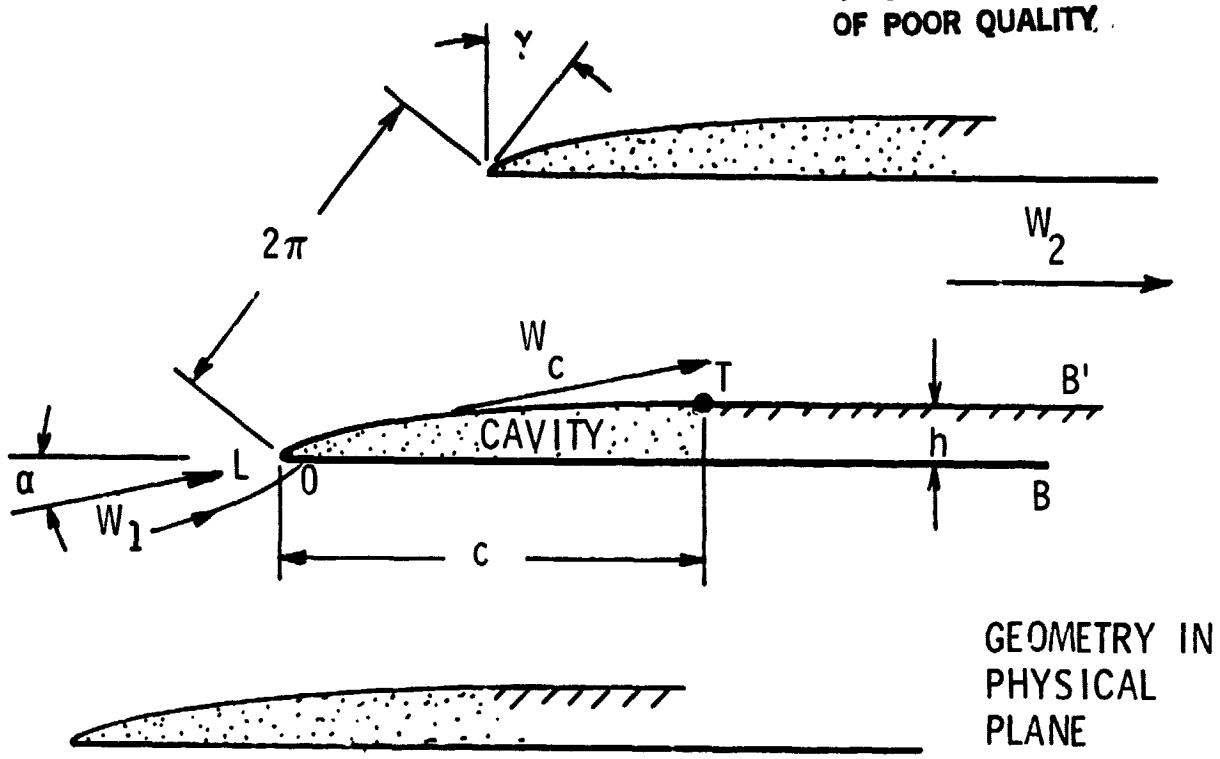

GEOMETRY IN PHYSICAL PLANE

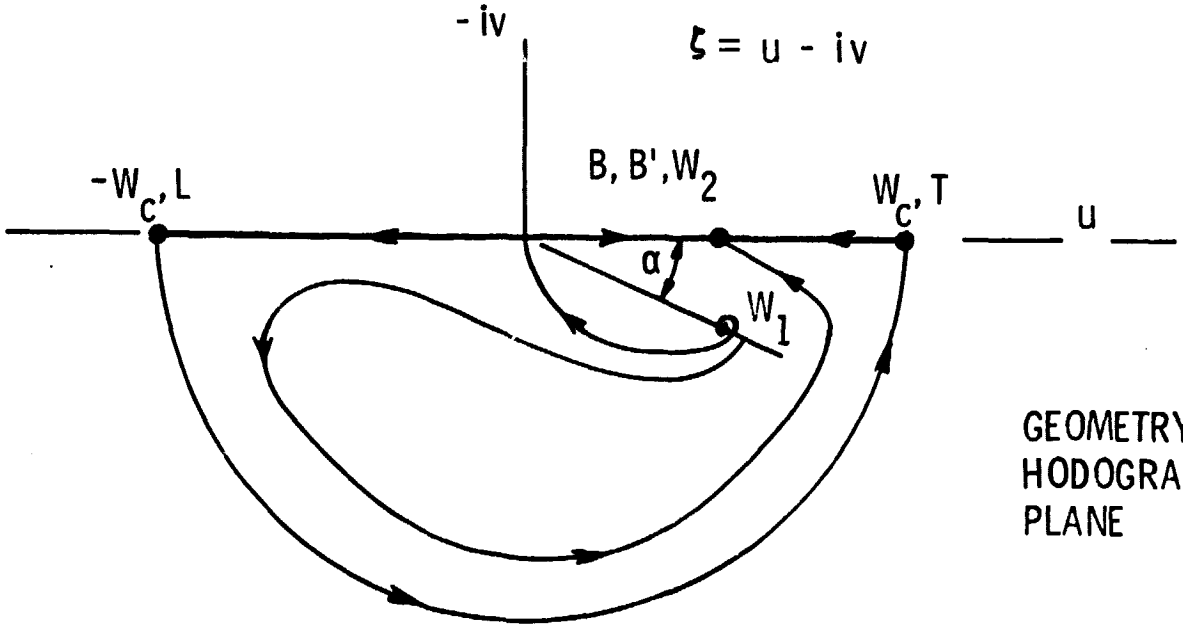

GEOMETRY IN HODOGRAPH PLANE

Figure A1

APPENDIX B

Unsteady Cavitation and Erosion

The destructive action caused by cavitation has been a practical problem for many years. Erosion of ship propellers and hydraulic turbine blades can cause a loss in performance leading to eventual costly maintenance or replacement of the damaged parts. The damage is caused by the collapse of the vaporous cavities as they move into a high pressure region. Upon collapse, enormous pressures are generated. If the cavity collapse occurs near a boundary, damage can occur.

Accurate prediction of cavitaiton damage is very difficult. After nearly 100 years of research in cavitation, the problem of calculating the amount of erosion for a given prototype is as yet unsolved. The lack of success is because cavitation damage involves both the fluid and solid mechanics and thus is inherently difficult.

The attack caused by the collapse of one cavitation bubble occurs over a very small area (or the order of hundredths of a square millimeter) and in a very short time interval (measured in microseconds). Both the hydrodynamic aspects of the cavity flow and the material response to the impact loading caused by the cavity collapse must be considered. The problem is further complicated by possible interactions between cavitation and corrosion.

In analyzing the inducer blade and casing damage it was assumed that a steady sheet of cavitation would exist on the blade in uniform flow. Any cavity length fluctuations arise from the blade passing through the wakes. This sheet type of cavitation is often observed near the blade tip on surface ship propellers. Most conventional surface ship propeller blades have low thickness to chord length ratios and low camber. The typical blade sections at the tip are similar to the inducer blade profile for the oxidizer pump.

It has been reported that when a surface ship propeller blade passes through the wake caused by the hull, severe noise, vibration and structural damage (blades and hull) can result. In a recent paper presented at the Joint Symposium on Design and Operation of Fluid Machinery, June 1978, Cumming, et.al. [15] measured the effect of wakes on the cavitation damage rate for some surface ship propellers. The results for two tests, one with and one without an upstream wake, are presented in Table B1. The mean velocity, test duration and cavitation number were approximately equal for both tests. Since the flows were similar except for the wake any change in damage rate should be due to the unsteady flow. The total pitting rate was approximately 2.48 times higher for the flow with the wake. The wake was approximately 60° wide. If the difference in the pitting rate were due solely to the wake then the pitting rate in the wake is nearly 8.9 times higher. While the pitting rate is one measure of the damage the size of the individual pits should also be considered.

For an approximation the pits are assumed to be conical sections with a constant diameter to depth ratio. The damage data is reduced to a total volume of erosion per unit area per hour. The volume erosion rate is 140 times higher for the wake region than in uniform flow. Thus, decreasing the velocity deficit and wake width can greatly reduce the damage rate. The assumption that the pits have a constant diameter to depth ratio probably is conservative. It was shown by Stinebring [4] for a cavitation damage study in the incubation zone that generally, the depth/diameter ratio increases with increasing diameter.

Another study of surface ship propellers by Wilson et.al. [16] for Naval Auxiliary Oilers (AO-177 class) studied the vibration and damage problem due to wakes. The ships had severe vibration transmited through the hull and

damage on the propeller blade trailing edges near the tip. They attributed the cause of the problem to the unsteady cavitation on the blades as they passed through the hull wake. The cavity would grow while in the wake, then break off and collapse against the trailing edge when leaving the wake. Adding a special fin upstream of the propeller reduced the wake deficit which reduced vibration and damage. Observations also showed that in addition to reducing the volume of cavitation, the cavity also collapsed in the free stream away from the blade.

These are just two examples of the increased damage due to the unsteady cavitation produced on blades passing through wakes.

Table B1

Run U5 $\sigma = 3.44$ Pitting Rate = 540 pits/cm^2/hr

Run W1 $\sigma = 3.51$ Pitting Rate = 1340 pits/cm^2/hr

Size Distribution of Pits
(% of Pits Within Size Range)

Diameter (mm)	Run U5	Run W1
< 3.0	36	9
3.0-4.1	47	19
4.2-5.3	11	12
5.4-6.4	3	13
6.5-7.4	3	12
7.5-8.4		12
8.5-9.5		10
9.6-10.6		3
10.7-11.7		3
11.8-12.9		2
13.0-14.0		1
14.1-15.0		1
15.1-16.1		2
16.2-17.3		1

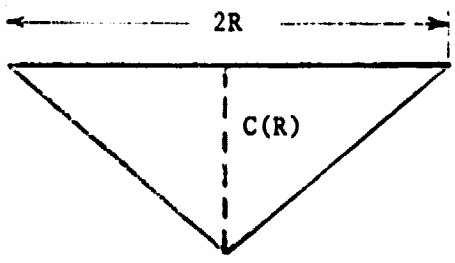

$V = 1/3\ \pi R^2(C(R))$

$= (C/3)\ \pi R^3$

Average Over One Revolution	Volume Loss Rate	$\frac{(W1)}{(U5)} = \frac{89.2c}{3.7c} = 24.3$
Average Over Wake	Volume Loss Rate	$\frac{W1 - U5}{U5}\left(\frac{360°}{60°}\right) = 140$
Average Over Wake	Pitting Rate	$\frac{W1 - U5}{U5}\left(\frac{360°}{60°}\right) = 8.9$

APPENDIX C

Coordinate Data for the Redesigned Inlet Casing Vanes

The following sets of coordinates can be used to construct the newly designed vanes. All dimensions are in inches and the vane shapes are numbered as in Figure 48. The x-axis is positive to the right of the page and the y-axis is positive to the top of the page.

VALVE # 2

X	Y
-0.00011	4.00000
0.00116	4.01550
0.00372	4.03774
0.00856	4.06940
0.02320	4.15125
0.04120	4.29115
0.06427	4.45835
0.09074	4.66087
0.11929	4.89638
0.14981	5.16200
0.18018	5.45149
0.20762	5.75869
0.22906	6.07387
0.24037	6.38703
0.23840	6.68559
0.22059	6.95669
0.18700	7.18663
0.13911	7.36291
0.10864	7.42820
0.07651	7.47683
0.04894	7.50248
0.02175	7.51742
-0.00020	7.52042
-0.02225	7.51742
-0.04934	7.50248
-0.07691	7.47683
-0.10924	7.42819
-0.13850	7.36290
-0.18739	7.18662
-0.22096	6.95667
-0.23875	6.68558
-0.24071	6.38701
-0.22939	6.07366
-0.20793	5.75868
-0.18047	5.45148
-0.15009	5.16199
-0.11956	4.89676
-0.09099	4.66066
-0.06451	4.45835
-0.04143	4.29118
-0.02343	4.15156
-0.00876	4.06940
-0.00393	4.03774
-0.00137	4.01550
-0.00011	4.00000

X	Y
-1.47814	3.71587
-1.48692	3.73039
-1.49913	3.74962
-1.51607	3.77749
-1.56135	3.85942
-1.61498	3.97663
-1.67262	4.12979
-1.72583	4.31589
-1.76753	4.53183
-1.79210	4.77195
-1.79865	5.02857
-1.78159	5.29429
-1.75107	5.56288
-1.70878	5.82755
-1.65802	6.08039
-1.60526	6.31285
-1.56142	6.51594
-1.53635	6.68059
-1.53197	6.74682
-1.55708	6.80412
-1.55056	6.83615
-1.56786	6.85722
-1.58438	6.86711
-1.60307	6.87134
-1.63014	6.86726
-1.66146	6.85459
-1.70390	6.82927
-1.75468	6.78377
-1.86465	6.64160
-1.97461	6.43945
-2.06823	6.18808
-2.13415	5.90104
-2.16415	5.59504
-2.16001	5.28755
-2.12451	4.99014
-2.06217	4.71415
-1.97876	4.46766
-1.88293	4.25492
-1.78113	4.07956
-1.68325	3.94160
-1.59932	3.83760
-1.52958	3.76893
-1.50504	3.74573
-1.48905	3.72886
-1.47814	3.71687

VANE # 4

X	Y
-2.74717	2.90741
-2.76460	2.91662
-2.78948	2.92941
-2.82421	2.94813
-2.91732	3.00614
-3.03103	3.09367
-3.16137	3.21318
-3.29259	3.36456
-3.40851	3.54628
-3.49591	3.75226
-3.54580	3.97412
-3.55748	4.20460
-3.53430	4.43994
-3.46014	4.67693
-3.39648	4.90804
-3.30113	5.12306
-3.20449	5.31198
-3.12701	5.46643
-3.09834	5.53113
-3.08398	5.56794
-3.08729	5.62012
-3.09743	5.64174
-3.10923	5.65266
-3.12475	5.65865
-3.14831	5.65902
-3.17755	5.65263
-3.21964	5.63761
-3.28115	5.60379
-3.42912	5.48377
-3.58973	5.30229
-3.73853	5.06578
-3.85032	4.78635
-3.90728	4.48361
-3.90374	4.17875
-3.84063	3.89127
-3.72561	3.63671
-3.57498	3.42416
-3.40573	3.25484
-3.23262	3.12720
-3.07291	3.03527
-2.93692	2.97204
-2.83107	2.93528
-2.79256	2.92339
-2.76556	2.91440
-2.74717	2.90741

VANE # 5

X	Y
-3.62706	1.68654
-3.64542	1.68963
-3.67118	1.69478
-3.70770	1.70202
-3.80854	1.72761
-3.93672	1.77378
-4.08701	1.84344
-4.24547	1.94159
-4.39595	2.07023
-4.52380	2.22769
-4.61924	2.40710
-4.68026	2.60233
-4.70975	2.80984
-4.71056	3.02593
-4.68491	3.24287
-4.64135	3.44967
-4.59260	3.63396
-4.55336	3.78341
-4.54004	3.84374
-4.53675	3.89475
-4.54352	3.92241
-4.55487	3.93974
-4.56691	3.94764
-4.58066	3.95069
-4.60104	3.94679
-4.62496	3.93574
-4.66050	3.91301
-4.70807	3.87005
-4.81374	3.73779
-4.91961	3.54913
-5.00483	3.31454
-5.04956	3.04889
-5.04050	2.77199
-4.97479	2.50564
-4.85628	2.26790
-4.69591	2.07143
-4.50973	1.92165
-4.31502	1.81619
-4.12589	1.74925
-3.95707	1.71168
-3.81796	1.69208
-3.71026	1.68868
-3.67227	1.68856
-3.64564	1.68783
-3.62706	1.68654

VARS 4 5

X	Y
-3.99357	0.22663
-4.01090	0.22285
-4.03571	0.21752
-4.07105	0.21040
-4.16919	0.19634
-4.29707	0.19050
-4.45270	0.19702
-4.62290	0.22539
-4.79418	0.28307
-4.95271	0.37292
-5.08734	0.49185
-5.19515	0.63588
-5.27814	0.80136
-5.33914	0.98437
-5.37706	1.17818
-5.39604	1.36940
-5.40379	1.54246
-5.40969	1.68315
-5.41396	1.73947
-5.42482	1.76461
-5.43829	1.80571
-5.45262	1.81716
-5.46411	1.82003
-5.47648	1.81887
-5.49203	1.80961
-5.50864	1.79348
-5.53215	1.76445
-5.56041	1.71416
-5.61415	1.57045
-5.65350	1.37836
-5.66264	1.15298
-5.62924	0.91246
-5.54552	0.67876
-5.41430	0.47046
-5.24334	0.30378
-5.04663	0.18780
-4.84020	0.12162
-4.63871	0.09714
-4.45300	0.10521
-4.29343	0.13161
-4.16502	0.16322
-4.06875	0.19637
-4.03472	0.21204
-4.01068	0.22093
-3.99357	0.22663

VANE # 7

X	Y
-3.79469	-1.26508
-3.80898	-1.27519
-3.82925	-1.28971
-3.85802	-1.30956
-3.93979	-1.35991
-4.05036	-1.41384
-4.18755	-1.46692
-4.34383	-1.50540
-4.50913	-1.51870
-4.67048	-1.49769
-4.81819	-1.44232
-4.94821	-1.35531
-5.06365	-1.24020
-5.16500	-1.09987
-5.24940	-0.94144
-5.31712	-0.77754
-5.36925	-0.62597
-5.41140	-0.50265
-5.42956	-0.45296
-5.45020	-0.41556
-5.46667	-0.40224
-5.48166	-0.39594
-5.49209	-0.39625
-5.50178	-0.40086
-5.51224	-0.41301
-5.52140	-0.43126
-5.53289	-0.46245
-5.54371	-0.51450
-5.55048	-0.65598
-5.53309	-0.83467
-5.48133	-1.03447
-5.38897	-1.23454
-5.25426	-1.41376
-5.06462	-1.55536
-4.89096	-1.64601
-4.68806	-1.66139
-4.49174	-1.66722
-4.31228	-1.61669
-4.15536	-1.54274
-4.02608	-1.46085
-3.92445	-1.38589
-3.85136	-1.31869
-3.82621	-1.29373
-3.80777	-1.27679
-3.79469	-1.26508

VARIABLE # 8

X	Y
-3.05866	-2.57771
-3.06631	-2.59120
-3.07735	-2.61012
-3.09312	-2.63696
-3.14055	-2.70706
-3.20945	-2.76949
-3.29930	-2.88132
-3.40956	-2.96862
-3.53531	-3.03810
-3.67031	-3.08082
-3.80692	-3.09141
-3.94152	-3.07219
-4.07483	-3.02629
-4.20704	-2.95619
-4.33332	-2.86655
-4.44841	-2.76723
-4.54840	-2.67159
-4.62937	-2.59337
-4.68280	-2.55252
-4.69378	-2.54350
-4.71222	-2.53955
-4.72579	-2.54110
-4.73381	-2.54589
-4.73910	-2.55308
-4.74211	-2.56630
-4.74227	-2.58383
-4.73875	-2.61157
-4.72631	-2.65503
-4.67616	-2.76502
-4.59280	-2.89590
-4.47607	-3.02847
-4.32824	-3.14612
-4.15688	-3.23320
-3.97275	-3.27896
-3.78863	-3.27821
-3.61721	-3.23162
-3.46775	-3.14966
-3.34424	-3.04519
-3.24618	-2.93023
-3.17262	-2.81871
-3.11669	-2.72729
-3.08485	-2.64170
-3.07370	-2.61245
-3.06501	-2.59176
-3.05866	-2.57771

VALUE # 9

X	Y
-1.88942	-3.52563
-1.89156	-3.53703
-1.89442	-3.55313
-1.89927	-3.57581
-1.91525	-3.63839
-1.94361	-3.71715
-1.98612	-3.80870
-2.04481	-3.90394
-2.12020	-3.99403
-2.21116	-4.07104
-2.31380	-4.13006
-2.42464	-4.17059
-2.54171	-4.19484
-2.66364	-4.20507
-2.78628	-4.20238
-2.90316	-4.19083
-3.00774	-4.17634
-3.09220	-4.16611
-3.12601	-4.16340
-3.15417	-4.16568
-3.16873	-4.17142
-3.17772	-4.17914
-3.18041	-4.18608
-3.18162	-4.19389
-3.17802	-4.20496
-3.17006	-4.21721
-3.15496	-4.23526
-3.12838	-4.25753
-3.09432	-4.30532
-2.94019	-4.35053
-2.80828	-4.38350
-2.66070	-4.39513
-2.50831	-4.37949
-2.36157	-4.33508
-2.22957	-4.26342
-2.11851	-4.16953
-2.03210	-4.06037
-1.96957	-3.94554
-1.92803	-3.83244
-1.90546	-3.72979
-1.89301	-3.64416
-1.89074	-3.57744
-1.89074	-3.55365
-1.89031	-3.53735
-1.88942	-3.52563

Value = 17

X	Y
-1.45153	2.27532
-1.45330	2.27943
-1.45511	2.28385
-1.45711	2.29025
-1.46347	2.30900
-1.47395	2.33450
-1.48656	2.36645
-1.50195	2.40399
-1.52013	2.44553
-1.54040	2.49039
-1.56237	2.53709
-1.58619	2.58399
-1.61126	2.62947
-1.63749	2.67161
-1.66401	2.70931
-1.69000	2.74046
-1.71506	2.76399
-1.73804	2.77943
-1.74812	2.78381
-1.75765	2.78579
-1.76444	2.78581
-1.77091	2.78386
-1.77448	2.78221
-1.77749	2.77966
-1.78199	2.77462
-1.78483	2.76846
-1.78705	2.75898
-1.78733	2.74799
-1.78302	2.72065
-1.77225	2.68799
-1.75497	2.65130
-1.73214	2.61144
-1.70482	2.56980
-1.67414	2.52769
-1.64167	2.48652
-1.60859	2.44690
-1.57645	2.40960
-1.54646	2.37560
-1.51891	2.34582
-1.49526	2.32091
-1.47634	2.30111
-1.46210	2.28725
-1.45727	2.28247
-1.45402	2.27897
-1.45163	2.27632

VALE = 18

X	Y
-2.61861	0.65751
-2.62182	0.65876
-2.62616	0.66073
-2.63223	0.66380
-2.64948	0.67293
-2.67464	0.68461
-2.70576	0.69918
-2.74272	0.71589
-2.78446	0.73360
-2.83001	0.75229
-2.87805	0.77114
-2.92757	0.78887
-2.97703	0.80472
-3.02517	0.81747
-3.07020	0.82652
-3.11048	0.83132
-3.14487	0.83121
-3.17217	0.82565
-3.19251	0.82291
-3.19080	0.81760
-3.19574	0.81316
-3.19911	0.80730
-3.20056	0.80364
-3.20101	0.79972
-3.20081	0.79297
-3.19805	0.78554
-3.19376	0.77812
-3.18641	0.76994
-3.16450	0.75303
-3.13424	0.73669
-3.09648	0.72188
-3.05251	0.70359
-3.00406	0.69709
-2.95298	0.68769
-2.90096	0.67992
-2.84970	0.67384
-2.80073	0.66880
-2.75558	0.66469
-2.71510	0.66196
-2.68080	0.66010
-2.65345	0.65870
-2.63359	0.65840
-2.62679	0.65824
-2.62202	0.65793
-2.61861	0.65751

VALUE # 19

X	Y
-2.35496	-1.32047
-2.35814	-1.32176
-2.36256	-1.32331
-2.36917	-1.32525
-2.38627	-1.33074
-2.41430	-1.33925
-2.44691	-1.35003
-2.48526	-1.36327
-2.52776	-1.37906
-2.57370	-1.39576
-2.62157	-1.41505
-2.66974	-1.43717
-2.71658	-1.45962
-2.76033	-1.48341
-2.79928	-1.50776
-2.83185	-1.53194
-2.85676	-1.55563
-2.87348	-1.57770
-2.87843	-1.58752
-2.88094	-1.59392
-2.88135	-1.60369
-2.87977	-1.61026
-2.87832	-1.61392
-2.87595	-1.61707
-2.87117	-1.62185
-2.86518	-1.62503
-2.85544	-1.62779
-2.84439	-1.62869
-2.81734	-1.62594
-2.78413	-1.61704
-2.74651	-1.60186
-2.70542	-1.58133
-2.66230	-1.55541
-2.61872	-1.52316
-2.57558	-1.49306
-2.53415	-1.46730
-2.49509	-1.43734
-2.45914	-1.40331
-2.42814	-1.38350
-2.40194	-1.36130
-2.38109	-1.34353
-2.36645	-1.33010
-2.35740	-1.32555
-2.35772	-1.32251
-2.35496	-1.32047